UNIVERSITAT POLITÈCNICA DE VALÈNCIA

DEPARTAMENT DE COMUNICACIONS

Reconfigurable Reflective Arrayed Waveguide Grating on Silicon Nitride

Industrial Ph.D. THESIS

by
Juan Fernández Vicente

Ph.D. Supervisors:
Dr. Pascual Muñoz Muñoz
Dr. Jose David Doménech Gómez

Valencia, March 2021

UNIVERSITAT POLITÈCNICA DE VALÈNCIA

DEPARTAMENT DE COMUNICACIONS

Reconfigurable Reflective Arrayed Waveguide Grating on Silicon Nitride

Juan Fernández Vicente
Photonics Research Labs (PRL)
Instituto de Telecomunicaciones y Aplicaciones Multimedia (iTEAM) Research Institute
Universitat Politècnica de València
Camí de Vera s/n, 46022 Valencia, SPAIN
VLC Photonics S.L.
juaferv3@doctor.upv.es, juan.fernandez@vlcphotonics.com

Ph.D. Supervisors:
Dr. Pascual Muñoz Muñoz
Dr. Jose David Doménech Gómez

Valencia, March 2021

A Ester, mis amigos y familia...

Hay gente que hace la caja.
Y otros que nos dedicamos a mover la caja.
Juan Fernandez
There is people making the box.
And others that we are working moving the box.
Juan Fernandez

Agradecimientos

Han sido unos años difíciles, con una lucha muy grande por mantener el equilibrio entre desarrollar un trabajo, un doctorado y una relación con las personas que me importan. Y este equilibrio es gracias a personas concretas que han conseguido que culmine este largo viaje.

Primero agradecer a mi profesor de Tesis, el catedrático Pascual Muñoz, por la primera vez que mencionó la óptica integrada en una clase de tercero mientras yo pensaba en mi futuro. Gracias a esto desarrollé un trabajo final de grado al respecto, unas prácticas de empresa en VLC Photonics, un trabajo final de máster y esta tesis. Aunque siempre está muy ocupado, cuando toca arremangarse y hacer trabajo duro ha estado ahí, y, gracias a su manera de trabajar, me ha empujado a ser autosuficiente, no dar nada por sabido, ser muy exhaustivo con la literatura y no rendirme por lo que como soy ahora es en gran parte gracias a él.

También quería agradecer al grupo de investigación, Photonics Research Lab (PRL), que durante años hemos discutido aspectos técnicos que me han ayudado a progresar y entender mejor todo, en especial a Gloria Micó, Daniel Pastor, Daniel Pérez, Luis Bru, Rubén Alemany y Jesús Benítez. Agradecer en especial a Daniel Pastor, tanto por las discusiones teóricas del dispositivo como por las enriquecedoras discusiones de muchos aspectos como en el algortimo de esta tesis que lleva sus siglas, y a Luis Bru por echarme una mano con las medidas de OFDR que corroboraban mis resultados. En cuanto a lo académico, quería también agradecer a todo el equipo del Centro Nacional de Microélectronica (CNM), donde se han fabricado todos los elementos de esta tesis. Gracias a su tecnología de nitruro de silicio, tenemos un centro de fabricación español que permite la fabricación de elementos para la fotónica integrada. En especial mencionar a Carlos Domínguez, que aunque le pedimos lo imposible, siempre está arrimando el hombro y haciendo todo lo que está en su mano para ayudarnos.

Toda esta tesis se ha desarrollado en la empresa VLC Photonics a la que estoy eternamente agradecido. Gracias a empezar primero como becario y luego como doctorando industrial, me ha permitido ver y aprender bastantes cosas muy diversas dentro de la óptica integrada y del funcionamiento de una empresa. Cuando empecé éramos tan sólo David Doménech, Iñigo Artundo y yo, y ahora somos 17 personas, con lo que ver en primera persona el progreso de esta empresa ha sido un

orgullo. Aunque en parte ha sido un sacrificio tener que trabajar en una pequeña empresa, con lo que supone eso en cuanto a bajo salario, cantidad de trabajo, roles y forma de ser de cada uno, ha sido toda una experiencia vital muy enriquecedor. Sobre todo, gracias a personas concretas como David Doménech, cotutor de esta tesis y CTO de la empresa que, con sus manías, detecta los errores tan sólo con una mirada, pero también con su trabajo duro y dedicación a la familia, es un ejemplo a seguir. A Iñigo Artundo, CEO de la empresa que, con su entusiasmo y positivismo, da la vuelta a situaciones en las que parece que todo está perdido. A Bernardo Gargallo, mánager del equipo de diseño o mi jefe directo, aunque cariñosamente le he llamado a veces el Grinch mientras trabajamos, gracias a él no podría entender dónde estoy ahora, porque a pesar de todo y de todo lo que le ha pasado, es un trabajador incansable, muy metódico, organizado, una gran persona y con una visión de la vida de disfrute y alegría. Realmente he aprendido mucho de él y es un gran ejemplo como persona. Y también agradecer al resto del equipo tanto antiguo como nuevo como Rocío, Joan, Alberto, Pepa, Raffaele, Jose, Edu, Marco, Alba, Luis-Olivier, Giovanni, Jordi y en especial, a Álvaro, compañero del equipo de diseño. Álvaro, aunque vino hace poco relativamente, parece que lleva toda la vida y su manera de actuar y ser en el trabajo y con los compañeros, ha sido una gran ayuda para todos demostrando que el buen hacer es un valor seguro para cualquier trabajo. Quería agradecer también a todos esos becarios que han pasado por la empresa y que sin ellos mucho trabajo no hubiera podido llevarse a cabo.

Agradecer también a todos mis amigos en especial a Javi, Dani, Juan, Anatol, y a toda mi familia por haber estado ahí, no sólo durante estos 4 años de tesis, sino durante toda la vida en lo bueno y en lo malo. También a mis compañeros de la universidad, con los que compartí la carrera, máster y salidas memorables, pero que también se han convertido en amigos, en especial a Jose, Carlos y Guille.

Y finalmente, agradecer a mi compañera de vida desde los 17 años, Ester. Aunque hemos tenido momentos muy difíciles en los que el mundo se acabó, has sido mi apoyo y mi motivación durante años para mejorar en lo personal y en lo profesional, no podría entender como soy sin ti. Casarnos en pleno doctorado ha sido nuestra mayor locura, pero espero que no la última, del resto de nuestra vida.

A todos vosotros, ¡gracias!

Abstract

This thesis is focused on the modelling, design and experimental demonstration for the first time of Reconfigurable Reflective Arrayed Waveguide Grating (R-RAWG) device. In order to build this device, that can be employed in spectrometry, a silicon nitride platform termed CNM-VLC has been chosen since this material allows to operate in broad range of wavelengths. This platform has the necessary elements, but some limitations because the operation of this device had a low performance. Therefore, a methodology has been developed and validated, which has allowed to obtain better splitters. Also an inverted taper has been designed, which has considerably improved the coupling of light to the chip. This has been possible thanks to an exhaustive analysis of existing options in the literature, that has allowed choosing the best option to make a reconfigurable mirror on the platform without changing or adding new manufacturing steps. Reconfigurable mirrors have been demonstrated by using feedback splitters. Furthermore, codes have been developed to predict the behaviour of the actual device. With all the work done, a R-RAWG has been designed by using certain considerations so that it can operate over a broad wavelength range and the phase actuators are not in danger of being damaged. A code has also been developed for the modelling of the R-RAWG, which allows manufacturing imperfections to be considered, thanks to this, a method or algorithm called DPASTOR has been developed. DPASTOR resembles machine learning to optimise the response by just using the optical output power. Finally, a PCB and an assembly with the chip interconnected to it have been made and designed. Moreover, a measurement method has been developed, which has made it possible to have a stable response and to demonstrate a multitude of optical filter responses with the same device.

Resumen

La presente tesis se ha centrado en el modelado, diseño y demonstración experimental por primera vez del dispositivo Reconfigurable Reflective Arrayed Waveguide Grating (R-RAWG). Para la consecución de este dispositivo que tiene posibilidades de uso en la espectrometría, una plataforma de nitruro de silicio llamada CNM-VLC se ha usado, ya que este material permite operar en un gran ancho de banda. Esta plataforma posee ciertas limitaciones y los elementos necesarios para el funcionamiento de este dispositivo tenían un performance bajo. Por ello, se ha desarrollado y validado una metodología que ha permitido obtener mejores divisores. Además, se ha diseñado un inverted taper que ha mejorado considerablemente el acoplo de luz al chip. Esto ha sido gracias a un exhaustivo análisis de opciones existentes en la literatura que también ha permitido escoger la mejor opción para realizar un espejo reconfigurable en la plataforma sin cambiar ni añadir ningún proceso de fabricación. Se han demostrado espejos reconfigurables gracias a utilizar divisores ópticos realimentados y también se ha desarrollado códigos que predicen el comportamiento del dispositivo experimentalmente. Con todo el trabajo realizado, se ha diseñado un R-RAWG para que pudiera operar en un gran ancho de banda y que los actuadores de fase no tuvieran peligro de estropearse. También se ha desarrollado un código para el modelado del R-RAWG que permite imitar la fabricación de estos dispositivos y que, gracias a esto, se ha desarrollado un método o algoritmo llamado DPASTOR, que usa algoritmos usados en machine learning, para optimizar la respuesta con tan sólo la potencia óptica de salida. Finalmente, se ha diseñado una PCB para poder conectar eléctricamente el chip fotónico y se ha desarrollado un método de medida que ha permitido tener una respuesta estable consiguiendo demostrar multitud de respuestas de filtros ópticos con el mismo dispositivo.

Resum

La present tesi s'ha centrat en el modelatge, disseny i demonstració experimental per primera vegada del dispositiu Reconfigurable Reflective Arrayed Waveguide Grating (R-RAWG). Per a la consecució d'aquest dispositiu que té possibilitats d'ús en l'espectrometria, una plataforma de nitrur de silici anomenada CNM-VLC s'ha usat ja que aquest material permet operar en una gran amplada de banda. Aquesta plataforma posseeix certes limitacions i els elements necessaris per al funcionament d'aquest dispositiu tenien un performance baix. Per això, s'ha desenvolupat i validat una metodologia que ha permés obtindre millors divisors i també, gràcies als processos de fabricació, s'ha dissenyat un acoplador que ha millorat considerablement l'acoble de llum al xip. Això ha sigut gràcies a un exhaustiu analisis d'opcions existents en la literatura que també ha permés triar la millor opció per a realitzar un espill reconfigurable en la plataforma sense canviar ni afegir cap procés de fabricació. S'han demonstrat espills reconfigurables gràcies a utilitzar divisors realimentats i també s'ha desenvolupat codis que prediuen el comportament del dispostiu experimentalment. Amb tot el treball realitzat, s'ha dissenyat un R-RAWG fent ús de determinades consideracions perquè poguera operar en una gran amplada de banda i que els actuadors de fase no tingueren perill de desbaratar-se. També s'ha desenvolupat un codi per al modelatge del R-RAWG que permet imitar la fabricació d'aquests dispositius i que, gràcies a això, s'ha desenvolupat un mètode o algorisme anomenat DPASTOR, que usa algorismes usats en machine learning, per a optimitzar la resposta amb tan sols la potència òptica d'eixida. Finalment, s'ha dissenyat una PCB per a poder connectar elèctricament el xip fotònic i s'ha desenvolupat un mètode de mesura que ha permés tindre una resposta estable aconseguint demostrar multitud de respostes de filtres òptics amb el mateix dispositiu.

Contents

List of Figures

List of Tables

List of abbreviations

AOWG Arbitrary Optical Waveform Generator.

ASE Amplified Spontaneous Emission.

AWG Arrayed Waveguide Grating.

BB Building Blocks.

CMOS Complementary Metal-Oxide-Semiconductor.

DBR Distrubuted Bragg Reflector.

DC Directional couplers.

DPASTOR Descend the hill and Progressively AScend TOwards Reconfiguration.

EG Echelle Grating.

EME Eigenmode Expansion Method.

FIR Finite Impulse Response.

FPPGA Field Programmable Photonics Gate array.

FPR Free Propagation Region.

FSR Free Spectral Range.

GMO Global Multivariable Optimization.

InP Indium Phosphide.

LIDAR Laser Imaging Detection and Ranging.

LPCVD Low pressure chemical vapor deposition.

MEM Micro-Electro-Mechanics.

MFD Mode Field Diameter.

MMI Multimode Interferometer.

MMIR MMI reflector.

MPW Multi-Project Wafer.

MZI Mach-Zehnder Interferometer.

OFDR Optical Frequency Domain Reflectometry.

OSA Optical Spectrum Analyzer.

PCB Printed Circuit Board.

PCG Planar Concave Grating.

PDK Process Design Kit.

PDL Polarization Dependent Loss.

PIC Photonic Integrated Circuit.

PLC Planar Lightwave Circuit.

PS Phase Shifter.

R-RAWG Reconfigurable Reflective Arrayed Waveguide Grating.

RAWG Reflective Arrayed Waveguide Grating.

RR Ring Resonator.

SiNx Silicon Nitride.

SLR Sagnac Loop Reflector.

SOA Semiconductor Optical Amplifier.

SOI Silicon-On-Insulator.

SSC Spot Size Converter.

TEC ThermoElectric Cooler.

TOP thermo-optic phase shifter.

TRML Tunable Reflective Michelson Loop.

Chapter 1
Introduction

From the dawn of time, light has been man's constant companion. Our ancestors, the Homo sapiens, were enlightened and fascinated by the same sunlight that illuminates us today. Then, the humans wanted to dominate the light because it allowed them to see in the dark, which became a symbol of intelligence, purity and progress. The appearance of J.C. Maxwell's equations in 1873 [1] allowed to start light's nature searching. The light was understood as an electromagnetic wave at a very high frequency and this interpretation of Maxwell's formulas explained many physical effects satisfactorily. However, with the discovery of the photoelectric effect in 1887 [2], this theory of light was questioned by Einstein, who was able to demonstrate this effect by taking light as a small quantum of energy in 1905 [3]. This double behaviour of light as a wave or as a particle was classically referred to as the wave-particle duality. However, it was not until Schrödinger equation in 1925 [4], which was the concept of the wave function, that the two concepts were fully connected for the theoretical development of photonics as we know it today [5].

Throughout history, the generation of light and its use has been based mainly on emulation of the sun, for illuminating. In the world of electricity, communications emerged with the electrical wire telegraph in the early twentieth century and, since the Maxwell's equations came along, the use of electromagnetic waves for wireless communication for short distances began. Then Einstein suggested that light could be generated coherently [6] by promoting the laser invention in 1960 [7], which revolutionized optical communications. Also, in those years, the term photonics was coined as a science and then fiber optics was invented, which gradually took over all communications by replacing communications with electrical cables, which were much more inefficient in terms of consumption and bandwidth [8].

On the other hand, in the years in which photonics came along, electronics or the use of electrons became so specialized that it illuminated diverse components for the processing, miniaturizing them at microscopic levels and thus microelec-

tronics was born. Microelectronics improved in many aspects such as consumption, robustness and size compared to the classic electronics, as well as its ease of mass production. Thus, it was possible to have the consumer electronics of the common user opening an immense market like the computers or the mobiles phones [9]. In the photonics, it happened the same as from the electronics to the microelectronics, lighting the so called integrated photonics. Integrated photonic solves problems and applications of the common optics since it allows to integrate monolithically a very complex system in the same miniaturized substrate [10]. In the beginnings of the integrated optics, the existing technologies were not sufficiently mature and precise for the operation of the suitable circuits, especially for high contrast platforms like the silicon photonics and the indium phosphide, in which the low precision in manufacturing involved high propagation losses and variability. Therefore, the platforms that became commercial products were those of very low contrast, such as PLC [11]. After those years, initiatives emerged to promote the research and commercialization of other material platforms [12]. Thus, in integrated photonics, as in the microelectronics industry, the development of generic processes was promoted, which allowed the creation of a consortium where ideas and products were developed [13]. Thanks to these initiatives and the commercialization of the Photonic Integrated Circuit (PIC), such as transceivers [14], the manufacturing processes of the different foundries have improved enormously, opening the possibility of other products and implementations.

Throughout the years, within the integrated photonics, different devices with specific functionalities have been developed. These devices, depending on their functionality, can be divided into categories. These categories are:

- Light-guiding structures, both waveguides of all types and special crossings, bends, spirals, etc.
- Power splitters, which divide the full spectrum of the light, whether passively or actively, statically.
- Light couplers to the PICs, which are responsible for coupling light to the chip, reducing losses with respect to the optical field input.
- Active and passive optical filters, which create a wavelength pattern according to which some frequencies have higher losses.
- Light modulators, which seek to modify the amplitude and phase of the light that passes through them with an external source.
- Light detectors, which are devices that can transform the optical power to electrical signal.
- Amplifiers or light emitters, which are devices with a structure that allows them to generate light or increase the optical signal.

With these basic functionalities, any system can be divided in small devices and thus be able to develop the device that best fits the needs of that functionality

in the system. Optical filters are one of them and these elements can be implemented in different ways, such as Mach-Zehnder Interferometers (MZIs) [15], Ring Resonators (RRs) [16], Distrubuted Bragg Reflectors (DBRs) [17], Planar Concave Gratings (PCGs) or Echelle Gratings (EGs) [18], [19] or Arrayed Waveguide Gratings (AWGs) [20]. Within these last type filters, there is a subcategory of reconfigurable filters, whose response can be reconfigured with active tuning to achieve the desired response. Thus, it would allow, once manufactured, to adapt to the requirements by modifying the optical system without the need for a new product. In the world of photonic integrated reconfiguration, there are systems and devices that are attracting a lot of attention, such as Field Programmable Photonics Gate array (FPPGA) [21], nano-photonic artificial intelligence [22], linear optical quantum computing [23] and Arbitrary Optical Waveform Generator (AOWG) [24]. So the reconfigurable filters are a basic part of many of them as well as for other applications in fields such as LIDAR, biosensing, microwave processing, telecommunications, etc [25]–[29]. This thesis is focused on the development and the first time experimental demonstration of a reconfigurable filter called R-RAWG [30], which is included in AWG filters group but has a particular configuration that will be explained in the following sections in depth.

1.1 Generic integration Technologies

To fabricate PICs, multiple material technologies are available, although, due to its fabrication properties and its characteristics, there are mainly four that are the most-demanded nowadays: Silica [31], Indium Phosphide (InP) [32], Silicon-On-Insulator (SOI) [33] and Silicon Nitride (SiNx) [34]. Each technology has its advantages and disadvantages, but depending on the characteristics that are needed in the integrated system, one of them will stand out from the rest. First of all, it should be noted that the Silica is not a platform that offers Multi-Project Wafer (MPW) runs. The MPWs are periodic productions with several clients that share the manufacturing costs of a whole wafer and thus reduce the prototype price. The fabrication process does not change and this is the base of the development and research on the platforms with a Process Design Kit (PDK) with certain tested devices or building blocks. In the silica platforms, the manufacturing is very mature and with reduced costs so the dedicated runs are the only way to obtain systems in this type of substrate. In addition to this, the Silica is a low contrast platform that allows to operate in the communications band with a great bandwidth and very repetitive devices with great performance. The main disadvantages are that due to its low contrast, this platform only allows to make simple systems or elements, since a radius of curvature of a few millimetres and it does not allow for the monolithic integration of active components.

InP technology allows the use of light generation, amplification and detection elements in the telecommunications band. Due to the manufacturing process and the layers that are necessary, it is a platform that is considered medium index contrast this leads to waveguides with relatively large bending radius, so the in-

tegration is moderate. Thanks to this, it allows the monolithic integration of the whole system in the same substrate, having the source, the system and the detection in the same chip. However, it is a technology that requires a very precise manufacturing with multiple steps having easily failures in manufacturing. Furthermore, the PICs are very fragile, which makes the packaging very expensive.

Silicon Photonics' technology emerged mainly because microelectronics circuits are based on the processing of this type of wafers. Thanks to the already developed electronic CMOS processes, guiding, high frequency modulation and photodetection can be defined. There are two modalities within this type of material: the thin silicon version and the thick silicon version. The thick silicon version [35] has been the basis for the development of the first transceivers, since it allowed to make high speed modulators with low relative losses. The thin silicon version needed a lot of development to define low loss processes but have managed to demonstrate multiple devices at high modulation speeds in complex systems with low losses. In addition to this, due to its high contrast, its bending radius is the most compact, using the smallest area when compared to other technologies. Due to its easy scaling-up production, rapid improvement in manufacturing, repeatability, and the number of companies and research centers working on it, it is destined to be the technology for all products based on integrated optics. However, nowadays the main problem is that it requires external light sources and amplifiers.

Finally, the silicon nitride technology came along a few years ago, mainly represented by the TripleX platform [36]. But the portfolio of foundries offering open-access nitride platforms is extended to CNM-VLC, Ligentec and IMEC [37]. This material, which is also used in CMOS processes, allows operation in a wide range of wavelengths from visible to mid-infrared. It has a moderate contrast index and low losses have been demonstrated so there are certain systems based on high-Q resonators for which this platform is ideal. Moreover, because it allows operating in visible wavelength and also in mid-infrared, there is a boom of customers and institutions that want to integrate their bio-sensors or optical sensors in this type of platform. Thus, the silicon platforms are integrating this type of material together with the silicon guidance to combine in the same platform both technologies, which allows to define circuits in the silicon nitride and also in the silicon [38].

The main purpose of this thesis is to define a device that allows to make a wavelength filter for large wavelength range that can be used for mid-infrared and also for visible range where the highest number of applications for the filters is. These filters allow, among other things, spectrometry or wavelength spectrum analysis, which is used for substance and gas detection applications. Silicone Nitride technology is therefore ideal for this purpose.

Thanks to the collaboration between the company where this PhD was developed, VLC Photonics [39], and Centro Nacional de Microelectrónica (CNM) in Barcelona [40], a fabrication process of 300 nm LPCVD nitride on 2.5 micron oxide and 2 micron deposited oxide on top of the waveguides was defined. In addition, a step to define an etching of 150 nm to make shallow waveguides, a process to make

selective area trench in the oxide to do sensing and a process to deposit and define metals on top of the waveguides to make heaters were defined. This stable and standardized process has been reported previously [34] and thanks to the MPWs defined in this technology, the cost of manufacturing can be split between different users, having available chip sizes of 10x5 mm^2 and 5x5 mm^2. The final device and all the elements of this thesis have been fabricated in this platform. The different possible cross-sections can be shown in Fig. 1.1.

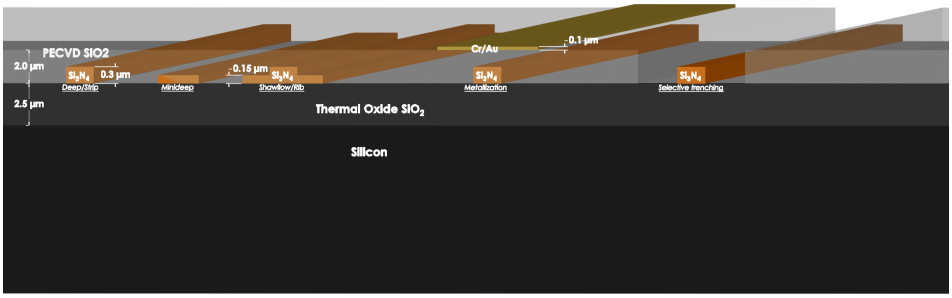

Figure 1.1: Different cross-section possible in CNM-VLC platform.

1.2 Reconfigurable Spectrometers: The Reconfigurable Reflective Arrayed Waveguide Grating (R-RAWG)

Reconfigurable filters, as explained in the introduction, are used for many applications, including spectrometry. Optical spectrometry is a technique that can be employed to characterize elements and substances, analyzing the optical spectrum of light transmitted or reflected through the element under analysis. There are several commercial products but integrating it in a miniaturized photonic chip would allow to make this device a low cost commercial element. There are several approaches in the literature to implement this in integrated optics. As a result of this interest, our research group developed a patent of a Reflective Arrayed Waveguide Grating (RAWG) to implement this functionality [30]. This device, apart from being used for spectrometry, can be reconfigured to obtain arbitrary filter responses. Due to the intrinsic phase and amplitude errors existing in any PIC manufacturing platform, the reconfigurability would help to recover a filter response despite these variations in all manufactured devices. The theoretical formalism of the device can be found detailed in [41].

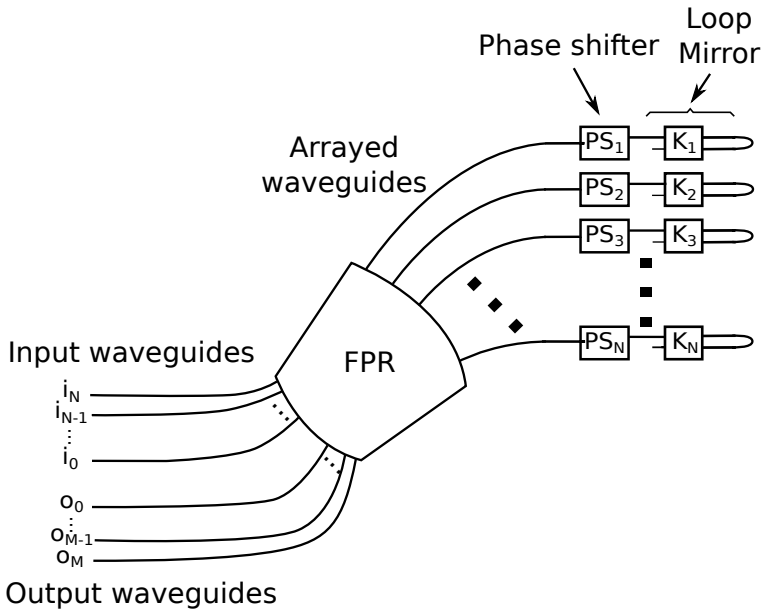

Figure 1.2: RAWG device schematic. FPR: free propagation region, PS: phase shifter, K coupling constant, xi are reference coordinates for arrayed waveguides and ij , oj are input and output waveguides.

As can be seen in Fig. 1.2, the device consists of a number of input and output waveguides connected to a star coupler and this divides the optical power with a Gaussian distribution in the waveguide array. The array has a fixed incremental length between waveguides that sets the Free Spectral Range (FSR) of the spectral response, and each waveguide of the array is connected to a reflective loop to control of the amplitude and phase. This configuration allows the device to reflect the signal and route the channels to the outputs.

Despite a detailed analysis and design of the device has been carried out, only a passive RAWG could be characterized in the our previous work. The main problem was that the reflectors were not well characterized and modelled. This thesis will show the development of the necessary blocks for the R-RAWG on the chosen silicon nitride platform as well as its characterization. Also, the analysis, simulation and characterization of loop reflectors and, finally, a design, characterization and demonstration of the reconfiguration of R-RAWG. In this last section, it will be shown the points taken into account to design this device, the algorithm developed to optimize the response and the problems and solutions developed to characterize this device.

1.3 Objectives

This thesis has three fundamental objectives:

1. To develop and optimize the necessary building blocks for the R-RAWG in the CNM-VLC platform:
   1.1. Couplers for PICs.
   1.2. Power splitters.
2. To develop for reconfigurable loop reflectors:
   2.1. Analytical model of this type of reflector.
   2.2. Develop a simulation tool to predict the spectral response of the reflectors.
   2.3. Characterization of the designed and fabricated devices.
3. Design, manufacture and demonstrate the R-RAWG as well as its reconfiguration:
   3.1. Detect the best design strategy of this device for its proper functioning.
   3.2. To develop a simulator including the response of the reflectors.
   3.3. To develop an automatic method for its optimization.
   3.4. To obtain equipment and create the necessary structures and methods to be able to characterize a complex device with many actuators.

1.4 Thesis outline

This thesis is structured in the following chapters:

- **Chapter 2** studies the basic building blocks required for the R-RAWG. The literature of different implementations and possibilities of chip coupling has been reviewed. An edge coupler has been designed using the existing manufacturing processes and testing their improvement. Also the literature of different implementations for a splitter has been reviewed. A new design flow for a splitter type has been proposed and tested for improvement.
- **Chapter 3** includes the study, modeling and characterization of a mirror reconfigurable in phase and amplitude. A literature study of integrated reconfigurable mirrors has been conducted. Mathematical modeling has been performed to predict the response of the characterization of these mirrors in amplitude and phase.

- **Chapter 4** shows the design, characterization and reconfiguration of the R-RAWG. An algorithm obtaining the desired reconfiguration only with the optical power has been developed and validated through multiple experimental realizations. Different strategies in the design were carried out to improve its performance. Also, a measurement method and the associated electronics were developed to ease the characterization of this circuit.
- Finally, in **Chapter 5** the conclusions and considerations for future work are presented.

Chapter 2
PIC basic building blocks: splitters and fiber couplers

The silicon nitride platform CNM-VLC [40] is a good candidate to develop the device proposed in this thesis, as explained in the introduction. Moreover, the standard PDK developed in the platform offered an edge coupler with 2.5x2.5 μm^2 MFD and different optical splitters. However, each edge coupler had 3 dB coupling loss, and the splitters were highly dependent on manufacturing.

In this chapter, an analysis of the splitters has been done. This has allowed to detect the weakness of previous designs and show a new design flow that improves performance. Furthermore, it has been carried out an analysis of PIC couplers showing the design and characterization of an edge coupler based on the standard fabrication steps.

Finally, the chapter conclusions are presented together with future developments to improve the standard platform. Some parts of the following chapter were previously published in a journal and at a conference and are reprinted here with permission [42], [43].

2.1 Background and motivation

The basic building blocks, which achieve certain specifications, are the basis of the standard platform PDKs. Thanks to these PDKs and their blocks, more complex structures can be implemented without risk that, due to the bad performance of a single block, the whole system response could be altered. Following the path of semiconductor microelectronics [44]–[46], the photonic integration foundries have designed and tested some basic blocks with which external customers can build complex systems [47].

According to the existing information in the different PDKs of the manufacturing processes of the companies or research centers around the world in all the

material platforms [34], [48]–[50], the basic blocks of a PDK can be divided into:

- Waveguides, which are usually strip/deep and rib/shallow. The information provided for those waveguides are: the recommended width or monomode width, group index and effective index.
- Optical splitters, which can be 50/50 or other type of splitting.
- Couplers to the PICs, which can be for horizontal (edge couplers) or vertical (grating couplers 1D, 2D) coupling.
- Optical filters, such as RR, MZI, DBR.
- Waveguide constructions such as crossings, transitions, bends, spirals.
- Thermal active structures such as thermo-optic phase shifters or thermo-optic switches.
- Electro-optical active structures such as electro-absorption modulators or plasma dispersion modulators.
- Optical amplification or emission active structures such as SOAs, lasers, etc.
- Optical detectors, such as photodetectors.
- Complex structures such as AWG, EG, etc.

The R-RAWG designed in this thesis was made on the CNM-VLC platform, which is a silicon nitride platform with metallization to make thermo-optic tuners. The implementation of the reconfigurable reflectors has been based on splitters and waveguides with thermo-optic phase shifters that will be seen in Chapter 3 of this thesis.

The optical couplers and splitters provided in the CNM-VLC PDK have been improved in order to improve as much as possible the overall response of the R-RAWG developed in this thesis.

2.2 Splitters and combiners

In photonic integrated circuits, the splitters/combiners are basic BBs to build more complex devices and systems [51]–[55]. The functionality of these elements is simple: splitting or combining the light at the output ports. [56].

There are four main structures to split and combine the light: Y-junctions, Directional couplers (DC), MMI and star couplers.

2.2.1 Implementations

Y-branch

This element is the most basic element to split and combine light. The main characteristics are that it can be lossless, fabrication tolerant, compact and broadband operating [57]–[62]. By dividing the input waveguide into two waveguides, the light is divided into two ports. The important design parameters are: the aperture angle between outputs ports, the width of the waveguides, the transition between the input and outputs and the splitting ratio desired. The main challenge of this element is the fabrication of the tip that in some higher index contrast technologies, the vertical position of the tip to the propagation of the light could introduce reflections.

In the literature, there are different implementations intended to optimize this element. The review of [63] shows the different approaches made in the past [64], [65]. Several computational methods have been employed to simulate this type of components like BPM or FDTD. Nowadays, inverse design techniques are being employed to optimize this element, thus obtaining high performance and different splitting ratios in broadband operation [66]–[68].

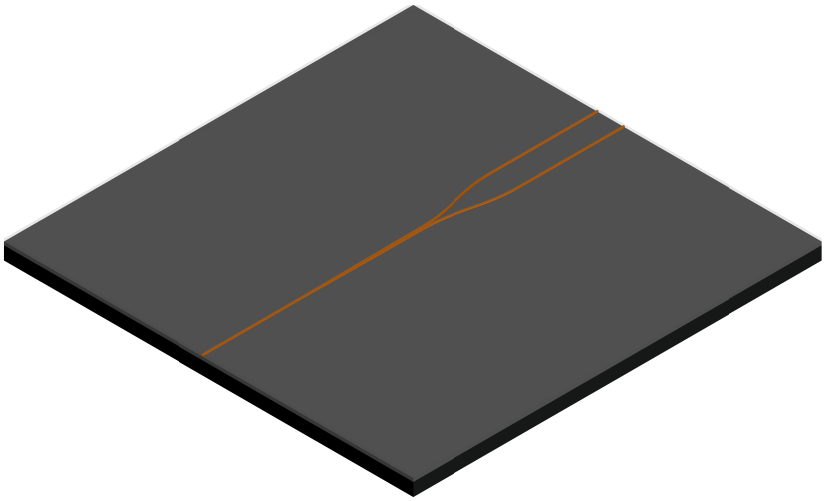

Figure 2.1: Example of Y-junction.

Directional couplers (DC)

If two optical waveguides are placed close together and the optical power is guided through one of them, a coupling effect between the waveguides occurs due to the propagation of the waves, thus splitting the light power in both waveguides. These elements are called Directional couplers (DC). On the one hand, by studying this

effect that is described by the coupled mode theory, any splitting ratio could be obtained by changing the length of the coupling section. On the other hand, traditional designs are sensitive to the input wavelength due to the coupling effect and to the fabrication tolerances such as the gap, width, thickness or refractive index of the parallel waveguides that could introduce big changes in the power response of this device. Among all, the important parameters to design these elements are: the width, gap and length of the waveguides, the gap and length of the fan-outs and cross-section. Recent developments in the design of this element have allowed the obtaining of devices which are less sensitive to fabrication tolerances in broadband operation. Among others, the most common approaches in the literature are bent couplers and adiabatic couplers [69]. First, bent couplers are based on the coupling study between bent waveguides which varies their width, gap, angle and length to obtain broadband operation and fabrication tolerance [70]. Second, adiabatic coupling studies the propagation of the modes in the devices to obtain the splitting desired for broadband operation and fabrication tolerance. The problem with this approach is that due to transitions, the total size of these devices is larger compared to other approaches [70]–[73].

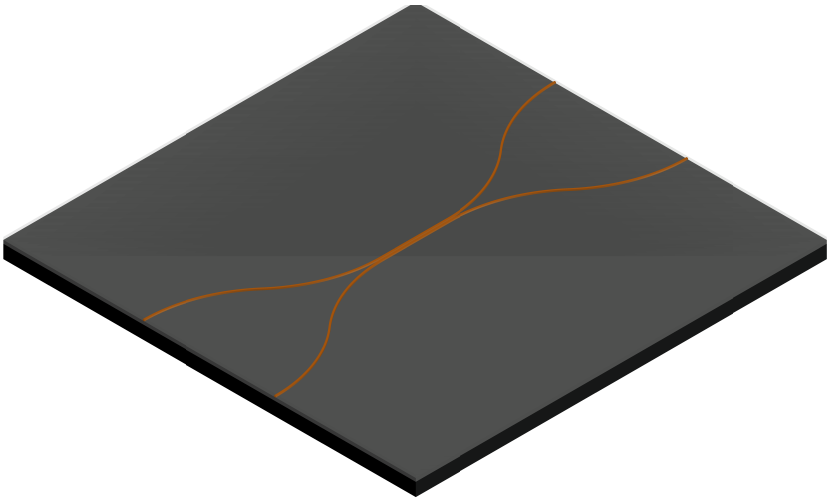

Figure 2.2: Example of Straight Directional Coupler.

Star couplers

The free-propagation region, more commonly referred to as star coupler, employs the optical beam diffraction to split the light [74]. In a star coupler, the input light is launched in a slab waveguide and it starts to expand following the Gaussian beam propagation. If the output waveguides are placed to collect the power of the expanded Gaussian beam, the losses of this element could be low for a high number of outputs [75]. In addition, the Rowland Circle is typically used to distribute the

optical power with the same phase, thus being the basis of the AWG [20]. Indeed, they are the best power splitters when a high number of outputs are needed, as the losses due to the power overlap in the arrayed waveguide are lower than other approaches based on a cascade of 1x2 or 2x2 power splitters. Primarily, the important parameters to design these elements are: the width of input/outputs of the star coupler, the amount of power to collect at the arrayed waveguide, the gap between waveguides and the length of the free propagation region. Finally, in order to improve the response of these elements, different techniques were studied. The most remarkable ones are: following a tangential pitch of the output waveguides to reduce the aberrations of the star coupler [76] and reducing the reflections inside the star coupler [77].

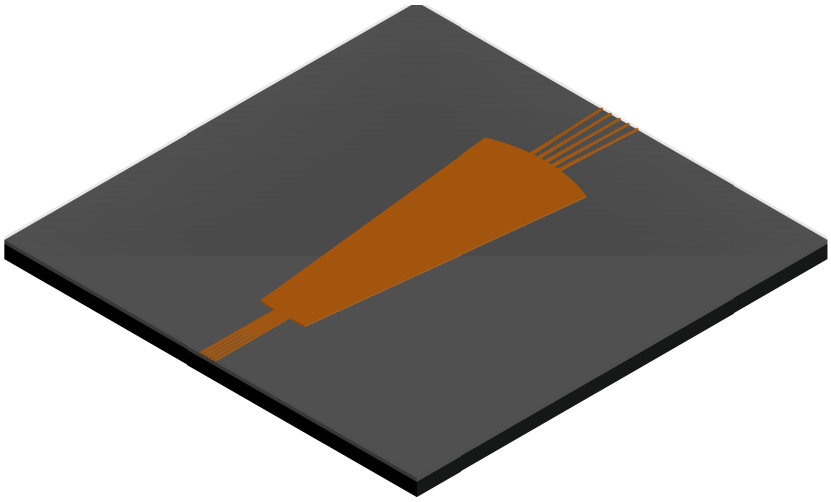

Figure 2.3: Example of Straight Directional Coupler.

Multimode interferometers (MMI)

The MMI is the most widely used splitter in integrated photonics since the first description by Soldano [78]. The operation mechanism of this element is based on the self-imaging and the most important parameters are the access waveguides width, the number and position of input/output waveguides, the cross-section and the MMI body width and the length and gap of the fan-outs of the MMI. Due to the intrinsic properties of this element such as broadband operation and fabrication tolerance[79], [80], MMI is the most common used element. Different design techniques were developed to improve the design such as: notching the edges to reduce reflections [81]–[83] or tapering to obtain different splitting ratios [84], [85].Recent developments also use inverse design to optimize these elements for high performance, fabrication tolerance and compact implementation [86]–[90]. This element will be used in the following sections as well as in the final design

due to their properties. In the next section, a new design flow describing how to design a standard MMI is reported.

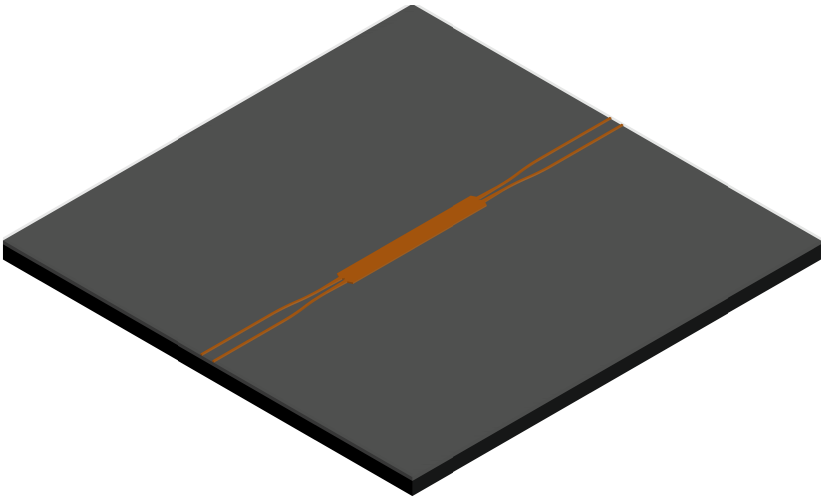

Figure 2.4: Example of 2x2 MMI.

2.2.2 Rethinking the design flow for the MMI

The traditional flow for MMI design begins by choosing the desired number of inputs and outputs and the splitting ratio according to the specifications. Then, a MMI width that influences the inputs and outputs positions and the length of MMI is chosen, following the article of Soldano[78]. Finally, an iterative simulation is performed to adjust the MMI length, the positions and the width of the inputs and outputs to maximize the transmitted power and the desired splitting ratio. However, this methodology leaves the choice of a width for the MMI body and the access waveguides width to the designer's discretion. On the one hand, the width of the MMI limits the wavelength bandwidth and insertion losses. Therefore, the narrower the width of the MMI is, the larger its operational bandwidth is. On the other hand, the width of the access waveguides reduces the losses of the MMI. The losses are produced by the number of the higher order modes excited in the multi-mode section. The wider the input mode in the multi-mode section is, the lower the number of excited modes are. Therefore, the amount of the power concentrated at the edges of the multi-mode section is lower. This amount of optical power concentrated at the edges of the waveguide is the main contribution of the losses. This is because the irregularities in the edges of the waveguides produce radiation losses of the optical mode [91]–[93]. In fact, this effect is important in AWGs because it produces amplitude and phase imbalance between waveguides [94]–[96]. Furthermore, some important parameters are the length and gap of fan-outs of the

device. The coupling between waveguides reduces the performance of the device shifting the response or adding an extra length that changes the target splitting ratio [97]. In MMIs, this coupling effect limits how narrow the body width of the MMI is. The coupling effect is related to the width and length of the MMI's body access waveguides so it is the first step for the new design structure of an MMI. Figure 2.5 shows a detailed description of the proposed design flow.

First, the material platform and the input waveguide width are chosen. Second, the type of the MMI, how many inputs and outputs are needed. Third, the cross-section in the material platform that is more suitable for the application is selected. Fourth, the width of the access waveguides to the multi-mode section is decided. This limits the amount of higher order modes that are excited in the multi-mode section. Fifth, the gap between access waveguides and taper length between input and access waveguide is studied to have the best performance. The gap and width of access waveguides limits the minimum width of the multi-mode section. Also gives the maximum length to avoid coupling between the waveguides. A simulation must to carried out to obtain the best performance. Sixth, the width of the multi-mode section is decided. The wider the multi-mode section, the narrower is the wavelength operation and higher the excess losses. Seventh, the length of the MMI is calculated starting with Soldano formulas for the desired splitting ratio and simulating to obtain the suitable point. Finally, the design flow is iterated until the splitting ratio, imbalance and excess losses for wavelength range desired are suitable.

Similar conclusions have also been reached by other authors to design this device previously [97]. To compare the new design flow, that with the traditional one, a 2x2 MMI simulation was carried out. On the one hand, in Fig. 2.6a it can be observed that the coupling between the input/output waveguides could produce an undesirable splitting ratio. On the other hand, in Fig. 2.6b the design follows the new flow avoiding the coupling.

Using the design flow described, a new MMI 2x2 has been designed, fabricated and tested to compare with the old implementation that follows the traditional design based on the CNM-VLC platform [40].

Figure 2.7 shows an example of the normalized response of the old MMI in the CNM-VLC platform and the new MMI following the strategy described. Different measurements were carried out for different dies along different wafers showing the same differences in the power response. Due to the fan-out coupling, the response of the old MMI is shifted to another division with high variability. Regarding the excess losses, in both cases they are less than 0.5 dB in all measurements [56].

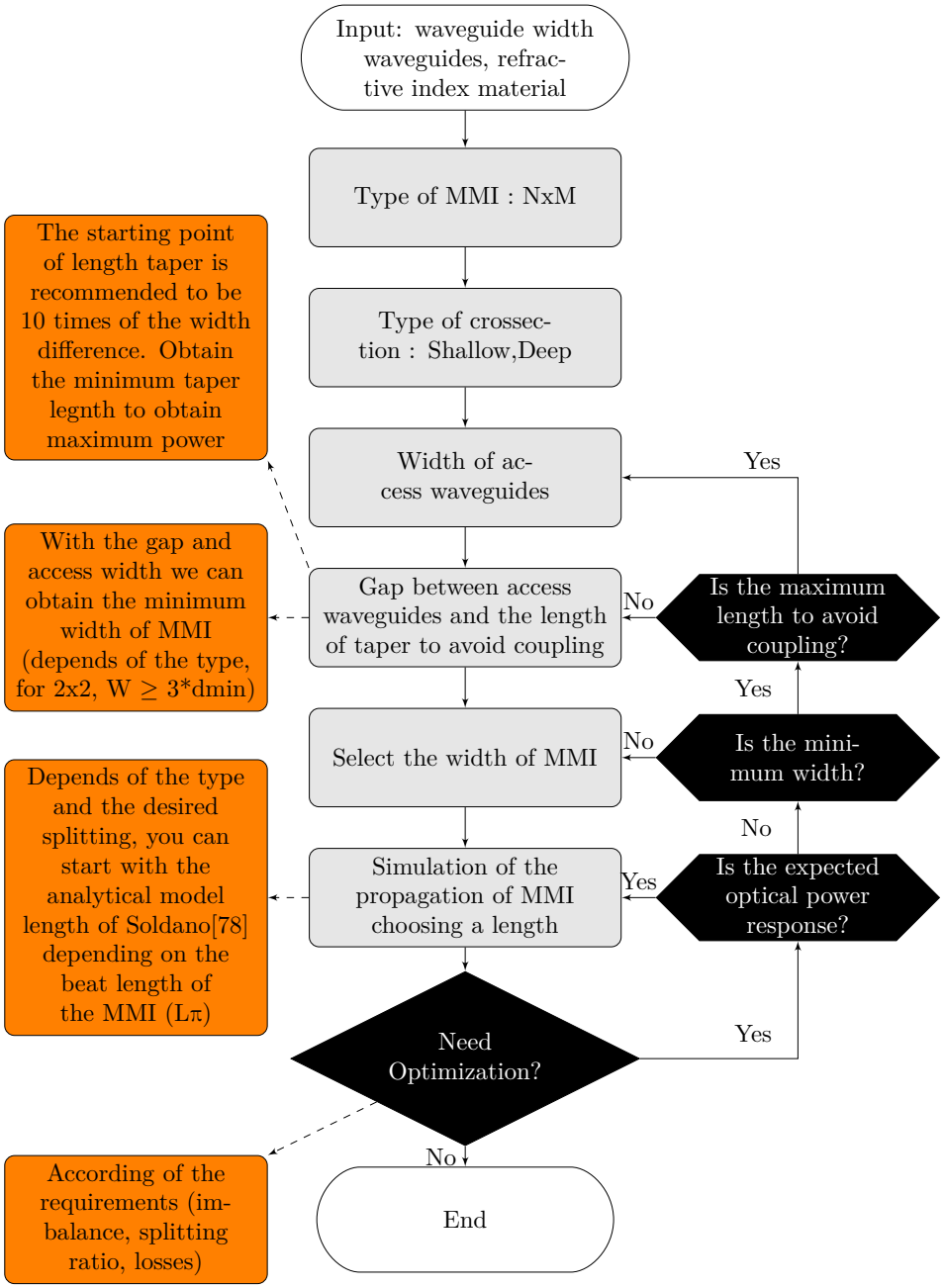

Figure 2.5: Prepared design flow.

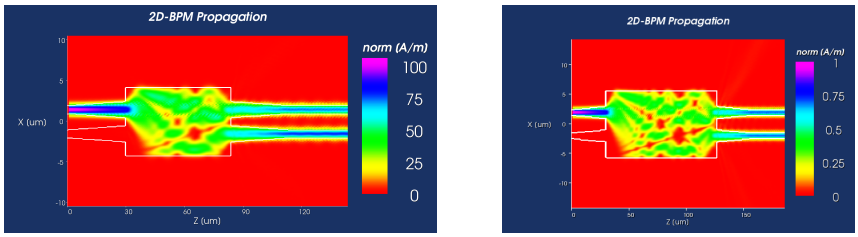

(a) Bouncing behaviour at the output **(b)** Perfect alignment of the images

Figure 2.6: BPM simulation of a 2x2 MMI. (a) with coupling and (b) without coupling between the output waveguides.

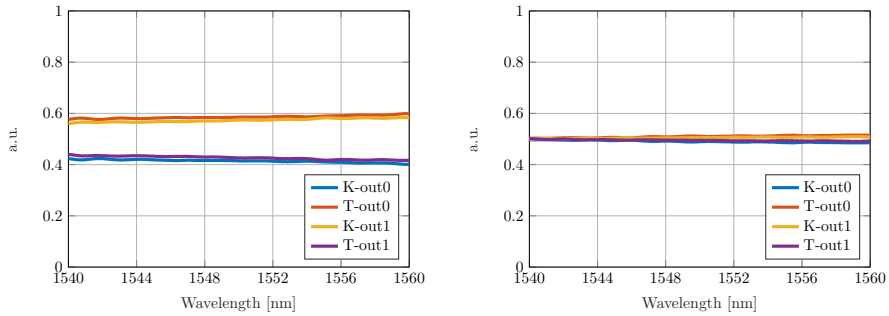

(a) Splitting ratio of old version of MMI **(b)** Splitting ratio of new version of MMI

Figure 2.7: Normalized measurements of the output distribution of old and new version of 2x2 MMI.

2.3 Couplers

Optical coupling to the chip is one of the main source of insertion losses in devices implemented in PIC. Over the years, it is a hot topic since there are different implementations to try to sacrifice the minimum possible space and obtain the best performance [98]–[100]. Any design for PIC coupling seeks to have losses below 1 dB for a standard SMF28 fiber that has a MFD of 10.4 µm at a wavelength of 1550 nm. In addition, alignment tolerance, low reflectivity, and independence of input polarization are extra properties to consider. This is a requirement for significantly reducing the price of the packaging and it simplifies the whole process [101]. To sum up, there are two main ways of joining fibers, fiber arrays or any optical input to the PICs: horizontal and vertical coupling[99].

Nowadays, the vertical coupling is the preferred for wafer level test that it is used to characterize manufacturing in mass production [102]. However, for final products with electrical connections, there is a trend towards horizontal coupling due to: the increased complexity of the circuits which forces a more complex implementation using flip-chip or a large amount of wire-bonding, which makes vertical light coupling impossible, the lower losses compared to vertical coupling,

insensitive polarization and its broadband operation [103].

2.3.1 Implementations

As explained in the introduction, there are two main approaches for efficiently coupling light to the chip: vertical or horizontal.

Vertical coupling

The main device for vertical coupling is the grating coupler [99]. Grating couplers are periodic structures that radiate light at a specific vertical angle depending on their period [104]. The best thing about this element is that it is easy to couple light with a large MFD because it only depends on the width of the waveguide. In addition, despite its intrinsic problems, designs below 1 dB insertion loss for 10.4 µm MFDs for more than a 30 nm wavelength range have been achieved [99], [102], [105]–[107]. There are other approaches that relate to additional post-processes outside the standard processes such as 45º mirrors [35] or elephant couplers [108]–[110].

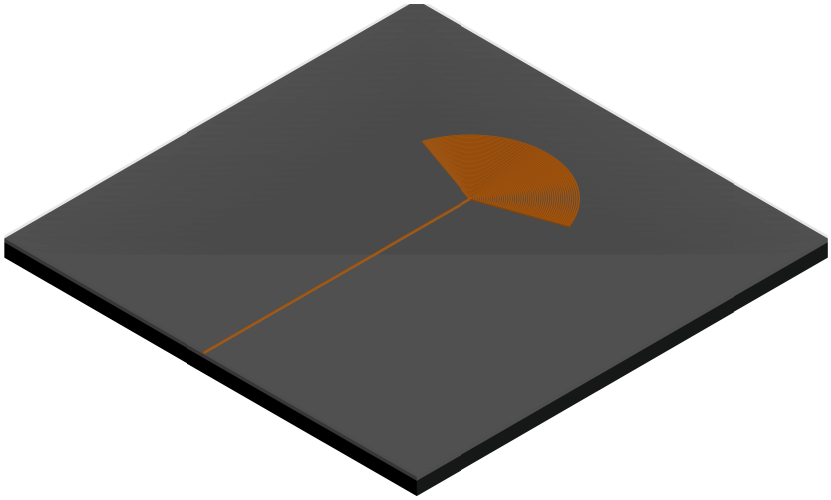

Figure 2.8: Example of Grating Coupler.

Edge coupling

In edge coupling, the main problem is to expand the MFD to achieve the specification in the smallest possible area. The main notable implementations are: inverted tapers, trident couplers or multiple waveguide/layer couplers, Spot Size Converter (SSC), evanescent couplers and photonic wirebondings or interposers [99], [100].

First, the inverted tapers, trident/multiple waveguide couplers and spot size converters have different names, but the implementations are quite similar because they try to expand the mode with different strategies. The inverted tapers are based on the fact that if the waveguide is reduced, the fundamental mode of waveguide begins to expand. Furthermore, the best thing about this approach is that, due to the optical power is less confined in the waveguide and more confined in the surrounding material, the reflections are lower due to the intrinsic lower effective index. However, it is really difficult to expand MFDs to larger ones as SMF28 by only using this technique. Expanding the MFD by sacrificing the low index contrast can be achieved by employing multiple waveguides or multiple layers to expand the mode. By doing a transition between the single mode waveguide and the multiple waveguides, it is possible to excite a supermode that has a larger MFD. To conclude this paragraph, the SSCs involves a transformation to a SMF28 MFD with a special process to expand the mode. Edge couplers such as inverted tapers or trident couplers try to be a SSC, but usually for narrow MFD. There are several approaches using different materials, subwavelength gratings, structures and configurations trying to have low-loss, insensitive polarization and broadband wavelength operation. Together with SSC, the most common option is to use V-grooves to place the fibers or array of fiber directly in the chip [100].

Second, the evanescent couplers exploit the intrinsic properties of the electromagnetic fields to couple the optical power between the fiber and the waveguide in the PIC. Otherwise, this technique needs the fiber attached to be tapered, which makes it really sensible to the misalignment in any direction [111]–[115].

Finally, the latest and newer implementations are the use of the interposers and photonic wirebondings. On the one hand, interposers are other SSCs fabricated on purpose to have low losses with fiber coupling and guide the light to the desired PIC with low losses. This technique requires packaging efforts but extends the possibilities of combining different chips with different substrates in the same platform. It follows the same approach as electronics and the use of a common low loss substrate, a Printed Circuit Board (PCB), that connects the high performance components obtains high performance of each element and diversify the production by reducing the costs of each element and the total price of the assembly [112], [116]–[118]. On the other hand, the photonic wirebonding is a technique using a special polymer as ORMOCER [119] which allows you to make photonic 3D print connections between each element of your complete system [120]–[122]. Nowadays, there is already a company that markets a machine that implements this process automatically, which allows to enter the production processes of integrated optical devices [123].

In the next section, an inverted taper was designed and fabricated with a standard process of CNM-VLC, that improves the reported losses of the previous version of edge coupler. An SSC design was also proposed using the SU8 as a coating to have low losses for the standard fibre optic input.

2.3.2 Edge coupler

To improve the PIC coupling in the CNM-VLC platform that has broadband operation, an edge coupler was proposed. As described in Section 2.3.1, edge couplers are the best solution to have broadband wavelength operation. To implement these structures in the CNM-VLC platform, an edge coupler is proposed by using the existing lithographic steps of the generic platform. This means that additional post-processing steps are not required, but instead the different levels of nitride etching are used. The device and some simulations made in order to show the chosen implementation are described below.

To start the design of the inverted taper, input, output mode and wavelength are defined. The central wavelength of this design is 1550 nm. The input mode is from a standard lensed fiber (2.5 µm MFD) and the output mode is the standard waveguide of the platform a 1 µm deep waveguide width. Both polarizations can be studied to find the best solution to couple light with the lowest Polarization Dependent Loss (PDL), but the recommended polarization used in the platform is TE polarization. The other building blocks are designed for TE polarization. So this edge coupler will be designed to minimize TE polarization losses. The next step is to analyse which cross-section and waveguide width are the best to have the lowest possible losses. The overlap integral [124] is calculated for different widths for the three possible cross-sections and the input MFD.

$$\Omega = \frac{\left| \iint E_f\left(x,y\right) E_w\left(x,y\right)\, dxdy \right|^2}{\iint \left|E_f\left(x,y\right)\right|^2 dxdy \iint \left|E_w\left(x,y\right)\right|^2 dxdy} \tag{2.1}$$

Where $E_f\left(x,y\right)$ is the Gaussian approximation of the input mode and $E_w\left(x,y\right)$ is the waveguide mode solution. Figure 2.9a shows that the best cross-section to reduce the overlap integral losses is the mini-deep waveguide. In fact, there is a 750 nm waveguide width sweet spot that obtains losses of 0.35 dB. After finding the cross-section and the waveguide width at the facet, the next step is to find the way to have a good match between the mini-deep waveguide cross-section and the deep cross-section (the output waveguide). Another overlapping integral was carried out with different widths between both cross-sections to reduce the losses of this interface as much as possible.

As shown in Fig. 2.9b, the losses are reduced when the deep waveguide width is decreased and the mini-deep waveguide width is increased. As it can be seen in the above figure, above 1 µm waveguide width of mini-deep waveguide, losses are not significantly reduced. The explanation for this behaviour is that the mode size of the deep waveguide is larger than for the mini-deep waveguide. Therefore, in the graph, the optimum point is for widths of 1 µm for mini-deep cross-section and 0.6 µm for the deep cross-section. By having the widths of each waveguide in each interface, the last step is to design the transitions in each cross-section between the waveguide widths. Propagation simulations were done for the entire structure with the FIMMWAVE/FIMMPROP tool of Photon Design [125], which employs the Eigenmode Expansion Method (EME) [126], [127]. In the first taper, the mini-deep taper starts with 750 nm width and ends with a 1000 nm width,

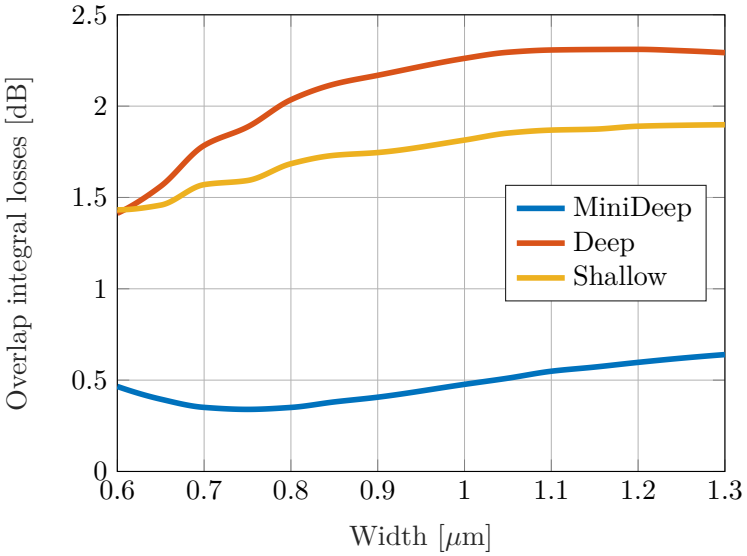

(a) Cross-sections response with a 2.5 µm MFD in TE polarization.

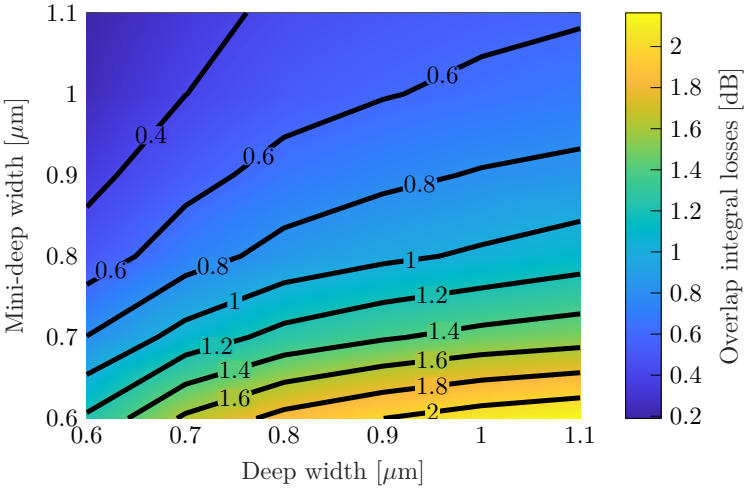

(b) Overlap between deep waveguides and mini-deep waveguides.

Figure 2.9: Overlap calculations.

whilst the deep taper starts with a 600 nm width and ends with a 1000 nm width.

Figure 2.10 shows that the power response of the device depending on the length of linear taper of each section. The dashed line shows the total power transmitted by varying the length of the first taper in mini-deep cross-section for

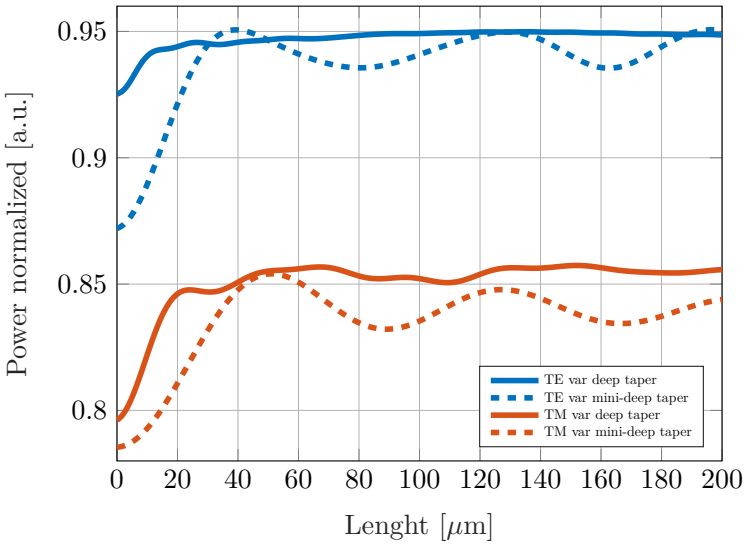

Figure 2.10: Output power for different taper lengths for mini-deep and for deep cross-sections.

a fixed length of 100 µm of deep cross-section taper. Also, the solid lines of the figure show the results for a fixed length of 50 µm of mini-deep taper and varying the deep taper. Moreover, together with the TE polarization response, the TM polarization is shown demonstrating the low PDL of this structure. Interestingly, the graphs show how the power fluctuates with the mini-deep taper length. At 45 µm taper length, the TE polarization shows a maximum power transmission. The mode conversion for some of the lengths as well as some mismatch between the two sections could produce the oscillating behaviour in the power transmitted vs taper length. In fact, Fig. 2.11 shows that the second order TE mode exhibits a minimum for the mentioned 45 µm mini-deep taper length.

Figure 2.11 shows how to increase the length to suppress the higher order modes. The maximum power transmission is obtained with 100 µm length of the deep cross-section and mini-deep taper of 45 µm length, according to the above simulations. Therefore, the taper lengths chosen to maximize the TE coupled power are: 45 µm length for the mini-deep taper and 100 µm length for the deep taper. That configuration yields 0.23 dB excess losses with 20 dB suppression of the higher order modes in simulations. The final insertion losses for this structure for a 2.5 µm MFD input will be about 0.58 dB, taking into account that the losses of overlap integral will be 0.35 dB. The final implementation of the edge coupler is shown in Fig. 2.12.

The results obtained assume does not take into account the fabrication imperfections that may arise from the manufacturing. For this reason, different parameters are scanned in reasonable ranges analysing the impact on the overall coupling

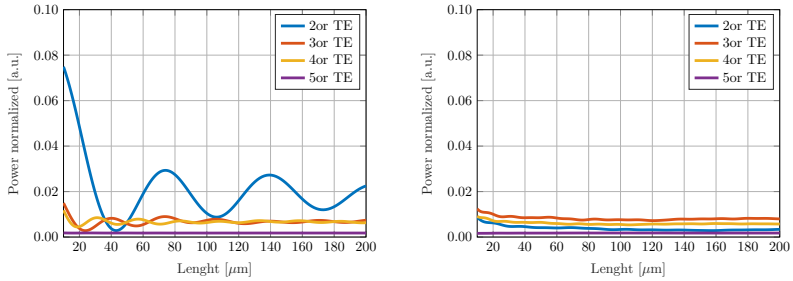

(a) Mini-deep cross-section taper **(b)** Deep cross-section taper

Figure 2.11: Total output power of different high order modes launching the first order mode for different taper lengths.

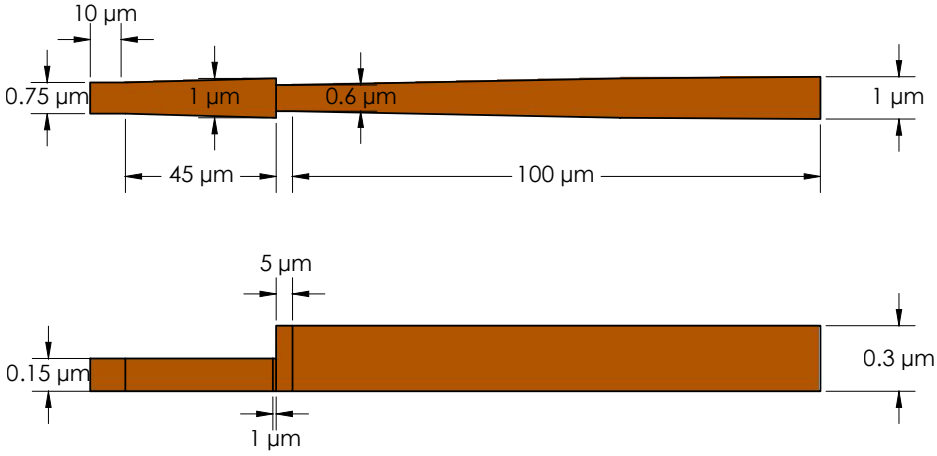

Figure 2.12: Final implementation of the inverted taper.

losses. In order to define the deep and mini-deep cross-sections in lithography, two masks, which have to be aligned, are needed. The impact of possible misalignments is studied by introducing a straight a deep section between the two tapers. The misalignment can only occur in the longitudinal direction, as the mini-deep is actually done with the same deep mask, but without the shallow mask protection. Figure 2.13 shows the response of the structure if mask alignment error of 1 μm is produced. In the worst case scenario, an additional 0.4 dB loss will be introduced for the TE polarization due to mask misalignment. Another source of losses is the different MFD due to the fabrication of the lensed fiber or if it is damaged. The next figure shows the different overlap integral losses if the MFD changes for different cross-sections and widths. As it can be observed in Fig. 2.14, the mini-deep cross-section results in the lowest insertion loss for a nominal 2.5 μm MFD, as well as low loss variations for MFD changes between 2 and 3 μm.

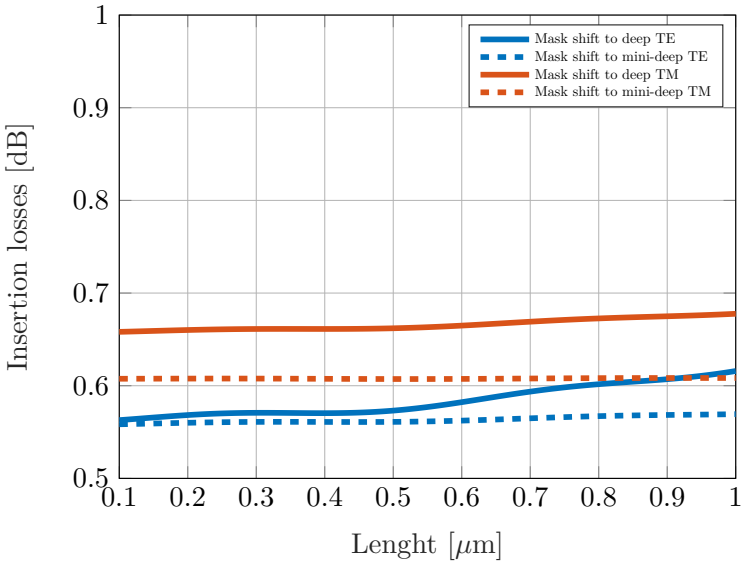

Figure 2.13: Shallow mask shifted toward the deep and minideep cross-section.

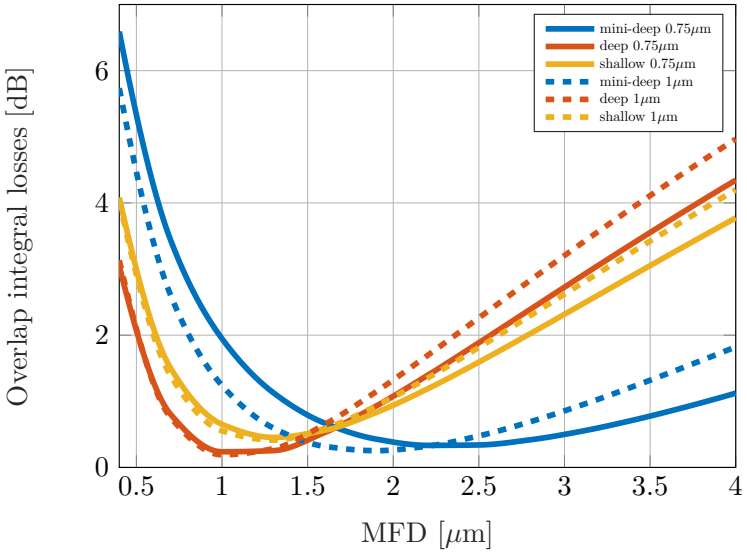

Figure 2.14: Overlap integral losses dependency with MFD for different cross-sections and waveguide widths.

In the worst case, the losses due to the overlap integral will be around 0.5 dB. Furthermore, the misalignment of the lensed fiber with respect to the waveguide center is explored. The structure shows robustness against misalignments in the

X and Y axes. To show the response of this device to misalignment, an offset in both directions of 1 micron (almost half of the MFD) is introduced and the response for different MFDs that would emulate the misalignment in the Z direction (which would be the longitudinal and the distance between the lensed fiber and the inverted taper)is calculated. Figure 2.15 shows overlap integral losses due

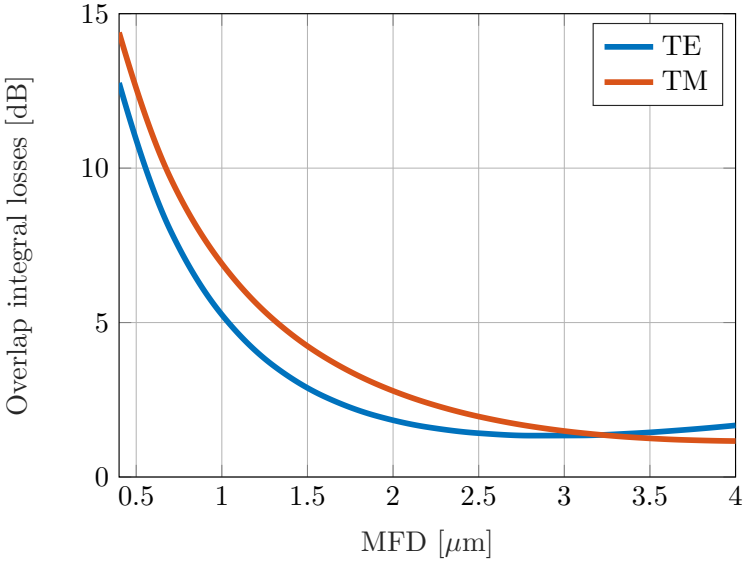

Figure 2.15: Extra losses introduced for 1 µm offset in X and Y direction for TE and TM polarization.

to the maximum allowed misalignment of 1 µm offset. The incident MFD could be between 2.0 and 3.0 µm, which losses are below 1.82 dB. As it can be seen, the change in MFD does not have a considerable contribution to the excess losses when compared to the misalignment in X and Y direction. Finally, in order to show the broadband wavelength operation of this structure, the losses versus wavelength are calculated in Fig. 2.16. The maximum change is around 0.06 dB in the wavelength range from 1510 and 1610 nm (C and L band). This design has been fabricated in the MPW of CNM-VLC. An end-fire measurement setup with microscope objectives with 2.5 µm and polarizers to inject and collect TE polarization is used to characterize the fabricated devices. The design is composed of two edge couplers, each on opposite sides of the chip, and a deep straight waveguide of 1 µm width between them. An Amplified Spontaneous Emission (ASE) broadband source was used to measure the response, along with an Optical Spectrum Analyzer (OSA). All measurements are normalised to the spectrum of the face to face direct coupling between objectives. The results are shown in Fig. 2.17 for both a straight waveguide with and without two inverted tapers. The fiber-to-fiber loss is 3.635 dB when inverted tapers are employed. The measured propagation loss

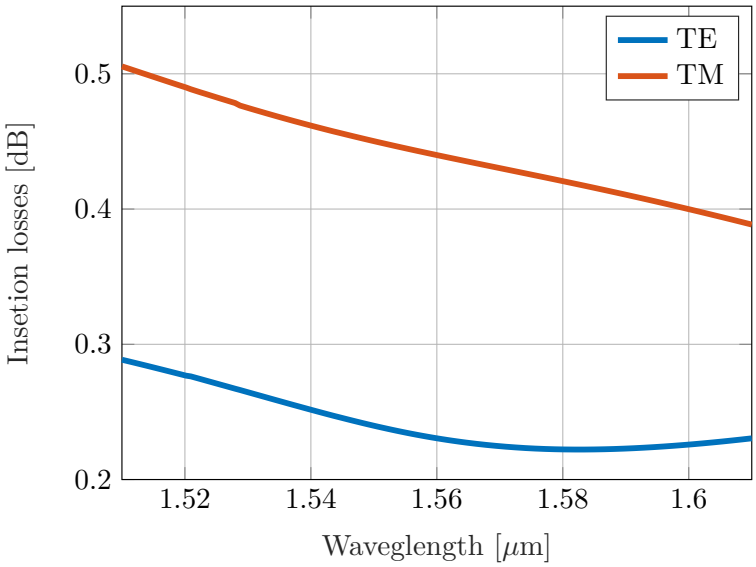

Figure 2.16: Wavelength dependence of insertion losses introduced by inverted taper.

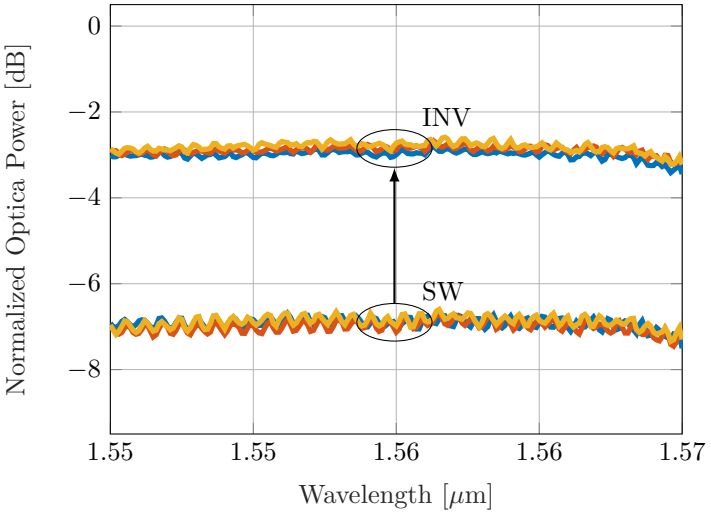

Figure 2.17: Fiber to fiber TE transmission measurements for test structures with (INV) and without (SW) inverted tapers.

for the deep 1 µm width straight waveguide is 1.41 dB/cm [34]. The length of the straight section is 4998 µm, that is to say, 0.7 dB of propagation loss. In conclusion, each edge coupler has an insertion loss of 1.47 dB for the TE polarization. The power response predicted by simulation is 0.58 dB and a plausible reason for

the mismatch is explained below. First, the wafers were stealth diced 25 µm inside the die reducing the mini-deep taper. The result width due to the dicing is 0.9 µm and the simulations shows an additional overlap coupling loss of 0.405 dB for TE polarization. Furthermore, the new taper length increases the taper loss to 0.351 dB. Then, the width variations in the lithographic processes are of the order of 100 nm which could introduce losses of 0.295 dB. In summary, the insertion losses in the worst case of width variations may reach 1.051 dB. Furthermore, due to the mask alignment, 0.4-0.5 dB insertion losses could be added. All these loss sources could explain the experimental 1.47 dB vs the 0.58 dB predicted at the design stage.

2.4 Conclusion and future

Basic building blocks of splitters and couplers have been discussed in this chapter. As a result of this analysis and based on the CNM-VLC platform, splitters and an edge coupler have been developed. The splitters developed are based on MMIs structures, making a novel design process that improves splitter performance and increases the device tolerance to fabrication imperfections. The MMI 2x2 has been designed and tested by comparing it with the standard MMI provided in the platform PDK, thus improving the amplitude unbalance of the device as well as the robustness against fabrication deviations. On the other hand, an edge coupler to a lensed fiber has been designed by using the two levels of etching, showing losses about 1.4 dB per edge coupler despite the fact that part of these losses (about 0.8 dB) are due to an error in the dicing of the dies. This also shows that this is a coupler with less than 1 dB per facet that is in the state of the art of silicon nitride technologies.

As future work in this chapter, work is being done on an improvement of the edge coupler combined with material SU8 [128] (a high strength material used for photonic applications) in order to match the 10.4 µm MFD SMF28 fiber standard. The simulations predict 1 dB of loss and could be a great improvement to facilitate coupling to the chip with low insertion loss. On the other hand, grating coupler designs have also been made by estimating about 7 dB per grating coupler for an input angle of 10°, which would be a great achievement, given the manufacturing limitations of the stepper used in the lithography [129].

Chapter 3
Tunable Photonic Integrated Mirrors

The integrated reconfigurable reflectors are elements that allow the amount of optical power reflected to be configured. This is the key component for the R-RAWG which will be described in the next chapter. In this chapter, the possible implementations in the literature will be presented, highlighting one of them, the reconfigurable reflector with splitters, phase shifters and loops. This implementation is the best to be manufactured on any platform without the need for extra process steps, and much more controllable to have a fully integrated device. However, it is a device that has been underdeveloped over the years and has been forgotten by the literature in the world of photonic integrated circuits as a tunable integrated mirror. Therefore, this chapter will show different ways to implement reflectors with loops and their theoretical responses by developing a formulation and code to emulate ideal responses of these devices. Finally, the amplitude and phase response measurements of an implementation of this device will be presented, controlling both parameters thanks to the simulator developed, thus demonstrating its versatility and its suitability to reconfigure a RAWG. Some parts of following chapter were previously published in a master's thesis and at a congress and are reprinted here with permission [43], [56].

3.1 Background and Motivation

There are several ways to make a reconfigurable integrated reflector in PICs. This chapter is motivated by the fact that for the design of R-RAWG, the reconfigurable reflector is the key to its proper operation and ideally should have a response as flat as possible in wavelength. In the literature, there are four main possible implementations: external mirrors, Bragg mirrors or periodic structures, metallized surfaces and feedback structures. In the next section each of them will be explained

in detail with its advantages and disadvantages.

Reconfigurable reflectors are not a well studied device in the silicon nitride or silicon platforms since they are normally used for lasers in InP platforms, in which implementations are based on post-processes such as metallizations or on external devices because the area is limited and the radius of curvature is very large [130], [131]. Today, thanks to the hybrid approaches of technologies, some development of reconfigurable reflection structures based on loops is observed, especially in silicon nitride due to its low propagation losses [132], [133].

However, at the beginning of this thesis it was found these devices, which are the ideal ones for the implementation of an R-RAWG, were poorly developed, with few experimental demonstration of the theory, and they are mainly focused on the Sagnac effect [134]–[140]. Therefore, this chapter arises from the need to simulate the response of the reflectors with loops, to obtain their characteristics and to predict the response of the measurements in order to have a clear picture of what can be expected when this device is introduced into the R-RAWG.

3.2 Implementations

The ideal reflector specifications for the R-RAWG are mainly: flat wavelength response, low loss and control the amplitude and phase of the reflection to be able to correct any errors that may occur and also to reconfigure the system. In the literature, there are different approaches to achieve this reflector but the following stand out above all: configurable external mirrors, periodic structures like DBRs, metallic/reflective surfaces on chip and the use of splitters with loops.

3.2.1 External mirrors

Historically and also due to the heritage of free space optics, the first possible reflectors are the based on Fresnel reflection. By using a stack of material layers on a surface, depending on the refractive indices, the thickness of the materials and the angle of the incident light, a very high reflection performance can be achieved with low losses. The main electromagnetic wave reflectors are metals and are widely used for reflective surfaces such as mirrors [141]. This leads to the first possible implementation which is the use of a mirror outside the chip. A micro-metric mirror can be used as a reflector for the integrated device. These mirrors also have Micro-Electro-Mechanicss (MEMs) allowing them to vary their angle and thus vary the reflection introduced. These devices are used, for example, for extended cavity lasers that need a very high control of reflections [141], [142]. Nowadays, reconfigurable micro-mirrors are commercial products for various applications [143].

As can be seen in the Fig. 3.1, which shows an example of implementation of this type of mirrors, it is an element external to the circuit and of considerable size. This device implementation is complex, specially from the packaging point of view if a large number of ports is required like it's the case of the AWGs. This

Figure 3.1: Example of Reconfigurable micro-mirrors [143].

approach has already been used to configure the phase of a whole RAWG [144], and as you can see this solution is designed to compensate the displacement of the central wavelength due to temperature and not to reconfigure an AWG.

3.2.2 Periodic structures

Periodic structures are elements that have been studied in depth over the years due to their multiple applications. In fact, a periodic structure can introduce a spatially located dispersion and thus act as a filter, which is what is used within an Optical Spectrum Analyzer (OSA) [145]. In the PICs, techniques have been developed to be able to define them at the waveguide level and they are mainly used because of the finesse in the reflection band and its high FSR required in applications such as lasers [146]. One implementation of this type of periodic filters are the Distrubuted Bragg Reflector (DBR) as shown in Fig. 3.2 [147]. Moreover, there are also structures called photonic crystals that can be used as reflectors [148]. They are based on the using of periodicities and patterns through the waveguide to create rejection bands to obtain the desired response [149].

These structures have been used to make high-bandwidth reflectors (over 120 nm reflection band) which, combined with an interferometer and phase shifters, allow amplitude and phase control. However, these structures usually require specific manufacturing processes, and/or a very controlled manufacturing, because otherwise the final response of each element could be greatly modified. These structures are fabrication-dependent and could also introduce additional losses. Despite this, there are examples of a RAWG based on DBR [150], [151] and photonic crystals [152], [153] that demonstrate that thanks to these structures the design can be compact.

3.2.3 Metallic/reflective surfaces

Following the idea of external mirrors, processes were developed to deposit a metallized layer on the walls of an optical waveguide. this results in a surface with a total reflection that can be used for various applications, from mirrors at 45° to cavities based on these mirrors [35], [154], [155]. Moreover, an interesting approach

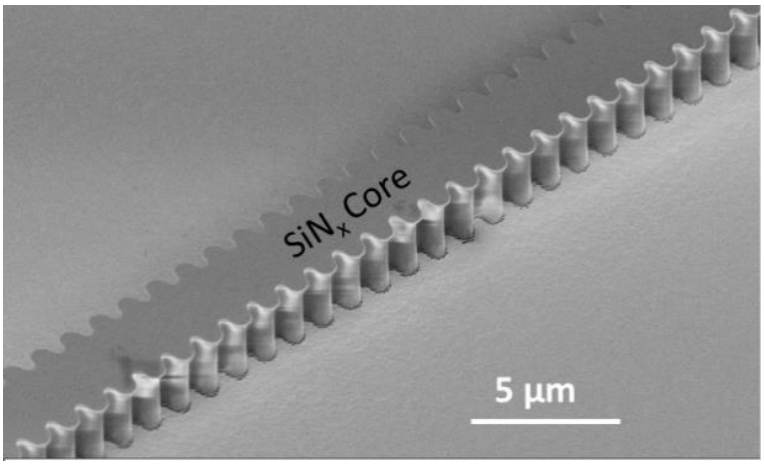

Figure 3.2: Example of periodic structures [147].

to the use of reflective surfaces is the MMI reflector (MMIR) [156]. This device is based in a 2x2 ports MMI where the output waveguides have been replaced by a 45 degrees (in-plane) etched surface. By choosing the appropriate configuration of the MMI, the incident light can be redirected back to each of the input ports [157]. Like periodic structures, if these elements are introduced into an interferometer,

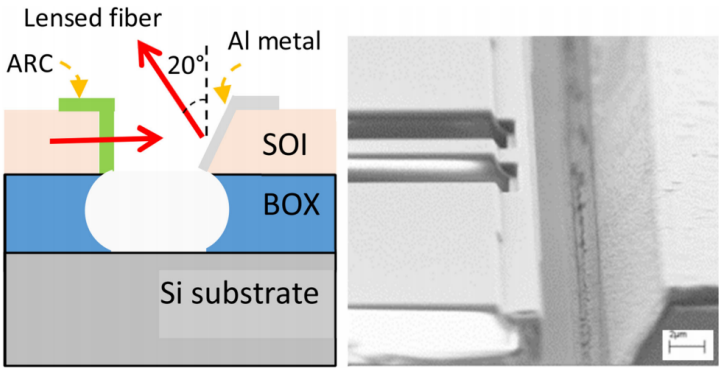

Figure 3.3: Example of metallic/reflective surfaces [35].

amplitude and phase can be controlled. However, this implementation has some problems: repeatability and fabrication is a challenge with customised process for it, the response is highly dependent on the verticality of the the walls because any inclination can lead to the excitation of unwanted higher modes and any deposition of material on the waveguides results in additional losses due to absorption [158]. Nonetheless, there are examples of proposed RAWG designs based on MMIR [159]

and simple metallized surface [160]–[162].

3.2.4 Loop mirrors

These mirrors are based on the loop of the outputs of a splitter to ensure that the optical power is reflected. This device was really thought as an implementation of a Sagnac interferometer, but it can also be used as a simple reflector [134]–[140], [163]. If a broadband splitter is employed, a low-loss reflector device for a large bandwidth can be obtained.

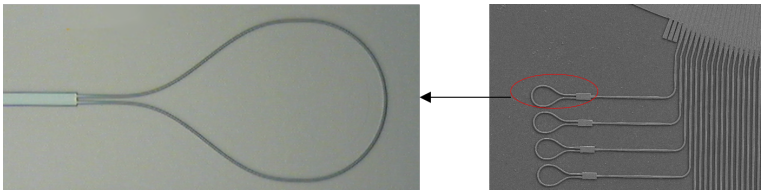

Figure 3.4: Example of loop mirrors [163].

Like other reflectors, this devices can be combined in an interferometer with active phase shifters to control amplitude and phase. Nevertheless, this device does not require very complicated or high-performance manufacturing to obtain a reasonable response. In addition, if 1x2 splitters are used that intrinsically have a stable splitting at a wide bandwidth with low insertion losses, it can be very competitive with any other implementation. However, this implementation is much more space consuming than others, as it depends largely on the radius of curvature and the curve function used. Even so, very compact bends have been demonstrated by the use of euler bends for example, which allow to reduce their size [164]. The use of these loop mirrors has been demonstrated on various platforms for the implementation of a RAWG [165]–[169].

In conclusion, as the reflector and the device have to be made on the CNM-VLC platform which has quite a few limitations in terms of minimum feature size and variations in manufacturing, the option of using loop mirror has been chosen as the most suitable for manufacturing a functional device on the platform, even though it consumes much more area. In the following sections of the chapter we will introduce the formalism used for the response analysis of these devices and then their ideal response and the measurements obtained will be analysed.

3.3 Formalism

In order to study the response of these devices, a matlab-based code was developed for the simulations. The code developed is based on the use of transmission matrices coming from certain assumptions of the S-matrices of the devices [57], [170]–[172].

To analyse the response with transmission matrices, it is necessary to develop certain mathematical interpretations. First, the three-port device can be modelled as a four-port device since, as suggested by the measurement and development literature, this virtual port would collect all the optical power that removes the radiative modes and therefore complies with the matrix being unitary and without losses [57]–[62]. Second, the loop can be transformed into an operation to connect the previous device to the same device but with the port crossed, making the analysis as transmission problem using the forward and backward matrices. Third, in order to directly multiply the matrices and simplify the transmission matrices, the reflections of the same port due to the device are assumed negligible. All this was developed in depth in a previous work [56].

Thanks to the matrix formalism, any device can be analyzed simply by doing the operations with appropriate matrices, even if they include feedback. To be able to compare similar structures and see the implications of feedback, the responses are compared between MZIs with the interconnected outputs, in a configuration called Sagnac Loop Reflector (SLR). Thus, in the following section a comparison of the response is made by applying the phase shift between the arms and a constant phase in both arms.

The basic formulas of the devices are shown as an introduction to the next section. First the MZI is described with transmission matrices and the generic formulas of splitters. In this case a symmetrical MZI is used (without any incremental length inside) because the aim is to use it as a broadband amplitude and phase controller.

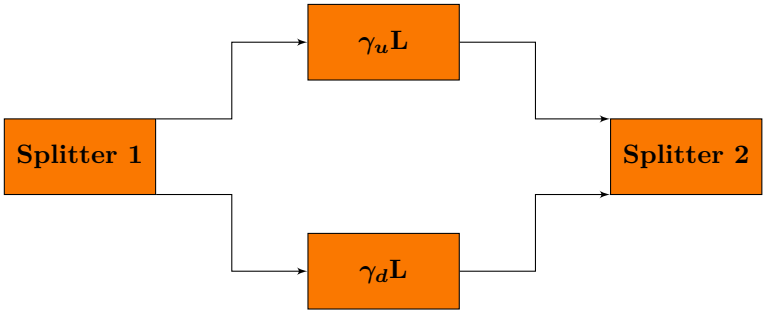

Figure 3.5: Schematic of MZI.

Where γ_d is the complex propagation constant of the lower arm, γ_u is the complex propagation constant of the upper arm and L is a constant length. There are different ways to change the propagation constants by changing the real or imaginary part. When the imaginary part is changed there is a phase change. In contrast, when the real part is changed there is a change in the attenuation per unit length. Depending on the physics of the actuator, there are mainly four mechanism:

- Thermo-optic effect. Using electrical currents and heaters on the chip, the

local temperature could be changed to modify the imaginary part of the waveguide's propagation constant without changing absorption. The value of the thermo-optic constant depends on the material used to guide the light and is a low speed effect [173].

- Electro-optic effect. This effect is the change of the optical propagation constants due to an applied electric field. It is mainly used in lithium-niobate platforms due to its intrinsic properties [174].
- Electro plasma phase dispersion effect. Due to the use of doping materials, the change in charge density leads to a phase change and the absorption of the propagation constant. This is the effect that is mainly used in silicon photonics to implement modulators [175].
- Acusto-optic effect. The interaction between photons and phonons, could produce a displacement of the propagation constant depending on the platform used. The problem is complex because a photonic and a sonic wave propagate together [176].

Figure 3.5 shows a generic MZI representation with splitters that depends on whether it is 2x2 or 1x2 the number of inputs and outputs changes. Using the general formulas of the [56], the steps to obtain the formulas are explained:

$$T_{MZI_f} = T^T_{MZI_b} = \sqrt{\sigma_1}\sqrt{\sigma_2} \begin{pmatrix} t_1 & k_1^* \\ -k_1 & t_1^* \end{pmatrix} \cdot \begin{pmatrix} e^{(\alpha+j\beta_d)L} & 0 \\ 0 & e^{(\alpha+j\beta_u)L} \end{pmatrix} \cdot \begin{pmatrix} t_2 & k_2^* \\ -k_2 & t_2^* \end{pmatrix} =$$

$$\sqrt{\sigma_1}\sqrt{\sigma_2} \begin{pmatrix} t_1 t_2 e^{(\alpha+j\beta_u)L} - k_1^* k_2 e^{(\alpha+j\beta_d)L} & k_1^* t_2^* e^{(\alpha+j\beta_d)L} + t_1 k_2^* e^{(\alpha+j\beta_u)L} \\ -k_1 t_2 e^{(\alpha+j\beta_u)L} - t_1^* k_2 e^{(\alpha+j\beta_d)L} & t_1^* t_2^* e^{(\alpha+j\beta_d)L} - k_1 k_2^* e^{(\alpha+j\beta_u)L} \end{pmatrix} \quad (3.1)$$

Where σ is the excess loss in the power response of each splitter, t is the transmission field coefficient of the splitter, k is the cross field coefficient of the splitter, α is the attenuation coefficient of the waveguide inside the interferometer as the real part of propagation constant and β is the imaginary part of the propagation constant called the phase constant.
Depending on the splitters used it is possible to distinguish between three cases:

1. Both splitters of 2 outputs and inputs.
2. One splitter of 1 input and 2 outputs and the other of 2 inputs and 2 outputs.
3. One splitter of 1 input and 2 outputs and the other of 2 inputs and 1 output.

This work explores the first two options because it allows to build feedback loop versions.

Case 1: both splitters of two inputs and two outputs

Replacing the generic values of the specifics in each splitter and making simplifying Eq. (3.2),the transfer matrix of a 2x2 MZI is:

$$\begin{cases} K_a \cong K_b \\ \alpha_u L \cong \alpha_d L \cong 0 \\ \Delta\Phi = L \cdot (\beta_u - \beta_d) \end{cases} \quad (3.2)$$

$$T_{MZI2x2_f} = T^T_{MZI2x2_b} =$$

$$\sqrt{\sigma_1}\sqrt{\sigma_2}\cdot e^{j\beta_d L_1}\begin{pmatrix} e^{+j\Delta\Phi} - 2Ke^{j\frac{\Delta\Phi}{2}}cos\frac{\Delta\Phi}{2} & -2j\sqrt{K(1-K)}e^{j\frac{\Delta\Phi}{2}}cos\frac{\Delta\Phi}{2} \\ -2j\sqrt{K(1-K)}e^{j\frac{\Delta\Phi}{2}}cos\frac{\Delta\Phi}{2} & 1-2Ke^{j\frac{\Delta\Phi}{2}}cos\frac{\Delta\Phi}{2} \end{pmatrix} \quad (3.3)$$

Case 2: one splitter of 1 input and 2 outputs and the other of 2 inputs and 2 outputs

Applying the same methodology of the previous case the transfer matrix of a 1x2 MZI is:

$$\begin{cases} K_a \cong K_b \\ \alpha_u L \cong \alpha_d L \cong 0 \\ \Delta\Phi = L\cdot(\beta_u - \beta_d) \\ \nu = \frac{\Delta\Phi}{2} - \frac{\pi}{4} \end{cases} \quad (3.4)$$

$$T_{MZI1x2_f} = T^T_{MZI1x2_b} =$$

$$\sqrt{\sigma_1}\sqrt{\sigma_2}\cdot e^{j\beta_d L_1}\begin{pmatrix} 1-2Ke^{j\nu}cos\nu & -2j\sqrt{K(1-K)}e^{j\nu}cos\nu \\ -2\sqrt{K(1-K)}e^{j\nu}cos\nu & -j(e^{j2\nu}-2Ke^{j\nu}cos\nu) \end{pmatrix} \quad (3.5)$$

Finally, thanks to the theory developed, it is straightforward to obtain the feedback loop version.

Case 1: SLR-2x2

Using the Eq. (3.3)

$$T_{RSL-2x2} = T_{MZI2x2_f}\cdot\begin{pmatrix} 0 & e^{\gamma_2 L_2} \\ e^{\gamma_2 L_2} & 0 \end{pmatrix}\cdot T_{MZI2x2_b} \quad (3.6)$$

Being γ_2 the complex propagation constant in the loop and L_2 the length of the loop. To obtain the reflection in the same port and the transmission, it is possible to operate the transmission matrix as mentioned in [170].

$$\begin{cases} r = \frac{T_{21}}{|T_{RSL-2x2}|} \\ t = \frac{T_{22}}{|T_{RSL-2x2}|} \\ R = r\cdot r^* \\ T = t\cdot t^* \end{cases} \quad (3.7)$$

Case 2: SLR-1x2

Using the Eq. (3.4)

$$T_{RSL-1x2} = T_{MZI1x2_f}\cdot\begin{pmatrix} 0 & e^{\gamma_2 L_2} \\ e^{\gamma_2 L_2} & 0 \end{pmatrix}\cdot T_{MZI1x2_b} \quad (3.8)$$

Following the equations Eq. (3.7)

$$\begin{cases} r = \frac{T_{21}}{|T_{RSL-1x2}|} \\ R = r \cdot r^* \end{cases} \tag{3.9}$$

These Eqs. (3.7) and (3.9) give the formal solutions to be explored and compared with the formulas of MZI in the next section.

3.4 Tunable Loop Mirrors

In this section the theoretical responses between the SLR and the MZI will be compared, varying also their parameters. This allows to understand the strengths and weaknesses of the device and to propose a better implementation. Thanks to the development made of mathematical formulas with transmission matrices, any modification or change of parameters is quickly calculated using a mathematical program such as MATLAB [177]. Moreover, SLR 2x2 amplitude measurements compared to the MZI 2x2 will be shown. Finally, phase measurements of an SLR 2x2 compared to the simulation will be shown.

3.4.1 MZI vs Sagnac Loop Reflector

First, the schematics of the devices under study are shown in Fig. 3.6.

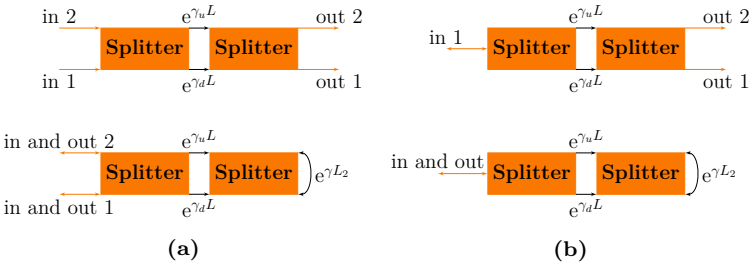

Figure 3.6: Schematics of (a) 2x2 MZI, 2x2 SLR and (b) 1x2 MZI, 1x2 SLRs.

Before analysing the response of both systems, it is necessary to make some considerations. First, a symmetrical Mach-Zehnder interferometer produces changes in the optical output through phase shift between arms. There are a many effects that can be employed in integrated optics to obtain a phase change as explained in the previous section.
On the one hand, acoustic, electro-optical and plasma-displacement effects require complex fabrication and materials to implement the actuators. On the other hand, the optical propagation constant can be changed with temperature by controlling the local temperature, increasing or decreasing a shift in the phase constant [173]. The heaters are the elements to produce these local variations and are typically

implemented by means of small electrical path on top of the waveguide. The dimensions (width and length) and the intrinsic sheet resistance (depending on the height and composition of the material) characterize the resistance of heater, which heats up according to the applied current flow. The disadvantages of using thermo-optical effect are:

- The speed of the modulation response, because it is a slow effect (milliseconds).
- The power consumption, which is too much for some applications.
- The stability of the system, because the use of local heat in a PIC could cause the heating of the full system producing non-desiderate response.
- The durability. Depending on the amount of power used in the heater, some effect such as electro-migration could cause the deterioration of heater.
- The environmental dependence. This effect depends slightly on the material surrounding the heater and its temperature, so any change in temperature conditions could affect the heater response.
- The stress-variations due to temperature increase. Due to the intrinsic properties of the materials, the temperature variations produce stress variations that lead to expansion and compression. If the PIC is not attached to the optical input, these mechanical variations could affect the chip alignment as shown in the next chapter.

However, most of the problems could be solved with: an adequate layerstack to have a better heater with high durability and low environmental dependence, air trenches around the waveguide to locate the temperature and reduce the thermal cross-talk across the chip. Therefore, this phase shifter is the best to use it in all technologies because no extra complex processes are required and it is the option chosen for this work.

Sagnac Loop Reflector could be modelled as two Mach-Zehnder connected as explained in the previous section. When choosing the thermal phase shifters, there is an important parameter called P_π, which is the electrical power needed to add a phase difference of π to an input optical signal in the system. In a SLR this P_π is half of the P_π of a single MZI due to the feed-back loop that forces to pass two times through the phase shifters. Furthermore, the Mach-Zehnders and the SLR are composed of three simple elements: waveguides, phase shifters and splitters.

As explained in the formalism, the waveguides propagation properties are determined by the propagation constant γ and it is composed of the attenuation constant α and phase constant β. The propagation losses of a specific geometry of waveguide depend on the material and the roughness of the waveguide sidewalls which can introduce large scattering losses. In addition, the length of the waveguide changes the total insertion loss of the waveguide section and the phase shift.

Finally, the splitters have two main parameters: excess losses σ and imbalance. The imbalance is the power distribution between the outputs of the splitter (K value). The excess losses parameter depends on the configuration of the splitter.

3.4.2 Simulations

Phase shifters tuning: control of Amplitude and Phase

Once all the terminology and the elements are clearly described, the power response can be analysed. In this sub-section, ideal conditions of splitters are considered: excess losses $\cong 0$, α L $\cong 0$ and K $\cong 0.5$. The phase difference between phase shifters changes the amplitude and phase of the SLR and MZI. Figure 3.7 shows

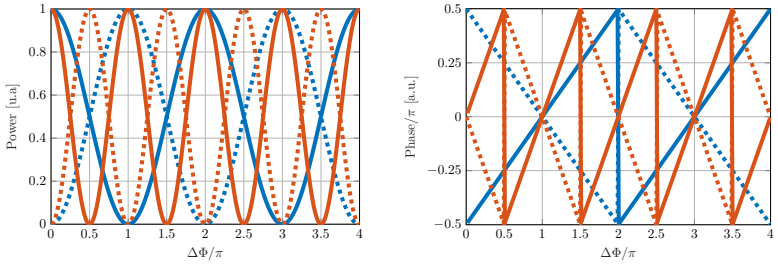

(a) Amplitude **(b)** Phase

Figure 3.7: Comparative figure between 2x2 MZI and SLR 2x2. Transmission of MZI in the cross-port (solid blue line), transmission of MZI in the direct-port (dots blue line), transmission of SLRs (solid red line), reflection of SLR (dots red line).

the improvement of Sagnac Loop Reflector regarding P_π as mentioned above. The x-axis shows the nominal phase change difference between phase shifters in number of π radians.
In an ideal and passive state of 2x2 MZI symmetrical, the formulas show that the main power is transmitted to the output port across from the input port. Tuning the phase shift difference between arms to π, the optical power is switched to the other optical output. In contrast, the 2x2 SLR with $\pi/2$ difference gets the same response and the optical power is at the same output port. Moreover, in π state the same initial power division is achieved.

In an ideal and passive state of symmetric 1x2 MZI, the formulas show that the main power is divided equally between the output ports with respect to the input port. Tuning the phase shift difference between the arms to $\pi/2$, the optical power is transmitted to an optical output. In contrast, the 1x2 SLR with 0 phase difference, ideally all the power is reflected to same input port and with $\pi/2$ it is totally lost.

Furthermore, if both arms are controlled, the phase could be controlled by changing both arms equally, applying a constant phase to the optical power. The

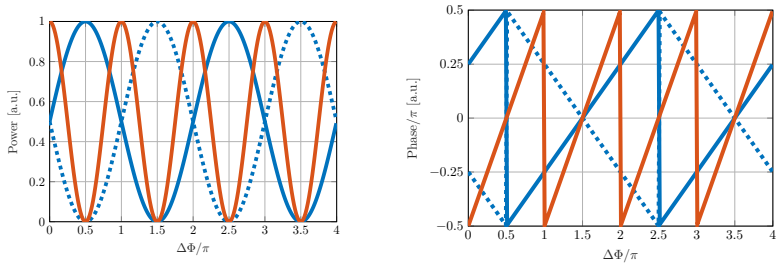

(a) Amplitude **(b)** Phase

Figure 3.8: Comparative figure between 1x2 MZI and SLR 1x2. Transmision of MZI in the cross-port (solid blue line), transmision of MZI in the direct-port (dots blue line), reflection of SLR (dots red line).

amplitude response depends on the phase difference between the arms and the phase response to the constant phase applied to both arms. As shown in Fig. 3.9,

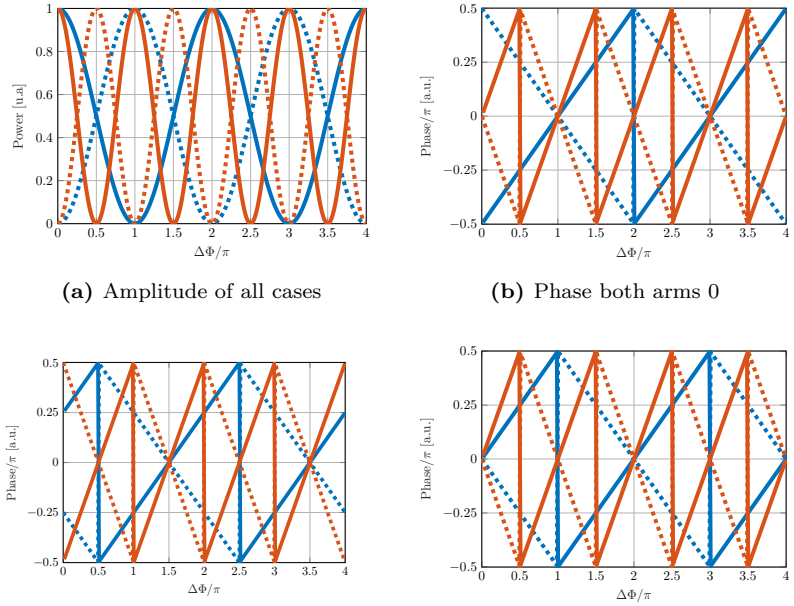

(a) Amplitude of all cases **(b)** Phase both arms 0

(c) Phase both arms $\pi/4$ **(d)** Phase both arms $\pi/2$

Figure 3.9: Comparative figure between 2x2 MZI and SLR 2x2 adding phase in both arms. Transmission of MZI in the cross-port (solid blue line), transmission of MZI in the direct-port (dots blue line), transmission of SLR (solid red line), reflection of SLR (dots red line).

the SLR 2x2 phase response could be tuned by applying the same phase to both

arms. Thus, if the phase could be controlled individually in each arm of AWG, it is possible to correct the phase errors in AWGs [20]. As shown in Fig. 3.10, the

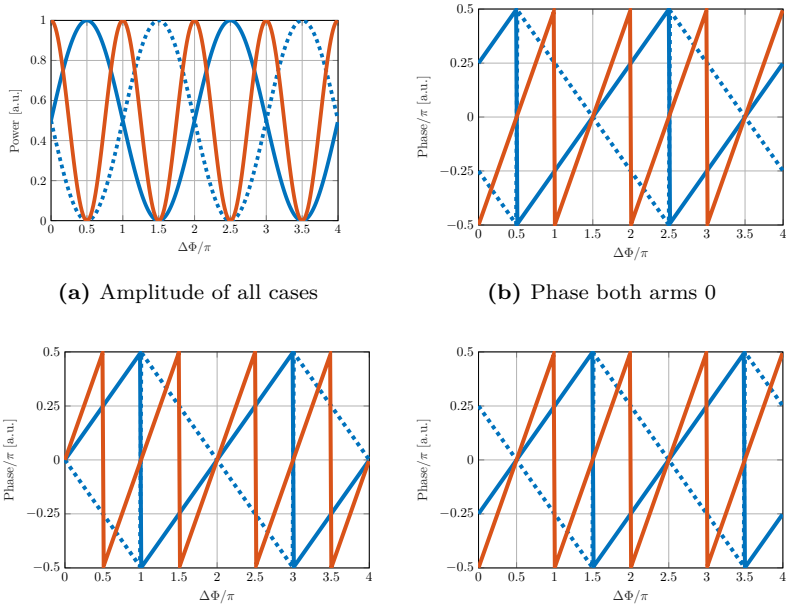

(a) Amplitude of all cases

(b) Phase both arms 0

(c) Phase both arms $\pi/4$

(d) Phase both arms $\pi/2$

Figure 3.10: Comparative figure between 1x2 MZI and SLR 1x2 adding phase in both arms. Transmission of MZI in the cross-port (solid blue line), transmision of MZI in the direct-port (dots blue line), reflection of SLR (solid red line).

1x2 SLR could reflect, without applying any phase shift difference, all the optical power with a controlled phase only by applying a constant phase shift on both arms.

Effect of excess loss and propagation losses

The propagation losses of the waveguides with the excess losses of the splitters impacts on the total output power. Only the amplitude is shown because the phase relation of the outputs doesn't change. As shown in Fig. 3.11 the propagation losses are not an important parameter in the MZI and in SLR response. The length of these devices is in the order of hundreds of microns and the propagation losses are in dB/cm, so the total losses introduced by this parameter will be low. However the difference in the excess losses produces great differences between MZI and SLR. As explained, the SLR is like two connected MZIs, so any change in the excess losses of splitters increases the losses differences between MZI and SLR. As shown in Figure 3.12 the behaviour is similar than in the 2x2 case.

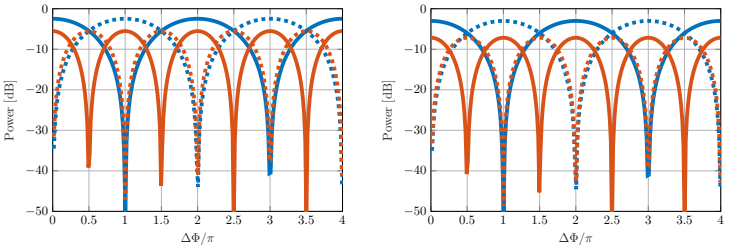

(a) 2dB excess loss and 3 dB/cm **(b)** 1dB excess loss and 6 dB/cm

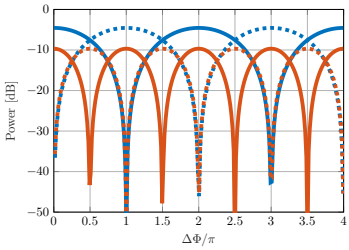

(c) 2dB excess loss and 3 dB/cm

Figure 3.11: Comparative figure between 2x2 MZI and SLR 2x2 changing excess loss and propagation losses. Transmission of MZI in the cross-port (solid blue line), transmission of MZI in the direct-port (dots blue line), transmission of SLR (solid red line), reflection of SLR (dots red line).

3.4.3 Measurements

The designs were fabricated in a MPW offered by CNM-VLC platform. The splitters were designed using the flow proposed in Section 2.2.2. The tests were carried out at the facilities of the research group [178] and the design, the setup and the procedure for the passives and active measurements of these devices are described in Appendix A.

To easily check the amplitude and phase response, the 2x2 SLR and MZI are measured and compared in transmission, so no complex setup using circulators is required. These measurements for 1x2 reflectors were inconclusive because the facets of the chip have strong reflections, and these shaded the pursued figure. The power dissipation of the heater is directly proportional to the phase shift applied to the waveguide [173]. As can be shown in Fig. 3.13, in the same power dissipation range as the MZI, the SLR transmission changes twice between the minimum optical transmission and the maximum optical transmission. This behaviour matches the theoretical estimations. On the other hand, as can be seen from the different levels of the maximum peaks, the thermal effect of misalignment greatly influenced the measurements. From the experiments, the physical misalignment is mainly in the z (vertical) direction. The stress resulting from fabrication of silicon nitride films at high temperature, makes them very sensitive to temperature changes, that

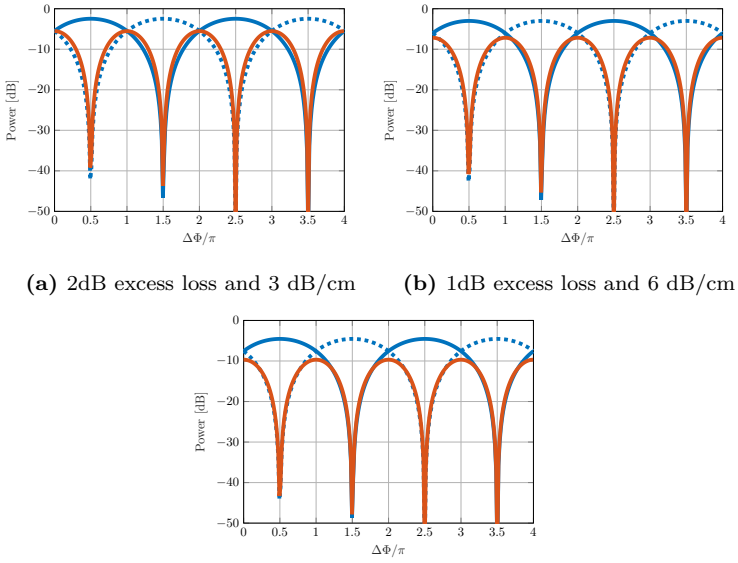

(a) 2dB excess loss and 3 dB/cm **(b)** 1dB excess loss and 6 dB/cm

(c) 2dB excess loss and 3 dB/cm

Figure 3.12: Comparative figure between 1x2 MZI and SLR 1x2 changing excess loss and propagation losses. Transmission of MZI in the cross-port (solid blue line), transmission of MZI in the direct-port (dots blue line), reflection of SLR (solid red line).

result into expansion or compression of the structure [179]–[185].

Finally, the theoretical model could be fed with the measurements of the splitters and the electrical response of the phase shifter. The electrical response of the phase shifter in terms of energy dissipation with the electrical current has a cubic relation [186], which means that the resistance is changing with temperature. Also, the theoretical model has been optimized until obtaining the values of amplitude and phase of the random noise to adjust to the response. The model perfectly predicts the amplitude response of the SLR for different cases.

The phase measurements were made using Optical Frequency Domain Reflectometry (OFDR) [187], [188]. Detecting the peaks of different temporal contribution due to the facets of the chip, the phase variation can be obtained. As shown in the right part of Fig. 3.14, the model can predict the amplitude response, however, there is some deviation in the phase response. If the phase response is analyzed, some fixed contribution is added as a function of the current applied. There is an extra optical length (less than 10 microns according to the calculations) which is heated in both arms of the SLR. The amplitude remains equal, but the phase response is higher than expected when the injected electrical power increases.

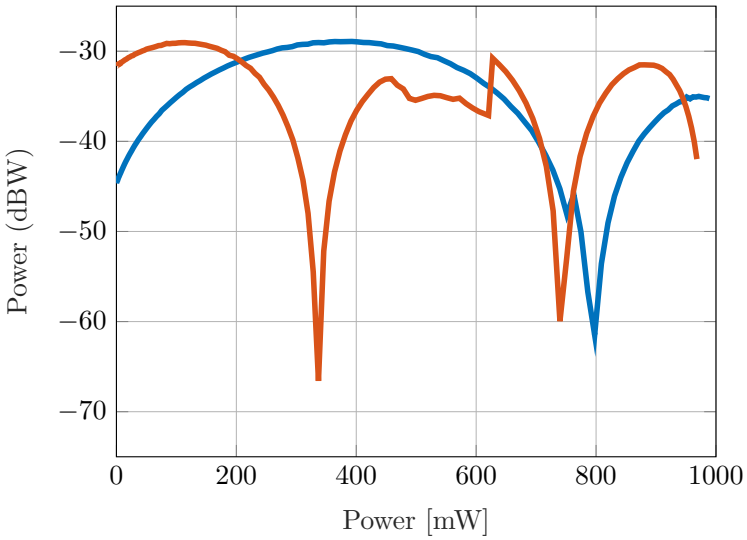

Figure 3.13: Example of power amplitude measurement MZI and SLR with 2x2 MMI varying the electrical power of one heater. MZI cross-port (blue) and transmission SLR(red).

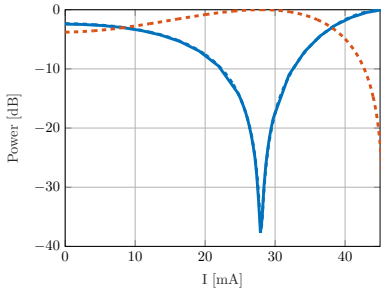

(a) Amplitude measurement(solid) vs simulated (dashed) response. Blue line shows the transmission and red line the theoretical reflection.

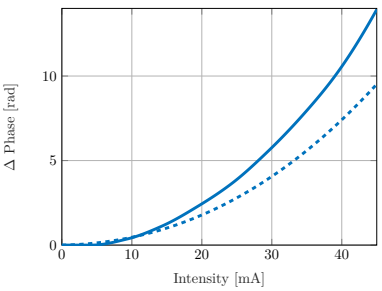

(b) Phase measurement (solid) vs simulated (dashed) response.

Figure 3.14: Amplitude and phase response of SLR and theoretical model predictions.

3.5 Conclusion and future

Different reconfigurable mirrors have been analysed with their advantages and disadvantages in order to use in the RAWG for reconfiguration. Due to the manufacturing characteristics of the CNM-VLC platform, the implementation chosen and studied is the use of mirrors with splitter and feedback loops. To analyse the response, a transmission matrix based code has been developed to compare the response between a MZI and its feedback version, the SLR. The simulations show

how the SLR achieves greater efficiency compared to the MZI, as the feedback allows the phase shifters to have greater efficiency. Finally, these structures have been measured both in amplitude and phase showing what was theoretically predicted. In fact, the theoretical model has been fed back with the measurements of the discrete elements and the noise values have been perfectly adjusted by fitting the measured amplitude response. With this model, the phase response has been analyzed appreciating a deviation of the measurement from the model. This deviation can be understood as an effective length greater than the implemented heater length that would make the two curves overlap perfectly. Furthermore, a mechanical optical misalignment with temperature has been detected showing that the fabrication is sensitive to local heating by modifying its stress state. This is an important issue for the RAWG due to the amount of heaters needed but in the next section will be explained the solutions that can be implemented.

Finally, as future work and as a basis for the RAWG in the next section, a better implementation of the SLR should be carried out especially to reduce its size with more compact curves and more efficient heaters. On the other hand, as can be seen in the simulations and measurements, the SLR 2x2 has passively all the power in the transmission port. This means that if these devices are placed in a RAWG, the optical alignment without applying any electrical power to the heaters will be almost impossible. The 1x2 SLR seems to be the best option for this, but the use of a 2x2 would limit its functions as it has less bandwidth than a 1x2. Therefore, the use of a 1x2 in each arm instead of the 2x2 splitter would improve its implementation, as well as its bandwidth, although it would increase its size by the use of two loops instead of one. This device, which we will call Tunable Reflective Michelson Loop (TRML) is the one we will use in the final design, and that thanks to the measurements made in this chapter, validates the theoretical model developed in this respect.

Chapter 4
Reconfigurable Reflective Arrayed waveguide gratings (R-RAWG)

Optical reconfiguration is a field with a growing interest in the world of integrated optics. Due to the characteristics of integrated circuits, it is possible to realise very complex or impossible circuits for fibre optics or free space optics. This is the case of transceivers, which are the current mainstream commercial products based on integrated optics for large companies such as Google, Facebook, etc., which allow a very complex circuit to be made in a very small device compared to its predecessors. Thanks to this success story that is driving the industry and whose market is growing exponentially, integrated optics is attracting attention for other applications where optics had been ruled out. Discrete optics made the implementation of certain commercial products difficult due to their sensitivity to temperature, vibrations, consumption, etc. The transition from optics to integrated optics is analogue to that from the electronics to microelectronics. Thanks to integration in the same substrate of the complete optical circuit, there is a drastic reduction in size, along with increased isolation, reduced power consumption and improved thermal management. Thus, thanks to integration, the reconfiguration of optical filters smaller than the fingertip is possible. The reconfiguration of optical filters opens up enormous possibilities that allow the wavelength response to be changed as desired and according to the application. As a result of this interest, the research group where this thesis has been carried out, has developed a patent [30] to implement a device called Reflective Arrayed Waveguide Grating (RAWG), which allows reconfiguration of the optical spectrum thanks to the amplitude and phase control of each arm in a RAWG. The purpose of this thesis was to experimentally demonstrate the feasibility of this device, since no similar device had ever been demonstrated (only a passive RAWG had been demonstrated). Therefore, after all the development and demonstration of the individual elements needed for the final device throughout this thesis, the aim of this chapter is to demonstrate a R-RAWG.

This chapter will review the literature of AWG and RAWG. Then, the RAWG simulator will be shown based on previous works combining it with the reflector simulator developed in this thesis. Later on, the new algorithm developed based on the multivariable global optimization algorithms will be explained, in order to optimize the value of each heater to achieve the desired response. It will be demonstrated how the algorithm will optimize the variables only with the wavelength response of the optical power in the simulation, achieving optimal solutions in different phase and amplitude noise scenarios in the waveguide array. On the other hand, all the problems and solutions that have been found to characterize this device will be shown, obtaining the optical power when acting on different thermo-optical actuators, forcing an in-house development to glue the chip to a PCB, making wirebondings, interconnection boards and a method to align a fiber array despite having a mechanical misalignment due to temperature. Despite all the problems found, it was finally possible to demonstrate the device thanks to the use of the algorithm demonstrated in the simulations. A dozen different high performance responses will be shown for the 1550 nm band in addition to the 1310 nm reconfiguration. Finally, conclusions will be drawn and future work will be drafted to improve this device with enormous possibilities. Some parts of following chapter were previously published in a peer-reviewed journal, and are reprinted here with permission [189].

4.1 Background and Motivation

Reconfigurable optical bandpass filters are key for optical signal processing and emerging applications such as Laser Imaging Detection and Ranging (LIDAR), bio-sensing, microwave processing and telecommunications [25]–[29]. Among other implementations, the AWG is the most-commonly used in the commercial application to implement integrated high performance photonic filters [190]. Since Smith described this device in depth and how to design it [20], the AWG has been studied and demonstrated for many applications and also, its traditional design has been improved to implement it in the smallest possible area, analyzing the design and some improvements to reduce manufacturing crosstalk and chromatic aberrations [76], [77], [191]. When an AWG is manufactured, due to manufacturing and light guiding, phase and amplitude errors occur that affect the final response of the AWG. On the one hand, to correct these errors, there are the techniques of trimming in production, to actively and permanently correct the manufacture once it has been made and thus reach the expected values [192]. On the other hand, there are the techniques of using active elements to adjust the response by controlling the amplitude and phase of each of the array waveguide [193]–[199].

To reduce the total area, the scheme of an AWG with mirrors, called RAWG has been proposed [150]–[153], [159]–[162], [165]–[168], [200]–[205]. This implementation reduces the total length of each arrayed waveguide to the half, making an improvement in terms of space and performance. As explained in the introduction of this chapter, the research group to which this thesis belongs has developed

a patent [30] to implement a R-RAWG. Although a design was theorised and attempted, a totally passive RAWG could only be demonstrated on a silicon photonics platform [169]. Therefore, the aim of this chapter is twofold, since it will be demonstrated for the first time as far as we know an R-RAWG and also on a silicon nitride platform, which, among other things, has enormous advantages in terms of its huge operating band as mentioned above.

4.2 DPASTOR algorithm (Descend the hill and Progressively AScend TOwards Reconfiguration)

4.2.1 Device description

The R-RAWG incorporates a tunable amplitude and phase mirror on each arm, as sketched in Fig. 4.1. As explained in the introduction, a static version device without tunable mirrors was previously reported [169]. In this work, no response optimization was provided and only the passive RAWG with Sagnac Loop reflectors was outlined, with some support simulations. The conceptual design of the R-RAWG incorporates a reflective version of a common MZI where each of the two arms is equipped with thermo-optic phase shifter (TOP) and terminated with a SLR, as described in Fig. 4.1b, called, as explained before, Tunable Reflective Michelson Loop (TRML). With this configuration, all MMIs are 1x2 which makes the overall mirror as broadband as possible with low losses. This dual-drive TRML could control amplitude and phase independently [206] as explained in the last section. Despite all TRML within an R-RAWG are made with the same layout, the fabrication deviations (height, width and material properties of the cross-section) leave all these mirrors at an unknown starting point in terms of phase and amplitude. Therefore, the passive response of the R-RAWG is distorted without correction. In the introduction, phase trimming techniques are introduced as a possibility, because they have traditionally been employed to telecommunications AWG (silica). However, the active capacity of tunable mirrors can, firstly, reasonably mitigate fabrication deviations and, secondly, obtain the spectral reconfiguration response.

Also, as explained in the last section, the phases shifters available on the fabrication platform used are low-loss TOPs. A well-known disadvantage of TOPs is the thermal chip control, which needs a ThermoElectric Cooler (TEC). Moreover, if several tens of them are used in reconfigurable PICs, the thermal cross-talk between them adds the complexity of stabilizing the thermo-optical response.

4.2.2 Reconfiguration strategy and implementation

As mentioned above, the R-RAWG initial response due to the fabrication deviations affecting each waveguide and TRML in the array is altered. For complex

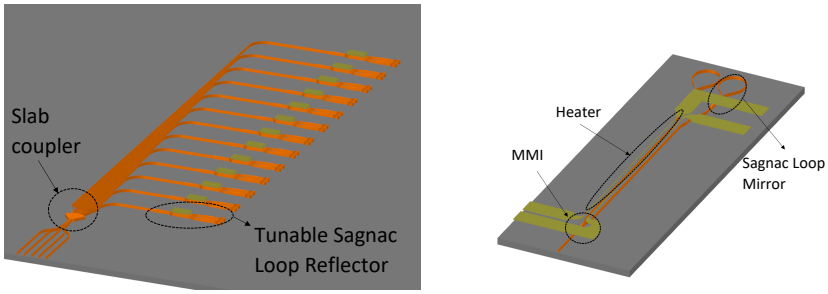

(a) Concept

(b) Tunable mirror

Figure 4.1: Conceptual sketches for the R-RAWG (a) and tunable mirrors (b). Device mask layout (c) and microscope photograph of the fabricated device (d) in a chip of 5x10 mm^2.

reconfigurable PICs, different methods are developed to optimize the optical response to reach a target. However, the R-RAWGs have an extra difficulty, since is an optical Finite Impulse Response (FIR) filter that makes it impossible to obtain the phase response of the amplitude with Kramers-Kronning relations and to characterize the amplitude and phase response, more complex techniques are needed with specific laboratory material to characterize it [207], [208]. Thus, mainly the options to achieve the reconfiguration of a R-RAWG are:

1. Techniques to obtain the full-field amplitude and the phase response of the system. Among others, the OFDR is one of the most used because full field response events can be recovered for a temporal range [187]. Although it's probably the most powerful and accurate technique, it needs heavy post-processing and precise configuration to recover the actual device response, which is difficult to make compatible with a real-time iterative measurement of the system response [193].

2. Gerchberg-Saxton algorithms to recover the phase response. These algorithms require an ideal amplitude assumption in the waveguide array to recover, with high level hologram retrieval algorithms, the phase response in each waveguide [194]. This option has been explored and some work has demonstrated the possibility of obtaining amplitude and phase, combining this algorithm with other algorithms such as Kalman filters, but their performance is limited and they are tested for image recovery [209].

3. Optimization algorithms with an objective function. This third approach, commonly called brute force [193], is based on the fact that the algorithms act simultaneously on all the variables on the basis of an objective function. Global optimisation algorithms are the basis for the so-called machine learning techniques such as deep learning, which ideally could instantly solve any problem if they are well structured for the problem and trained on solutions. There is a growing use of these techniques in applications as reconfigurable

OFDRs, even though they may not be as good as the OFDR techniques [193], [210], [211]. Addressing the complete problem (complete set of variables, final target response) in the R-RAWG seems almost impossible due to convergence. The reason is that iterative and continuous measurements are required, with an inherent non-linear response that evolves over time due to the cross talk of the thermal phase shifter.

Due to the impossibility of using techniques to characterise the amplitude and phase of a time spectrum in real time and the lack of homogeneity of the amplitude because the mirrors do not reflect the same after manufacturing, the third option was chosen. Nowadays, machine learning algorithms are used in many scenarios such as voice recognition, strategy marketing, computer vision, topology optimization, etc. in which optimum solutions are sought even if there is no exact solution, with a model that is trained (optimizing its large number of variables) according to the problem, giving the algorithm the solution and the inputs to the problem [51], [212], [213].

As a first step to develop a deep learning or some high level machine learning algorithm trained for the problem, a method using Global Multivariable Optimization (GMO) algorithms borrowed from machine leaning is needed to obtain a solution to our problem. There are many GMO algorithms, however, thanks to the in-depth knowledge of the OFDR operation and characteristics, some stand out over others. The response of an OFDR when power is introduced in an input and power is obtained in an output depends on the constructive interference radiated by the array guides. The slab coupler on both sides is analysed as a Fourier spatial transformation [214]. Thus, due to its arrangement in an array, the central waveguide receives more power than the rest, dividing the amplitude of the input into a Gaussian distribution in the rest of the waveguides. In addition, another aspect of our problem is that due to the optical misalignment already detected with a pair of actuators in the previous section, an algorithm is required that can be paused and restarted from a certain point of the optimization. Also due to the thermal cross-talk, this algorithm has to optimize even if the variables vary their influence on the solution with time and value. Thus, within GMO algorithms, algorithms that use statistical analysis of how the solution varies with respect to the variables such as neural networks can be discarded, because they need many evaluations and stability of the problem to find an optimal solution. Algorithms that use the function derivative to iterate can also be discarded, because they may fall to a local minima or require multiple random initialization searches to find a global solution. Therefore, among all the algorithms, the derivative-free GMO algorithms seem to be the most suitable. These have already been successfully used for variable optimisation in nano-photonics [210], but within this group, there is one that has been developed relatively recently and that obtains optimal solutions with a low number of iterations, called pattern search algorithm [215], which is the one that will be used in this work.

4.2.3 Numerical validation

A R-RAWG numerical model was implemented using integral Fresnel for the star coupler and effective indices and length of each section, as in our previous works [169], [214]. This model includes the response of the mirrors with the theory described above including the response in the measurements of heater behaviour. This heater has a cubic relationship between the power consumption and the electric current due to the self-heating [186]. Also the numerical model implements phase and amplitude noise [216] along all the arms of the R-RAWG, to synthesize a similar response to reality after manufacturing.

Therefore, the possible simulation responses of the R-RAWG were reproduced by simulation with the same parameters of the manufactured device that can be seen in the following section. As a first approximation to optimize the values of each heater in each arm, all the variables were tested at the same time, defining the cost function similar to that used in the synthesis of microwave filters. It consists of the sum of the absolute value squared of the difference between the target response and the device response in logarithmic units [217]. This cost function behaves in a very similar way to sigmoid activation which, as reported in machine learning algorithms, improves convergence in all possible scenarios [218], [219]. In spite of this, an attempt was made to optimise all the variables at the same time with various configurations, but it was not possible to achieve optimum solutions and in addition, the number of iterations to reach this solution was very considerable.

Therefore, an attempt was made to develop an alternative method to achieve optimisation. Due to the knowledge of the structure and the experience in the characterisation, a method or algorithm based on this knowledge was developed to achieve the optimisation of the response. The first step is to optimise the heaters to minimise the optical power over all wavelengths, i.e. what is attempted in this step is to turn off all the R-RAWG arms. In this step any GMO algorithm is optimal since power minimization, that it is the cost function, is simple in terms of R-RAWG response. This is because, as can be observed in the section on tunable mirrors, with the control of a single heater per mirror it is possible to minimise the amplitude of reflection, making the solution quick to achieve in few iterations. Once the value of the variables that manage to minimise the power output is obtained, the values of the heaters are progressively optimized, starting with those of the central arm and one close to it (pursuing their importance in the final solution as the star coupler distributes more power in the central arms). This in the pattern search algorithm is possible because it is based on providing a starting point, which are the minimization values, and optimize only some values depending on the target function. In this case the cost function is defined as described above but the target function would be the one that ideally would be obtained if only those arms of the R-RAWG are tried to optimize, which would be the response of an MZI. Thus, the algorithm only optimizes four TOP values. Once found some values that converge for this step, the objective function is replaced by the one that ideally would be obtained with the three central arms of the R-RAWG, a three-armed MZI, and from the values of the variables of the previous

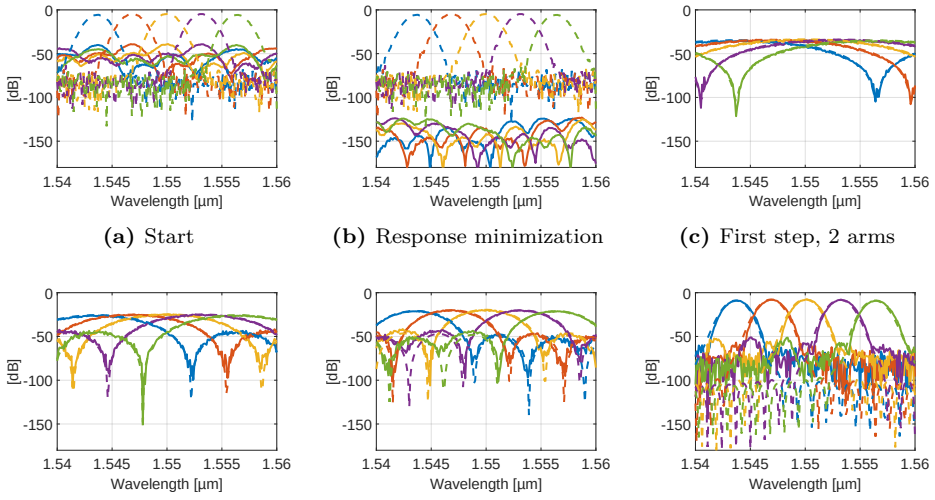

(a) Start **(b)** Response minimization **(c)** First step, 2 arms

(d) Second step, 3 arms **(e)** Third step, 5 arms **(f)** Final step, 19 arms

Figure 4.2: Step-by-step optimisation using R-RAWG response simulation. The sub-figures show in solid and dashed lines the actual and target normalized responses (in logarithmic units) at a given step versus wavelength. Each of the coloured lines within the graphs represents one of the five outputs of the R-RAWG channels. In (a) there is the starting situation, in which the real response is forced to differ heavily from the target one, because it includes amplitude and phase errors. Panel (b) presents the first step in which the tuners are configured to minimize the response. From panels (c) to (e) the optimization step is shown for each increase in the number of arms and variables. The last panel (f) shows the final response for 19 arms optimized.

step, the algorithm optimizes the six values of the TOPs. In this way, the number of arms will be increased depending on the amplitude that they have due to the distribution of the array until all the values are optimized. The procedure followed and its partial solutions can be seen in Fig. 4.2. The first sub-figure presents the target response for all the R-RAWG channels in dashed lines (without random noise), while a simulated real response including random noise for the same is given in solid lines. In sub-figure (b) shows the result of minimizing the simulated real response. This provides a set of TOPs currents for the next step, restoring the response. From this set, the target and current function is shown in sub-figure (c) after optimization for two arms (4 TOPs), and following the optimization steps for 6 and 10 TOPs (3 and 5 arms enabled respectively) in (d) and (e). Finally, Fig. 4.2-(f) provides the result of the optimisation against the target response when all the 38 TOPs (19 arms) are activated and optimized.

As can be appreciated in Fig. 4.2, a really nice solution was obtained with this procedure. The algorithm has different stop criteria to end the optimization and with the example showed in the figure, the minimization step took 2768 iterations,

and for all the other points of the response restoring step another 11283 iterations. Different conditions of random noise scenarios were simulated and optimized and, on average, the minimization could be carried out in 3000 iterations and response restoring in about 12000 iterations. These results are from simulations and the stop criteria are not optimized to reduce the number of iterations because this thesis was not intended to be a fast but accurate method. The R-RAWG response simulation code is not completely optimized and for each iteration 11 seconds were needed to simulate, because the computation time of the pattern search is negligible. However, in the experiments reported below, the analyzer span and resolution can be adjusted to minimize the spectrum acquisition time, leading to optimization steps of 2-3 seconds in total. Although the simulation time and the number of iterations needed by this method to optimize 38 variables with this complex problem could be reduced, it should be taken into account that if a precision of 1 mA is chosen in the 75 mA range in which each heater (each variable) can vary, the number of possible combinations would be of the order 10^{118}.

For a better description of the flow of the algorithm and the particular values and iterations, see the supplementary information below Appendix B.

4.3 Materials, methods and results

The R-RAWG was designed and fabricated in the CNM-VLC silicon nitride platform explained in the introduction [34], [37], [40]. The silicon nitride platform was chosen instead of silicon photonics because it can potentially operate from visible to mid-infrared [37] covering a multitude of needs for various applications, which is why reprogrammable devices are so interesting. The cross-section chosen

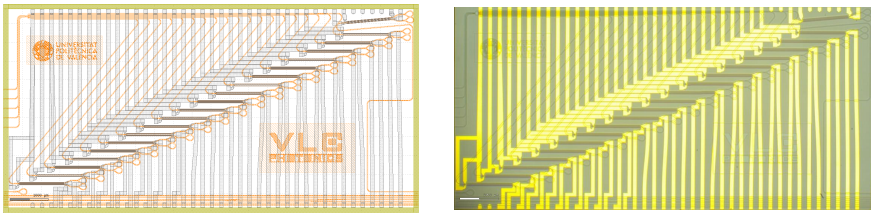

(a) Layout **(b)** Fabricated chip

Figure 4.3: Device mask layout (a) and microscope photograph of the fabricated device (b) in a chip of 5x10 mm^2.

for the waveguide routing and inside the AWG was the deep waveguide of 1 µm. According also with previous works in the platform [173], the TOP width chosen is 5 µm of 1.2 mm length. The R-RAWG parameters of the devices designed are: center wavelength 1550 nm, 5 channels with spacing 3.2 nm and FSR of 25.5 nm, slab coupler length 74.88 µm, arm length increment 49.24 µm and the number of arms is 19, with bend radius 100 µm. The waveguides interfacing the slab

coupler are up/down-tapered to 2 µm. They are placed following a traditional constant angle layout, 3 µm spacing over the grating circle. The R-RAWG footprint is 10x4.5 mm^2 (width x height) using and orthogonal layout as can be seen in Fig. 4.3 with the device layout and the fabrication. The mirrors placed in the design follow the TRML design described at the end of the previous section and it has large footprint due to the large bending radius (conditions the arm spacing) and lengthy heaters (so as to make them reliable for a given width). This implementations tries to increase the functionality of the mirror using 1x2 splitters that have very large bandwidth and low loss. At the outer part of each interferometer arm or heater, a shallow trench (just the cladding oxide removed) of 5 µm width is placed at distance of 13 µm. An additional trench is also present in the space between the two arms / heaters at 10 µm distance. With optimized TOPS cross-sections [220], or other tuning mechanisms, the footprint of the R-RAWG could be significantly reduced. The metal routing was optimized to have the large resistance in the heater length so the metal until the heater doesn't affect to the total resistance so the resistance variability is less than 3 %. The optical inputs are spaced to characterize with a fiber array of 250 µm pitch and the pads are also compatible to do wire-bonding with a pitch of 250 µm pitch.

4.3.1 Characterization setup: problems and solutions

The chip is mounted on top of a PCB, and the TOPs pads are wire-bonded to the metal lines in the board, as shown in Fig. 4.4. Due to the number of waveguides in the array (19), there are 38 heaters that need individual control. In this design, it translates to 68 electrical contacts because some are common grounded. The first test that was made with standard fibers was limited by the number of electrical sources presented in the laboratory. Also, due to the impossibility to control by computer, manual iteration of the currents was made only for few reflectometers. The solution was not optimal but this was the first test and some restoring solution could be obtained controlling some central arm heaters. Also, thanks to this first test, high coupling losses were measured due to the use of SMF28 fiber of MFD of 10.4 µm that limited the range of the optical detection necessary to do the minimization procedure. Another issue that was detected is that when performing the electro-optical characterization of the devices the optical alignment can be modified by the thermal mechanical stress of the materials. It was observed two main sources for this misalignment:

1. The PIC itself, due to the different stack of the materials, could be bent due to the different material thermal expansion coefficients.

2. The supporting elements. The PCB and the different materials below (for example metal carrier) could be modified by a small temperature gradient. The TEC that is typically placed below the chip, could be expanded due to the temperature changes.

The initial setup employed is shown in Fig. 4.5. A complex cabling layout and an

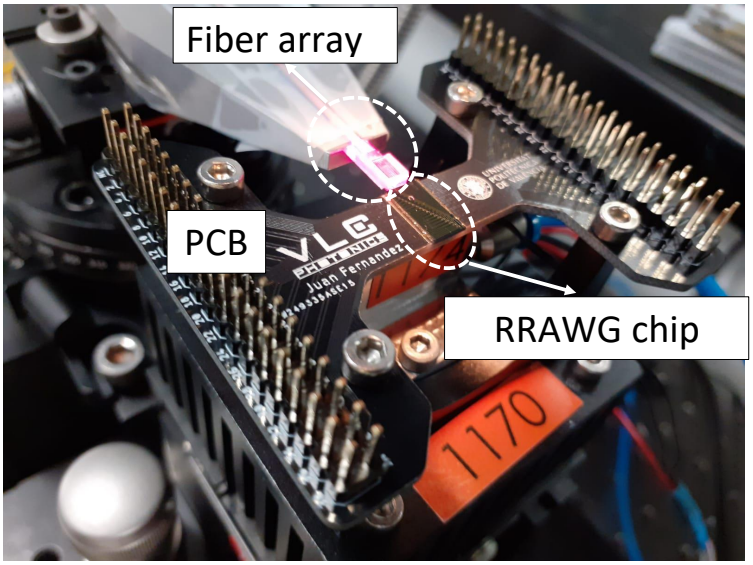

Figure 4.4: Chip, PCB and fiber array.

electrical interconnection box was required. This box was designed and assembled specifically for this project.

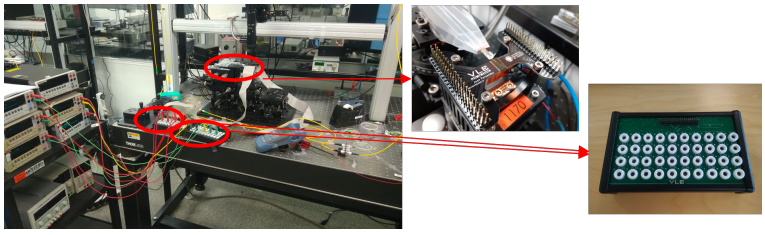

Figure 4.5: First version of the setup.

Once all the problems were detected, different solutions were carried out to improve the measurements. First, four multi-current sources, each one with ten channels, were acquired from Luzwavelabs. This has allowed us to reduce significantly the electrical testing equipment footprint [221]. The controlling of these current sources was based on python language and code was developed to control and to implement a communication between the MATLAB simulation and optimization code and the python libraries to control the devices. Also, a custom PCB design with SAMTEC connectors was designed to integrate all the cables that introduced additional resistance in the electrical paths and produce error connections in the same substrate, as can be seen at the right side of Fig. 4.6.

Second, multiple UHNA7 fiber array [222] were acquired, reducing the insertion losses because they have a 3.2 µm MFD at 1550 nm.

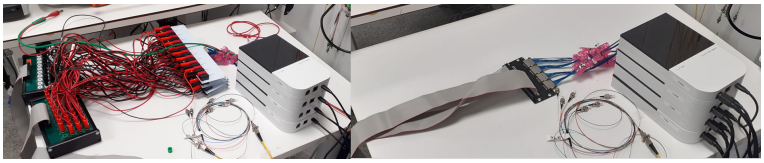

Figure 4.6: Luzwavelabs multicurrent connection before and after the connection integration.

Third, to mitigate the misalignment due to the temperature, two solutions were found. On the one hand, and the easiest one was to glue the fiber array to the chip. VLC Photonics has the capabilities to attach fiber arrays with certain specifications. However, due to the use of UHNA7 with only passive alignment, it was impossible to align when the measurements were done. Nowadays, the expertise is higher and this alignment was tested and satisfactorily proven (as can be shown in the Figure 4.7. On the other hand, a basic method was developed to have a fiber array aligned despite the optical misalignment. The idea of this was that once the fiber array was totally aligned almost perfectly parallel to the chip, push the fiber array against the chip facet. With this force applied to the fiber array thanks to the micro-positioner, the fiber array is moved in the same direction as the chip facet is displaced by to the expansion and compression, due to the friction force between both facets. This method was used for the characterization measurements.

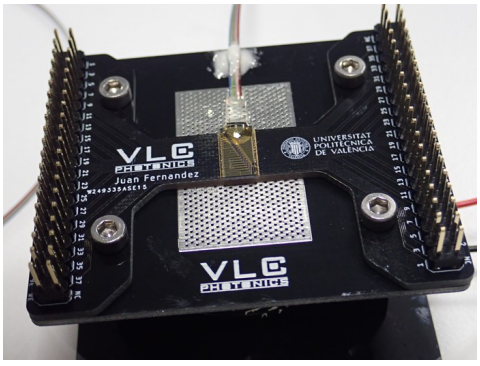

Figure 4.7: Glued chip to fiber array.

Once all the elements and the developments were carefully explained, the final setup and the methodology to get the measurements are going to be explained. The characterization setup consists of two stages, one with the micro-positioners, a three axis motorized positioner and a manual positioner to control the yaw rotation

angle, Fig. 4.8. The PCB with the chip sits on top of a thermally controlled chuck, held by the second stage. For the measurements, the fiber array is aligned manually in three steps.

First, the fiber array is yaw rotated until the fiber array edge is parallel to the chip. The other pitch and roll rotation angles do not need to be adjusted because the sample and the fiber array are carefully placed to be as parallel as possible. Second, a red light is used in two of the fibers in the array for visual alignment purposes. Third, once the fiber array is visually aligned with red light with the three-axis movement of the fiber array, a broadband infra-red light source (BBS) is connected to one of the fibers, whereas a power meter is connected at the other fiber of array. Hence, the position of the fiber array is optimized with the motorized stages to obtain the maximum power.

When the fiber array alignment is optimized, the power meter is replaced by an OSA, which is used to record the spectra with a resolution of 20 pm for measurements in the optical C-band. To characterize in the O-band, the same procedure is used but the BBS is replaced by a Yenista tunable laser with a CT400 combiner, employed to synchronize the sweep and spectra recording. The spectra are recorded after each step where the TOPS are tuned to the currents provided by the pattern search algorithm. The OSAs currents are generated with a four multi-current LuzWavelabs modules, with ten current sources each, Figure 4.8.

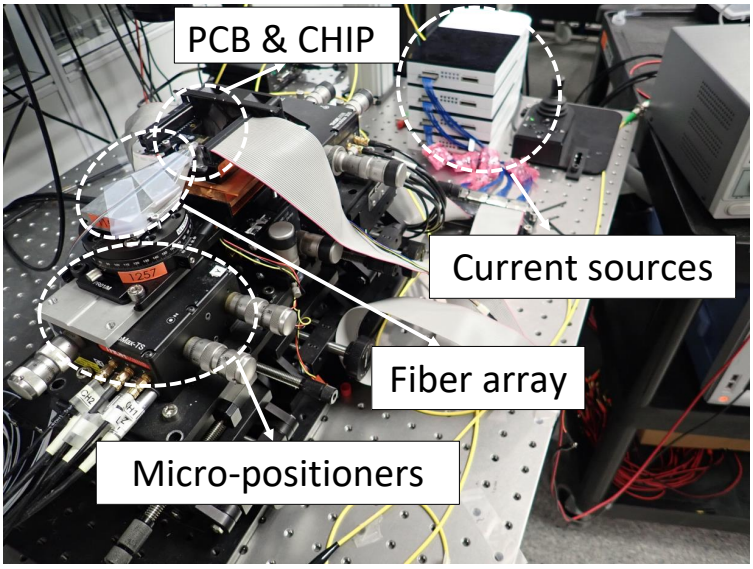

Figure 4.8: Setup general view.

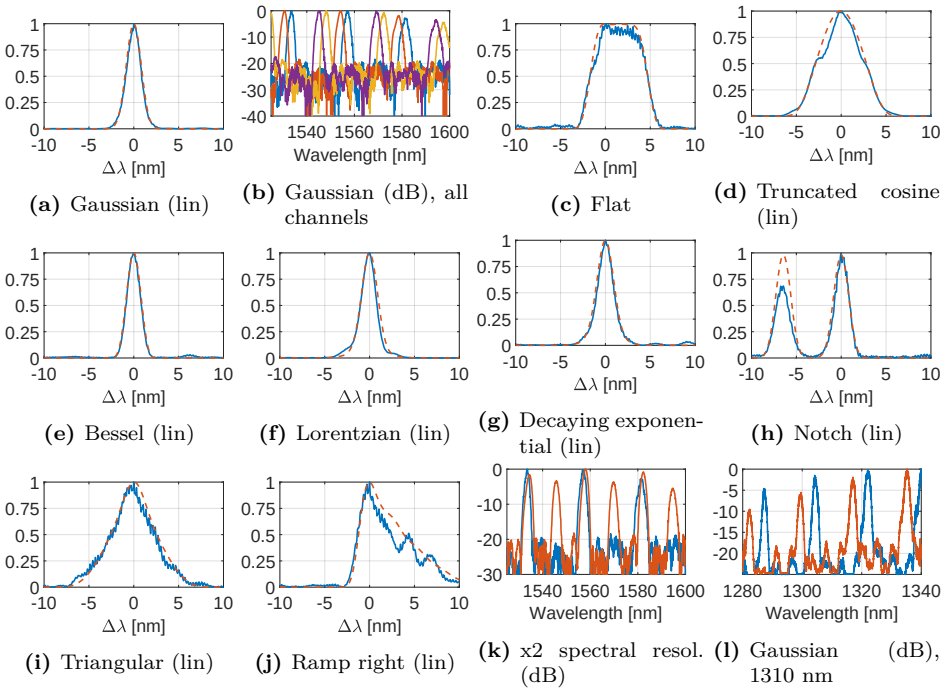

(a) Gaussian (lin) **(b)** Gaussian (dB), all channels **(c)** Flat **(d)** Truncated cosine (lin)

(e) Bessel (lin) **(f)** Lorentzian (lin) **(g)** Decaying exponential (lin) **(h)** Notch (lin)

(i) Triangular (lin) **(j)** Ramp right (lin) **(k)** x2 spectral resol. (dB) **(l)** Gaussian (dB), 1310 nm

Figure 4.9: Spectral response reconfiguration results. All the responses are given normalized, either in linear (lin) or logarithmic (dB) units. For the linear representations, the horizontal axis is given as wavelength difference in nm from the peak center.

4.3.2 Characterization results

To evaluate the insertion loss of the R-RAWG, the transmission spectra of straight waveguides is captured. Even though the insertion loss can thus be de-coupled, the straight waveguide transmission to that of the setup without chip is compared. A 3-3.5 dB/facet and 5-5.5 dB/facet insertion loss are obtained, for microscope objectives with 2.5x2.5 µm² MFD and for ultra-high numerical aperture (UHNA7) fiber with 3.2x3.2 µm² MFD, respectively. The results are compatible with the MFD of the in/out waveguides 1.19x0.95 µm².

The maximum insertion loss for the Gaussian optimized device was 15 dB below the transmission of the straight waveguide. From those, 5 dB corresponds to a propagation loss of 2.5 cm and 2 dB to excess losses of the splitters used in the Michelson interferometer. Thus, the insertion loss of the R-RAWG is less than 8 dB considering that part of it may be due to the fact that the fiber array is not optimally aligned.

Some results of the reconfiguration of the spectral response are given in Fig. 4.9, further detailed responses can be explored in linear and logarithmic scales in Appendix C. The algorithm flow, and the particular values and iterations required,

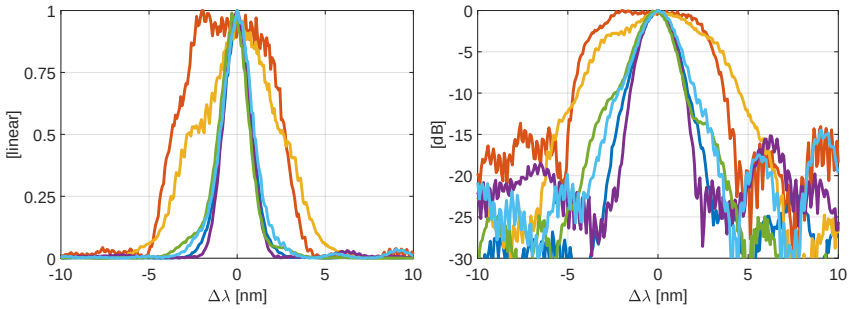

(a) Linear **(b)** Logarithmic

Figure 4.10: Spectral response reconfiguration results compared. All the responses are given normalized, in linear (a) and logarithmic (dB) units versus the wavelength difference in nm from the peak center. The colors correspond to Gaussian (dark blue), flat (red), truncated cosine (orange), Bessel (purple), Lorentzian (green) and decaying exponential (light blue).

are detailed further in the supplementary information. Twelve different responses where synthesized. Except in (b), (k) and (l), only one FSR is shown for clarity, when comparing the synthesized responses with the target. In this case linear units are used to clearly appreciate the differences. In the figure, a regular Gaussian response is first shown on panel (a), alongside with the same response for the rest of the AWG channels in panel (b). From (c) to (g) the experimental results for the synthesis of flat, truncated cosine, Bessel, Lorentzian and decaying exponential responses are shown, all of them compared with their target function. Note that the starting point for all this is the previously optimized Gaussian response. All these experimental plots are collated in linear and logarithmic units in Fig. 4.10 (cf. with the theoretical proposal in Fig. 6 of our early work on reference [169]).

Other functions are synthesized in Fig. 4.9-(h) to (j). In (h), the band-pass is unfolded to create a notch filter, whereas in (i) and (j) triangular shaped functions, isosceles and right triangle (ramp) are shown. A version of right triangle with opposite ramp was also demonstrated, but not shown for the sake of space. Panel (k) shows a Gaussian response synthesized with half FSR. Theoretically that would correspond to having two interleaved sub-arrays out of phase, as described in [223]. In conclusion, and from an application perspective, besides changing the shape of the bands, the R-RAWG can reconfigure their spectral resolution. Furthermore, and due to the broadband nature of silicon nitride on silica platform and the tunable mirrors used, the responses were also synthesized for the O-band, with two channels shown in panel (l). In this case, the other channels could not be measured correctly, the alignment was critical owing to a cross-section designed to work in the C-band, and light was guided through the substrate mainly, obfuscating the passing bands up to some extent.

As a general conclusion, looking for example at e.g. Fig. 4.10-(b), the shape of the bands can be adequately approximated, but indeed the overall response (band

and out of band) is not yet optimal. There are several factors to investigate for further improvement, two of which stand out. Firstly, the ability of algorithm to find the best combination and how good it is. In this paper a pattern search is used as a tool for a proof-of-concept, but leave unexplored how to assess on the machine learning algorithm performance itself. Secondly, design improvements to alleviate distortions (amplitude and phase) are not into place. These, indeed, would help the algorithm and overall strategy, progressively establishing objective responses from simple MZI to generalised MZI, enabling the arms to be used step by step. The better the design, the better the match in the progressive steps and hence the final result. These design improvements should include waveguide widening in straight sections [224]–[226] and improved grating line waveguide placement in the slab coupler interface [76]. Last but not least, better thermal isolation (i.e. with deep trenches down to the silicon wafer) would certainly alleviate the optimization efforts.

4.4 Conclusions and future work

In this chapter, the design, fabrication and experimental validation of an integrated reconfigurable reflective arrayed waveguide grating in silicon nitride technology has been presented. The reconfiguration was approached using optimization algorithms borrowed from machine learning and adapted to the internal structure of our device. A dozen of different band-pass shapes have been demonstrated, alongside spectral resolution change in the C-band and operation in O-band. The device could be improved both in footprint, through the use of more compact bends and tuning elements, and performance, through the refining of the internal structure, waveguides and slab couplers, as well as through the design of auxiliary elements, such as edge and MMI couplers, to operate broadband.

Chapter 5
Thesis conclusions and outlook

5.1 Conclusions

The objectives of this thesis have been met with the following conclusions:

- With the silicon nitride platform available for this thesis, the basic structures required have been analysed and improved. Using the manufacturing processes already defined, a low-loss coupling structure to the chip was proposed and characterized, analyzing its possible variations due to the technology, and showing its robustness to manufacturing variations and the high performance. On the other hand, an improved design flow for the MMI was developed and applied in this technology. These devices tested to have better performance and to be more robust to manufacturing than those already designed on the platform, demonstrating the validity of the method.

- The possible implementations of a reconfigurable reflector on the platform were analysed, and the use of tunable loop mirrors with different configurations were proposed, analysed and characterised in chapter 3. Due to their easy implementation and the use of existing processes on the platform, these mirrors, which are composed of splitters, waveguides and TOPs, were chosen. An analytical model was developed to predict the amplitude and phase behaviour. In addition, measurements of the discrete elements can be fed to the model predicting the experimental measurements in phase and amplitude performed.

- For the first time an R-RAWG was tested showing a great performance and configurability that serves to multitude of applications, which is what is shown in chapter 4 of this thesis. For the characterisation, we resorted to achieve developed methods and solutions for the characterisation, electrical control and optimisation of up to 38 actuators while obtaining the optical response. A theoretical model was developed that incorporated the responses

of the mirrors and the variations by manufacturing. Thanks to this model, a strategy was developed using global multivariable optimization algorithms used in machine learning, which allowed optimizing the variables to achieve a certain objective response even though only the optical power response was used. This device was developed on a silicon nitride platform and as demonstrated, in the O and C bands, thus proving its viability as a reconfigurable spectrometer of very wide bandwidth.

5.2 Outlook

After all the work carried out in this thesis there are some future paths that could be explored:

- Optimisation can be carried out in all aspects of RAWG design that might greatly reduce its size, decrease its losses and reduce its variability. Among others: using an SSC that would allow low losses for fibre coupling, more compact heaters, tighter curves with Euler bends for example, splitters with better losses, a better design of the distribution of the waveguides in the array, etc. If it is also possible to use metallised reflection layers at waveguides level and no bends would be required, the design could be even more compact.

- The development of the deep learning based DPASTOR algorithm, as a feedback deep learning scheme for this device. Thanks to the fact that it can be fed with different cases and solutions, this artificial intelligence would immediately allow to have a solution based on the objective function that is sought with only the initial passive response from the R-RAWG.

- Develop this device in other silicon nitride platforms and different materials. In addition, the design is compatible with different platforms that can be explored such as SOI, InP and Planar Lightwave Circuit (PLC).

- Make a packaged device. The main use of this device is for spectrometry in various bands such as Mid-Infrarred where gas sensing is located. Thus, with a packaged and functional device different experiments or application tests could be done.

5.3 List of Publications

Journal papers

1. J. Fernández, J. Felip, B. Gargallo, J.D. Domenech, D. Pastor, C. Domínguez and P. Muñoz, "Reconfigurable reflective arrayed waveguide grating using optimization algorithms", *Optics Express*, 28(21), 31446-31456, 2020.

2. P. Muñoz, P. W. van Dijk, D. Geuzebroek, M. Geiselmann, C. Dominguez, A. Stassen, J.D. Doménech, M. Zervas, A. Leinse, C.G.H. Roeloffzen, B. Gargallo, R. Baños, J. Fernández, G. Micó, L.A. Bru and D. Pastor, "Foundry developments toward silicon nitride photonics from visible to the mid-infrared", *IEEE Journal of Selected Topics in Quantum Electronics*, 25(5), 1-13, 2019.

3. J. Fernández, R. Baños, D. Domenech, C. Domínguez and P. Muñoz, "Low-loss inverted taper edge coupler in silicon nitride", *IET Optoelectronics*, 13(2), 62-66, 2018.

4. P. Muñoz, G. Micó, L.A. Bru, D. Pastor, D. Pérez, J.D. Doménech, J. Fernández, R. Baños, B. Gargallo, R. Alemany, A.M. Sánchez, J.M. Cirera, R. Mas and C. Domínguez, "Silicon nitride photonic integration platforms for visible, near-infrared and mid-infrared applications", *Sensors*, 17(9), 2088, 2017.

Conferences contributions

1. J. Fernández, L.A Bru, D. Pastor, D. Doménech, C. Domínguez and P. Muñoz, "Reconfigurable reflective arrayed waveguide grating (RAWG)" in *Proc. 2021 SPIE Photonics West OPTO*, 11689-13, San Francisco, California, United States, 2021.

2. J. Fernández, L.A Bru, D. Pastor, D. Doménech, C. Domínguez and P. Muñoz, "Sagnac Reflector Based Broadband Tunable Integrated Mirror" in *Proc. 2020 22nd International Conference on Transparent Optical Networks (ICTON)*, 1-5, Bari, Italy, 2020.

3. J. Fernández, L.A Bru, D. Pastor, D. Doménech, C. Domínguez and P. Muñoz, "Statistical analysis of passive components manufactured in a thick silicon nitride platform" in *Proc. 2020 22nd European Conference on Integrated Optics*, Paris, France, 2020.

4. J. Fernández, L.A Bru, D. Pastor, D. Doménech, C. Domínguez and P. Muñoz, "Universal tunable integrated mirror: the Sagnac Loop Interferometer" in *Proc. XI Spanish Optoelectronics Meeting (OPTOEL) 2019*, Zaragoza, Spain, 2019.

5. G. Micó, L.A Bru, D. Pastor, D. Doménech, J. Fernández, A. Sánchez, J.M. Cirera, C. Domínguez and P. Muñoz, "Silicon nitride photonics: from visible to mid-infrared wavelengths" in *Proc. Silicon Photonics XIII*, 10537, 105370B, San Francisco, California, United States, 2018.

6. J. Fernández, M.A.G Porcel, H. Jans, D. Geuzebroek, S. Mas, P. Leisching and J. Witzens, "Silicon Nitride Photonic Integrated Circuits for Biophotonics and medica applications" in *Proc. NanoBio&Med 2018*, Barcelona, Spain, 2018.

7. J. Fernández, R. Baños, D. Doménech, C. Domínguez and P. Muñoz, "Low-loss inverted taper edge coupler in silicon nitride" in *Proc. 2018 20th European Conference on Integrated Optics*, Th.2.B.2-110, Valencia, Spain, 2018.

8. D. Pérez, J. Fernández, R. Baños, J.D. Doménech, A.M. Sánchez, J.M. Cirera, R. Mas, J. Sánchez, S. Duran, E. Pardo, C. Domínguez, D. Pastor, J. Capmany and P. Muñoz, "Switching and cross-talk characteristics of compact thermal tuners on a silicon nitride platform" in *Proc. 2016 18th European Conference on Integrated Optics*, p-02, Warsaw, Poland, 2016.

Other contributions

1. D. Pérez, J. Fernández, R. Baños, J.D. Doménech, A.M. Sánchez, J.M. Cirera, R. Mas, J. Sánchez, S. Duran, E. Pardo, C. Domínguez, D. Pastor, J. Capmany and P. Muñoz, "Thermal tuners on a Silicon Nitride platform", *arXiv preprint*, arXiv:1604.02958, 2016.

Appendices

Appendix A
Die of test structures and setup characterization

A.1 Design

To test every individual element as splitters, waveguides and diverse configurations of SLRs, the designs were fabricated in a MPW offered by CNM-VLC [40] within a 5x5 mm^2 chip die. In this die were included designs in deep cross-section and in shallow cross-section. The most interesting is the deep cross-section devices due to the monomode behaviour. Two versions of deep MMI were designed for two inputs and two outputs. Widths of 8.4 µm and for 11.4 µm of the multimode waveguide were chosen. The narrower width is to corroborate the estimations that the coupling between arms can't be avoided and it changes the behaviour of the MMI. The design of 11 µm were designed following the rules mentioned and ideal behaviour has to be obtained.
These devices designed was introduced in MZIs and in SLR along the die to obtain the performance.

A.2 Test and characterization setup

An end-fire measurement setup is used with microscope objectives with MFD 2.5 µm and with polarization filters, in order to inject and collect TE polarization. All structures include edge couplers at the input and at the outputs, each at one side of the chip. To measure the response an ASE broadband source was employed, together with an OSA. All the measurements are normalized to the spectrum acquired without the chip, that is between the microscope objectives face to face. All measurements are with the polarizers set to allow TE to go through to/from the microscope objectives. Fiber collimators are employed, so as to allow fiber connections from the ASE source and to the OSA.

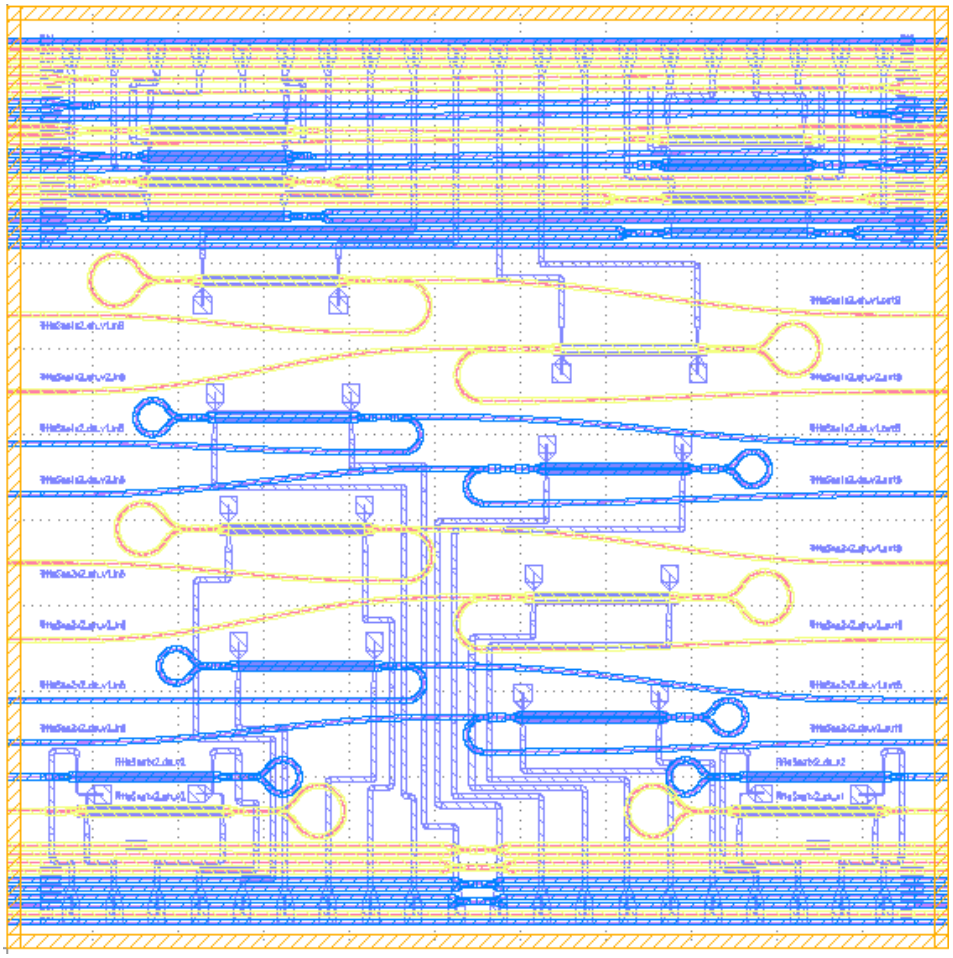

Figure A.1: Die design 5.5x5.5 mm^2.

Several copies of the design are provided, coming from different reticles patterned in the wafer. In the same wafer, the thicknesses are not the same along the wafer and this condition also changes the definition of the waveguides. Furthermore, the foundry provides more than one wafer so there are a lot of dies to test the variability of a specific device.

On the one hand, the optical elements response are normalized to the straight waveguides of the same chip. Thus, the facet response and the coupling losses is avoided. Moreover, the actives measurements of this chip were measured using electrical probes and electrical source to the electrical contacts inside the chip. Some of the chips were glued to a PCB board to use wire bonding, making easy the connection to the chip using standard connector. The measurements of the active elements follow the next steps:

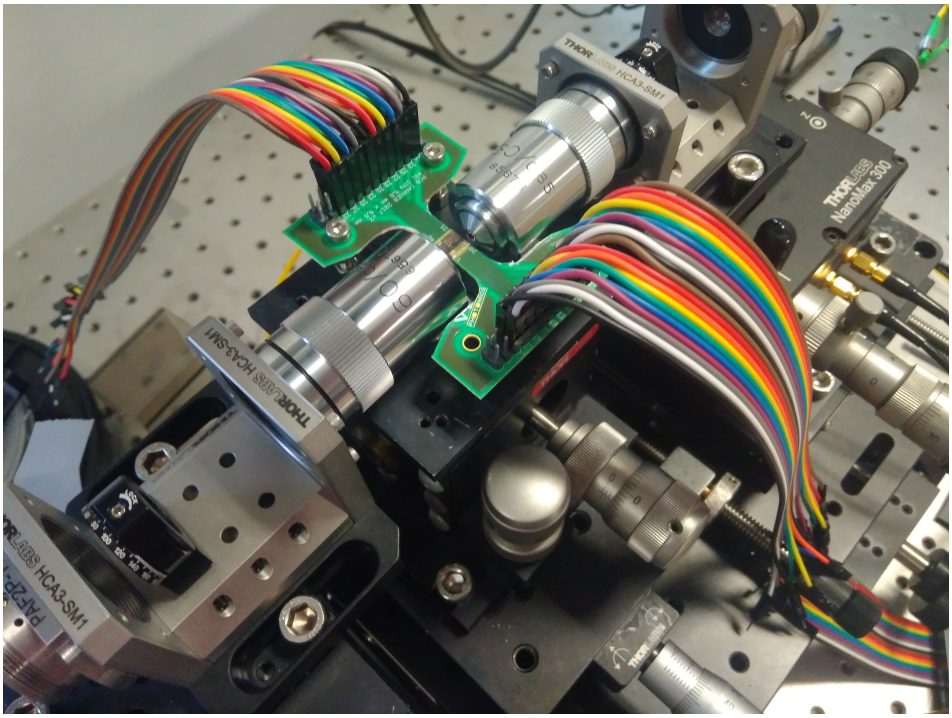

Figure A.2: Setup.

1. Contact the electrical probes to the pads inside the chip.
2. Align the optical ports to obtain the maximum spectra.
3. Vary the electrical source.

Appendix B
DPASTOR algorithm additional information

This supplementary section is to provide further detail on the optimization algorithm. The flow, illustrated in Fig. B.1 comprises three steps. The first two are performed once, and the third is repeated as will be described.

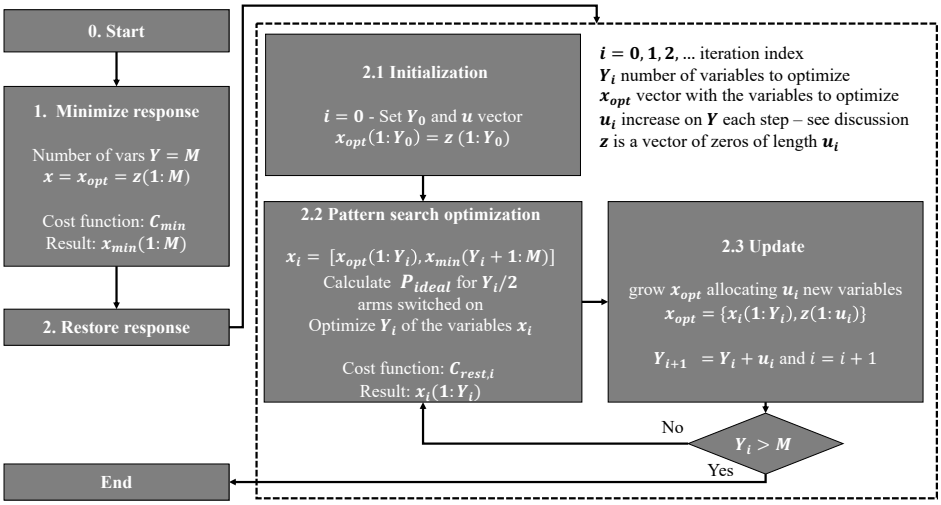

Figure B.1: Flow chart for the optimization algorithm.

Step 0. Start. Define the problem space as follows. For N arms in the R-RAWG, the total number of optimization variables is $M = 2N$. Each value corresponds to the current of one of the heaters. Recall each arm has tunable mirror, each with

two heaters. Owing to the internal structure of the problem, a R-RAWG, where the center arms have more power than the lateral arms, we order the optimization variables following that natural weight as follows, expressed as a vector:

$$x = \left\{I_{N/2,A}, I_{N/2,B}, I_{N/2-1,A}, I_{N/2-1,2B}, I_{N/2+1,A}, I_{N/2+1,2B}, ..., I_{1,A}, I_{1,B}, I_{N,A}, I_{N,B}\right\} \tag{B.1}$$

where $I_{n,A/B}$ is the current for arm number n and heater A or B within the tunable reflector of that particular arm. Note the order, starting from the center arms $n = N/2$ and then moving outwards.

Then, define the power spectral response of the R-RAWG (from one input to one output) as $P(M, W)$, with W the number of wavelength points $w = \{\lambda_0, \lambda_1, ..., \lambda_W\}$.

Step 1. Minimize response. Minimization using the pattern search algorithm and M variables. For this step, the cost function is defined as follows:

$$C_{min} = \sum_{r=0}^{W-1} 10 \log_{10} \left(P(M, r)\right) \tag{B.2}$$

with r an index to The algorithm has several stop criteria, but the most restrictive ones were found to be the change in the value of the cost function, and the change in the variables subject to optimization, among consecutive steps. This step, for $M = 38$ as in the presented device, took 2768 evaluations to converge in the case of the simulation presented in the paper. The experiments took 4600 iterations to converge (see tables below). Due to misalignment between the fiber array and the chip along time, that had to be manually corrected, it was performed in batches of 200-400 iterations. The pattern search algorithm allows for restarting from a previous point. Hence, after each batch the setup was re-aligned, and the pattern search algorithm resumed. The result of this step is a vector of size M, labelled as x_{min} in Fig. B.1.

Step 2. Restore response. Enable iteratively new R-RAWG arms, increasing the number optimization variables accordingly, and hence progressing to the full R-RAWG response. In this step, the cost function is defined as the absolute square difference between the power response and ideal responses:

$$C_{rest,i} = \sum_{r=0}^{W-1} \left|10 \log_{10} \left(P(Y_i, r)\right) - 10 \log_{10} \left(P_{ideal}(Y_i, r)\right)\right|^2 \tag{B.3}$$

where $i = 0, 1, 2...$ is the iteration index. For the following, refer to the dashed box within Fig. B.1. In the initialization ('2.1' in the figure), $i = 0$, the initial number of variables to optimize, Y_0 is set, alongside the u vector that contains the number of new optimization variables added after each step. The initial variables to optimize are grouped in a vector x_{opt} filled with zeros. Next, in step 2.2, the vector x_i is composed by replacing the first Y_i elements of x_min with x_{opt}. The ideal

Parameter	Simulation	Experiment
Y_0	10	10
u	$[9, 19]$	$[9, 19]$
Iterations per step	$[754, 771, 1243]$	$[400, 800, 3400]$
Total iterations	2768	4600

Table B.1: Details for the minimization step, for the simulation and experiments described in the paper.

power transfer function for Y_i switched on elements (i.e. perfect amplitude and phase for each path) is calculated. The power transfer function, for the assembled x_i, $P(x_i, w)$ is calculated, and only Y_i are optimized. This is written in the cost function equation $C_{rest,i}$, as $P(Y_i, r)$. Upon completing this step, 2.3 is devised to update the variables. The corresponding panel in the figure shows that a new x_{opt} is created by a) incorporating the first Y_i position of the x_i, the outcome of the optimization 2.2 step and b) adding u_i zeros. After 2.3, a check is done, and the algorithm stops if the number of variables to optimize is larger than the maximum M.

Summary tables for the minimization and Gaussian optimization.
The tables hereby summarize the input parameters and required iterations, for the minimization and optimization towards a Gaussian band-shape, both for the simulation and experiments presented in the paper. Note that the minimization step, Table B.1, is designed similar for the simulation than for the experiment. As already discussed in previous paragraphs, practical reasons required performing the minimization in batches of smaller iterations, actuating over the setup to correct misalignments, then resuming the algorithm.

With respect to the optimization algorithm, Table B.2, note the different target out of band rejection, 40 dB for the simulation, and 20 dB for the experiment. The latter more conservative target is a choice with respect to the previous experience on AWGs within this same technology platform and similar design strategies (without the design refinements outlined in the paper as possible improvements). While on simulation we started with two arms ($Y_0 = 4$) in the experiment we enabled the central three arms ($Y_0 = 6$). Note than in simulation, in each step fewer new variables are added, as compared to the experiment (vectors u in the table). The motivation to enable more in the experiments is to minimize the effects of changing conditions in the experimental setup, that obviously do not take place in simulation. Note the also the heavy load of iterations for the experimental optimization, for the last 5 arms (10 tuners). As the simulation also reveals, the optimization effort in number of iterations grows towards the outer arms, because they have smaller energy, so their contribution to the response is not as critical as for the center ones. Finally, the table reveals the total number of iterations in the experiment (with more variables in each step) is less than for the simulation. This has two reasons. Firstly, the starting condition in the simulation is worse than in

Parameter	Simulation	Experiment
Target out of band rejection	40 dB	20 dB
Y_0	4	6
u	$[2, 4, 4, 4, 8, 12]$	$[4, 6, 12, 10]$
Iterations per step	$[147, 230, 214, 786, 1573, 3349, 4984]$	$[200, 400, 200, 7600]$
Total iterations	11283	8400

Table B.2: Details for the optimization step, for the simulation and experiments described in the paper, and target response Gaussian band-pass shape.

the practical device. We induced heavy amplitude and phase distortions, further than in reality, so as to stress-test the algorithm. Secondly, the target out of band rejection in simulation is two orders of magnitude larger than in the one set as requirement for the experiment.

Appendix C
R-RAWG reconfiguration results

This supplementary section is to provide further detail on the results obtained from R-RAWG.

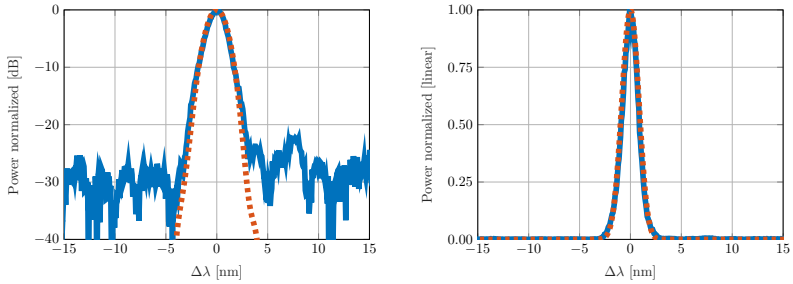

Figure C.1: Spectral normalized response of Gaussian shape. The horizontal axis is given as wavelength difference in nm from the peak center.

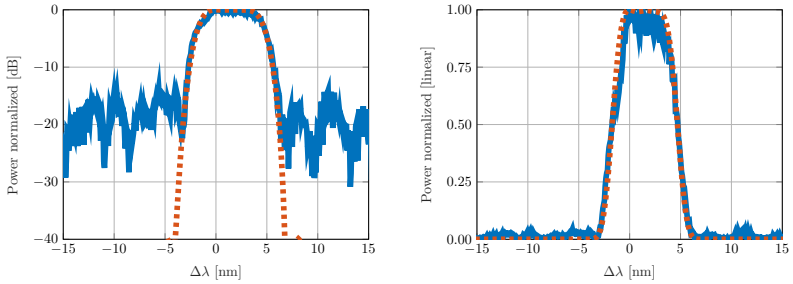

Figure C.2: Spectral normalized response of Flat shape. The horizontal axis is given as wavelength difference in nm from the peak center.

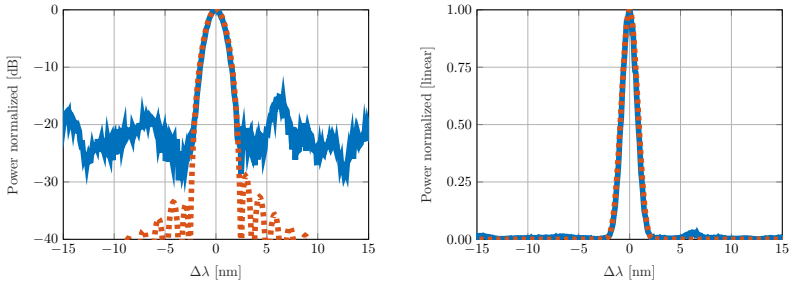

Figure C.3: Spectral normalized response of Bessel shape. The horizontal axis is given as wavelength difference in nm from the peak center.

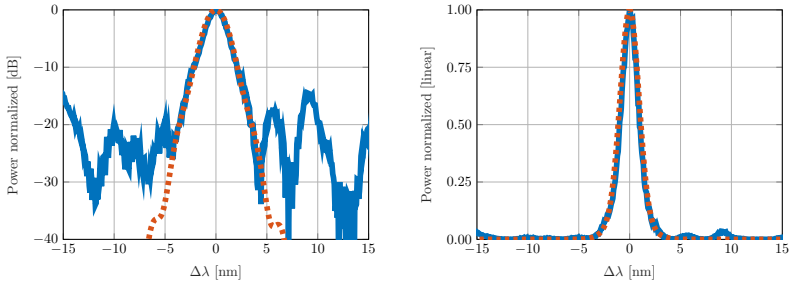

Figure C.4: Spectral normalized response of Exponential decrement shape. The horizontal axis is given as wavelength difference in nm from the peak center.

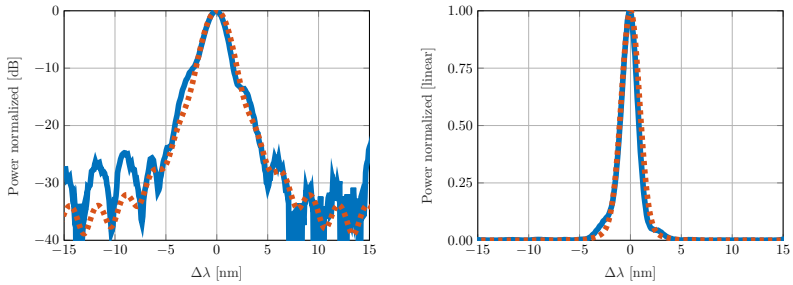

Figure C.5: Spectral normalized response of Lorentzian shape. The horizontal axis is given as wavelength difference in nm from the peak center.

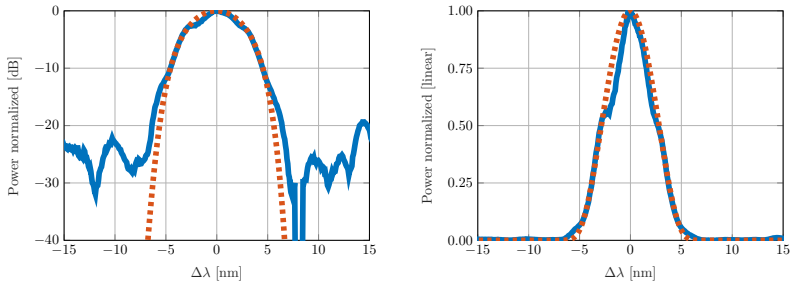

Figure C.6: Spectral normalized response of Truncate cosiner shape. The horizontal axis is given as wavelength difference in nm from the peak center.

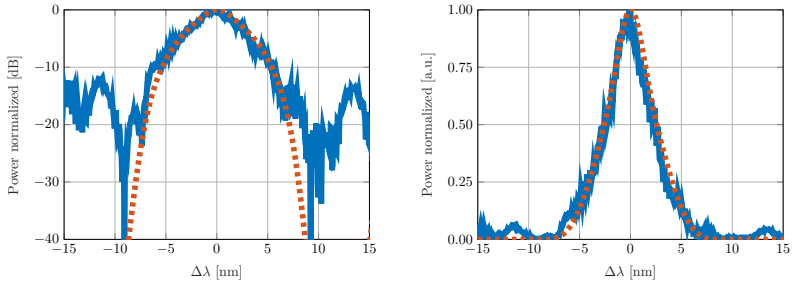

Figure C.7: Spectral normalized response of Triangular shape. The horizontal axis is given as wavelength difference in nm from the peak center.

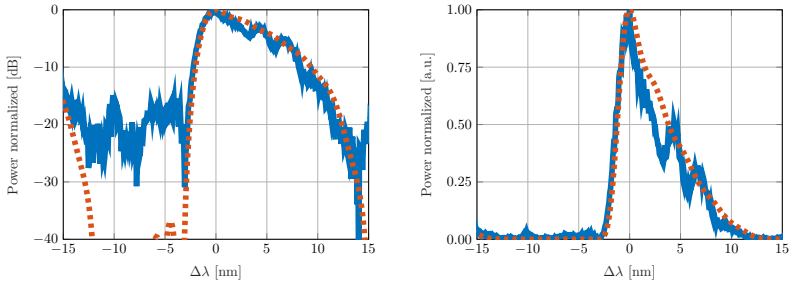

Figure C.8: Spectral normalized response of Left ramp shape. The horizontal axis is given as wavelength difference in nm from the peak center.

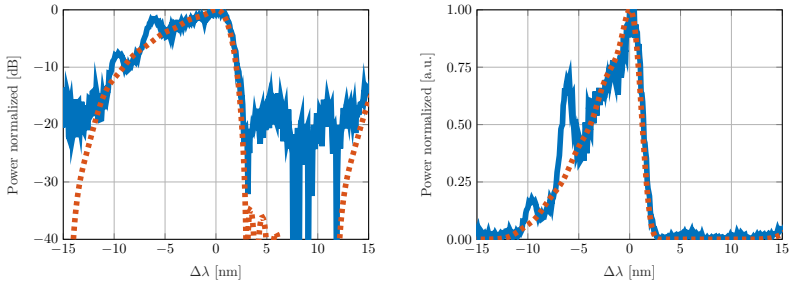

Figure C.9: Spectral normalized response of Right ramp shape. The horizontal axis is given as wavelength difference in nm from the peak center.

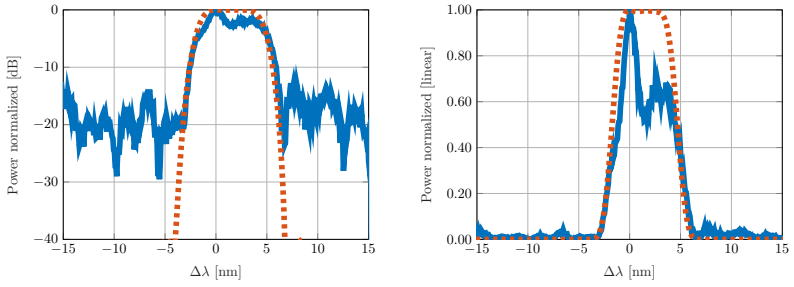

Figure C.10: Spectral normalized response of narrow flat shape. The horizontal axis is given as wavelength difference in nm from the peak center.

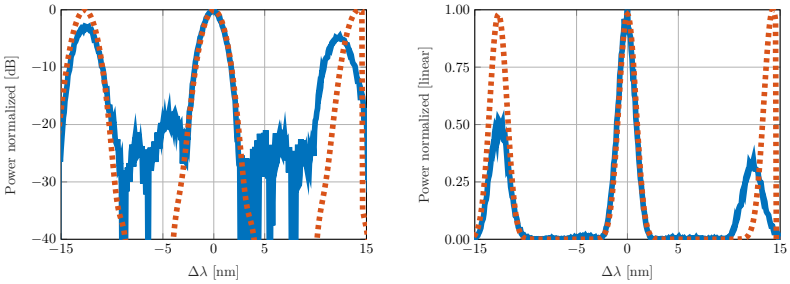

Figure C.11: Spectral normalized response duplicating the FSR. The horizontal axis is given as wavelength difference in nm from the peak center.

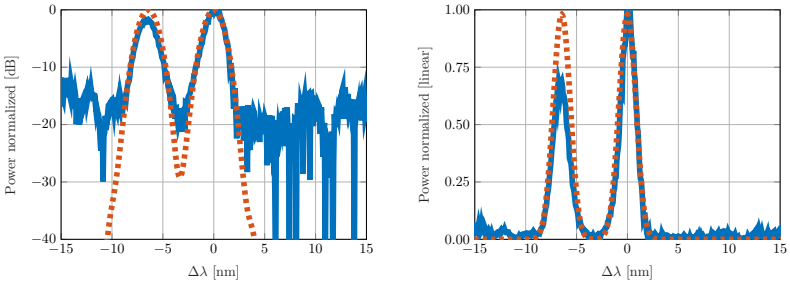

Figure C.12: Spectral normalized response of a notch filter. The horizontal axis is given as wavelength difference in nm from the peak center.

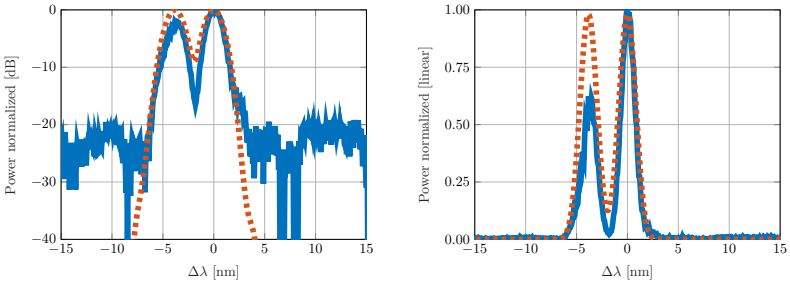

Figure C.13: Spectral normalized response of a narrow notch filter. The horizontal axis is given as wavelength difference in nm from the peak center.

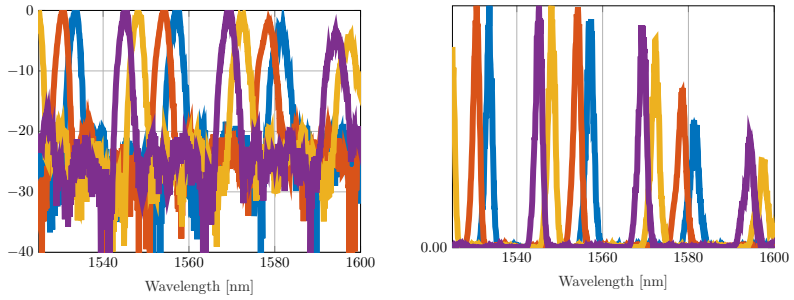

Figure C.14: Spectral normalized response of all the outputs for a gaussian shape configuration. The response is centred and optimized for C band.

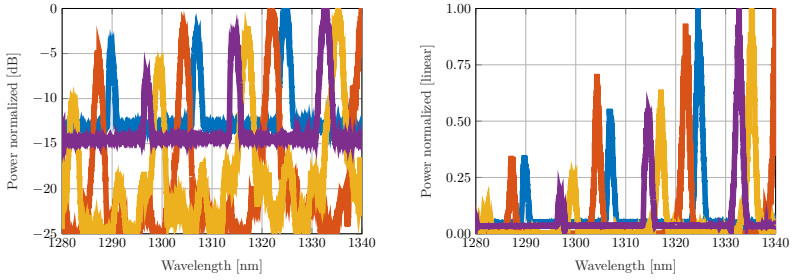

Figure C.15: Spectral normalized response of all the outputs for a gaussian shape configuration. The response is centred and optimized for O band.

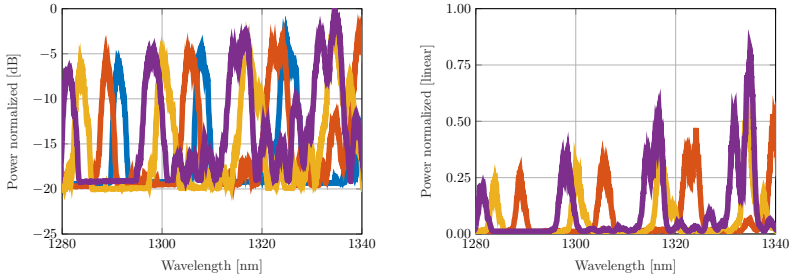

Figure C.16: Spectral normalized response of all the outputs for a flat shape configuration. The response is centred and optimized for O band.

Bibliography

[1] J. C. Maxwell, *A treatise on electricity and magnetism*. Oxford: Clarendon Press, 1873, vol. 1.

[2] H. Hertz, "Ueber einen Einfluss des ultravioletten Lichtes auf die electrische Entladung," *Annalen der Physik*, vol. 267, no. 8, pp. 983–1000, 1887.

[3] A. Einstein, "Über einem die Erzeugung und Verwandlung des Lichtes betreffenden heuristischen Gesichtspunkt," *Annalen der physik*, vol. 4, 1905.

[4] E. Schrödinger, "An undulatory theory of the mechanics of atoms and molecules," *Physical review*, vol. 28, no. 6, p. 1049, 1926.

[5] M. Zubairy, "A very brief history of light," in Dec. 2016, pp. 3–24, ISBN: 978-3-319-31902-5. DOI: 10.1007/978-3-319-31903-2_1.

[6] A. Einstein, "Zur Quantentheorie der Strahlung," *Physikalische Zeitschrift*, vol. 18, pp. 121–128, Jan. 1917.

[7] T. H. Maiman, "Stimulated optical radiation in ruby," *nature*, vol. 187, no. 4736, pp. 493–494, 1960.

[8] J. D. Montgomery, "History of fiber optics," in New York: Academic Press, 2002, pp. 3–31.

[9] B. Lojek, *History of semiconductor engineering*. Springer, 2007.

[10] R. G. Hunsperger, *Integrated optics*. Springer, 1995, vol. 4.

[11] C. R. Doerr and K. Okamoto, "Advances in silica planar lightwave circuits," *Journal of Lightwave Technology*, vol. 24, no. 12, pp. 4763–4789, 2006.

[12] ePIXnet Steering Committee *et al.*, Towards a foundry model in micro-and nano-photonics: a vision for Europe, `https://www.jeppix.eu/wp-content/jeppix/Vision+Document+Photonic+Foundry+Model+-+ePIXnet+Steering+Committee.pdf`, 2007.

[13] P. Munoz, J. D. Domenech, I. Artundo, J. H. den Bested, and J. Capmany, "Evolution of fabless generic photonic integration," in *2013 15th International Conference on Transparent Optical Networks (ICTON)*, IEEE, 2013, pp. 1–3.

[14] Trends in silicon photonics for fiber optic communication, `https://www.photonics.com/Articles/Trends_in_Silicon_Photonics_for_Fiber_Optic/a64191`.

[15] G. Treyz, "Silicon Mach-Zehnder waveguide interferometers operating at 1.3 mu m," *Electronics Letters*, vol. 27, no. 2, pp. 118–120, 1991.

[16] J Capmany, P Muñoz, J. Domenech, and M. Muriel, "Apodized coupled resonator waveguides," *Optics Express*, vol. 15, no. 16, pp. 10 196–10 206, 2007.

[17] S. Wang, "Principles of distributed feedback and distributed Bragg-reflector lasers," *IEEE Journal of Quantum Electronics*, vol. 10, no. 4, pp. 413–427, 1974.

[18] W. Bogaerts, S. K. Selvaraja, P. Dumon, J. Brouckaert, K. De Vos, D. Van Thourhout, and R. Baets, "Silicon-on-insulator spectral filters fabricated with CMOS technology," *IEEE Journal of Selected Topics in Quantum Electronics*, vol. 16, no. 1, pp. 33–44, 2010.

[19] H. Yen, H. Friedrich, R. Morrison, and G. Tangonan, "Planar Rowland spectrometer for fiber-optic wavelength demultiplexing," *Optics Letters*, vol. 6, no. 12, pp. 639–641, 1981.

[20] M. K. Smit and C. Van Dam, "PHASAR-based WDM-devices: Principles, design and applications," *IEEE Journal of Selected Topics in Quantum Electronics*, vol. 2, no. 2, pp. 236–250, 1996.

[21] D. P. López, A. L. Hernández, P. DasMahapatra, and J. Capmany, "Field-Programmable Photonic Array for multipurpose microwave photonic applications," in *2019 International Topical Meeting on Microwave Photonics (MWP)*, IEEE, 2019, pp. 1–4.

[22] Q. Zhang, H. Yu, M. Barbiero, B. Wang, and M. Gu, "Artificial neural networks enabled by nanophotonics," *Light: Science & Applications*, vol. 8, no. 1, pp. 1–14, 2019.

[23] X. Qiang, X. Zhou, J. Wang, C. M. Wilkes, T. Loke, S. O'Gara, L. Kling, G. D. Marshall, R. Santagati, T. C. Ralph, *et al.*, "Large-scale silicon quantum photonics implementing arbitrary two-qubit processing," *Nature photonics*, vol. 12, no. 9, pp. 534–539, 2018.

[24] D. T. Spencer, T. Drake, T. C. Briles, J. Stone, L. C. Sinclair, C. Fredrick, Q. Li, D. Westly, B. R. Ilic, A. Bluestone, *et al.*, "An optical-frequency synthesizer using integrated photonics," *Nature*, vol. 557, no. 7703, pp. 81–85, 2018.

[25] W. Liu, M. Li, R. S. Guzzon, E. J. Norberg, J. S. Parker, M. Lu, L. A. Coldren, and J. Yao, "A fully reconfigurable photonic integrated signal processor," *Nature Photonics*, vol. 10, no. 3, pp. 190–195, 2016.

[26] M. Li, Y. Deng, J. Tang, S. Sun, J. Yao, J. Azaña, and N. Zhu, "Reconfigurable optical signal processing based on a distributed feedback semiconductor optical amplifier," *Scientific reports*, vol. 6, p. 19 985, 2016.

[27] P. B. Deotare, I. Bulu, I. W. Frank, Q. Quan, Y. Zhang, R. Ilic, and M. Loncar, "All optical reconfiguration of optomechanical filters," *Nature Communications*, vol. 3, no. 1, pp. 1–8, 2012.

[28] Q. Xu and R. Soref, "Reconfigurable optical directed-logic circuits using microresonator-based optical switches," *Optics Express*, vol. 19, no. 6, pp. 5244–5259, 2011.

[29] M. S. Rasras, K.-Y. Tu, D. M. Gill, Y.-K. Chen, A. E. White, S. S. Patel, A. Pomerene, D. Carothers, J. Beattie, M. Beals, *et al.*, "Demonstration of a tunable microwave-photonic notch filter using low-loss silicon ring resonators," *Journal of Lightwave Technology*, vol. 27, no. 12, pp. 2105–2110, 2009.

[30] P. Muñoz, B. Gargallo, J. A. S. Fandiño, and J. Capmany, Photonic integrated device, US Patent 9,588,290, Mar. 2017.

[31] G. C. Righini and A. Chiappini, "Glass optical waveguides: a review of fabrication techniques," *Optical Engineering*, vol. 53, no. 7, p. 071 819, 2014.

[32] M. Smit, K. Williams, and J. Van Der Tol, "Past, present, and future of InP-based photonic integration," *APL Photonics*, vol. 4, no. 5, p. 050 901, 2019.

[33] R. Soref, "The past, present, and future of silicon photonics," *IEEE Journal of Selected Topics in Quantum Electronics*, vol. 12, no. 6, pp. 1678–1687, 2006.

[34] P. Muñoz, G. Micó, L. A. Bru, D. Pastor, D. Pérez, J. D. Doménech, J. Fernández, R. Baños, B. Gargallo, R. Alemany, *et al.*, "Silicon nitride photonic integration platforms for visible, near-infrared and mid-infrared applications," *Sensors*, vol. 17, no. 9, p. 2088, 2017.

[35] T. Aalto, M. Cherchi, M. Harjanne, S. Bhat, P. Heimala, F. Sun, M. Kapulainen, T. Hassinen, and T. Vehmas, "Open-Access 3-μm SOI Waveguide Platform for Dense Photonic Integrated Circuits," *IEEE Journal of Selected Topics in Quantum Electronics*, vol. 25, no. 5, pp. 1–9, 2019.

[36] C. G. Roeloffzen, M. Hoekman, E. J. Klein, L. S. Wevers, R. B. Timens, D. Marchenko, D. Geskus, R. Dekker, A. Alippi, R. Grootjans, *et al.*, "Low-loss Si3N4 TriPleX optical waveguides: Technology and applications overview," *IEEE Journal of Selected Topics in Quantum Electronicss*, vol. 24, no. 4, pp. 1–21, 2018.

[37] P. Munoz, P. W. van Dijk, D. Geuzebroek, M. Geiselmann, C. Dominguez, A. Stassen, J. D. Doménech, M. Zervas, A. Leinse, C. G. Roeloffzen, *et al.*, "Foundry developments toward silicon nitride photonics from visible to the mid-infrared," *IEEE Journal of Selected Topics in Quantum Electronics*, vol. 25, no. 5, pp. 1–13, 2019.

[38] A. Rahim, E. Ryckeboer, A. Z. Subramanian, S. Clemmen, B. Kuyken, A. Dhakal, A. Raza, A. Hermans, M. Muneeb, S. Dhoore, *et al.*, "Expanding the silicon photonics portfolio with silicon nitride photonic integrated circuits," *Journal of Lightwave Technology*, vol. 35, no. 4, pp. 639–649, 2017.

[39] VLC Photonics S.L. http://www.vlcphotonics.com/.

[40] Centro Nacional de Microelectronica (CNM), `http://www.imb-cnm.csic.es/index.php/en/clean-room/silicon-nitride-technology`.

[41] B. Gargallo and P. Munoz, "Advanced Arrayed Waveguide Gratings: Models, design strategies and experimental demonstration," Ph.D. dissertation, Universidad Politècnica de València, 2016.

[42] J. Fernández, R. Baños, D. Doménech, C. Domínguez, and P. Muñoz, "Low-loss inverted taper edge coupler in silicon nitride," *IET Optoelectronics*, vol. 13, no. 2, pp. 62–66, 2018.

[43] J. Fernandez, L. A. Bru, D. Pastor, D. Domenech, C. Domínguez, and P. Muñoz, "Sagnac Reflector Based Broadband Tunable Integrated Mirror," in *2020 22nd International Conference on Transparent Optical Networks (ICTON)*, IEEE, 2020, pp. 1–5.

[44] D. Nenni and P. M. McLellan, *Fabless: The transformation of the semiconductor industry*. SemiWiki. com Project, 2014.

[45] J. T. Macher and D. C. Mowery, "Vertical specialization and industry structure in high technology industries," *Advances in Strategic Management*, vol. 21, pp. 317–356, 2004.

[46] C. Brown, G. Linden, and J. T. Macher, "Offshoring in the semiconductor industry: A historical perspective [with comment and discussion]," in *Brookings Trade Forum*, JSTOR, 2005, pp. 279–333.

[47] W. Bogaerts and L. Chrostowski, "Silicon photonics circuit design: methods, tools and challenges," *Laser & Photonics Reviews*, vol. 12, no. 4, p. 1 700 237, 2018.

[48] A. Rahim, T. Spuesens, R. Baets, and W. Bogaerts, "Open-access silicon photonics: Current status and emerging initiatives," *Proceedings of the IEEE*, vol. 106, no. 12, pp. 2313–2330, 2018.

[49] S. Latkowski and D. Lenstra, "Lasers in InP generic photonic integration technology platforms," *Advanced Optical Technologies*, vol. 4, no. 2, pp. 179–188, 2015.

[50] K. Ławniczuk, L. M. Augustin, N. Grote, M. J. Wale, M. K. Smit, and K. A. Williams, "Open access to technology platforms for InP-based photonic integrated circuits," *Advanced Optical Technologies*, vol. 4, no. 2, pp. 157–165, 2015.

[51] K. Yao, R. Unni, and Y. Zheng, "Intelligent nanophotonics: merging photonics and artificial intelligence at the nanoscale," *Nanophotonics*, vol. 8, no. 3, pp. 339–366, 2019.

[52] C. Wang, M. Zhang, X. Chen, M. Bertrand, A. Shams-Ansari, S. Chandrasekhar, P. Winzer, and M. Lončar, "Integrated lithium niobate electro-optic modulators operating at CMOS-compatible voltages," *Nature*, vol. 562, no. 7725, pp. 101–104, 2018.

[53] M. G. Thompson, A. Politi, J. C. Matthews, and J. L. O'Brien, "Integrated waveguide circuits for optical quantum computing," *IET circuits, devices & systems*, vol. 5, no. 2, pp. 94–102, 2011.

[54] B. Luff, J. S. Wilkinson, J. Piehler, U. Hollenbach, J. Ingenhoff, and N. Fabricius, "Integrated optical mach-zehnder biosensor," *Journal of Lightwave Technology*, vol. 16, no. 4, p. 583, 1998.

[55] M. J. Heck, "Highly integrated optical phased arrays: photonic integrated circuits for optical beam shaping and beam steering," *Nanophotonics*, vol. 6, no. 1, pp. 93–107, 2017.

[56] J. Fernández Vicente, Reflectores de Sagnac reconfigurables en tecnología de Nitruro de Silicio, 2018.

[57] R. B. Balili, "Transfer matrix method in nanophotonics," in *International Journal of Modern Physics: Conference Series*, World Scientific, vol. 17, 2012, pp. 159–168.

[58] I. Anderson, "Transmission performance of Y-junctions in planar dielectric waveguide," *IEE Journal on Microwaves, Optics and Acoustics*, vol. 2, no. 1, p. 7, 1978.

[59] W Burns and A Milton, "An analytic solution for mode coupling in optical waveguide branches," *IEEE Journal of Quantum Electronics*, vol. 16, no. 4, pp. 446–454, 1980.

[60] R. H. Rediker and F. Leonbercer, "Analysis of integrated-optics near 3 dB coupler and Mach-Zehnder interferometric modulator using four-port scattering matrix," *IEEE Transactions on Microwave Theory and Techniques*, vol. 30, no. 10, pp. 1801–1804, 1982.

[61] M. Izutsu, Y. Nakai, and T. Sueta, "Operation mechanism of the single-mode optical-waveguide Y junction," *Optics Letters*, vol. 7, no. 3, pp. 136–138, 1982.

[62] M. Kuznetsov, "Radiation loss in dielectric waveguide Y-branch structures," *Journal of Lightwave Technology*, vol. 3, no. 3, pp. 674–677, 1985.

[63] A. Sakai, T. Fukazawa, and T. Baba, "Low loss ultra-small branches in a silicon photonic wire waveguide," *IEICE transactions on electronics*, vol. 85, no. 4, pp. 1033–1038, 2002.

[64] M Rangaraj, M Minakata, and S. Kawakami, "Low loss integrated optical Y-branch," *Journal of Lightwave Technology*, vol. 7, no. 5, pp. 753–758, 1989.

[65] M. Hu, J. Huang, R Scarmozzino, M Levy, and R. Osgood, "A low-loss and compact waveguide Y-branch using refractive-index tapering," *IEEE Photonics technology letters*, vol. 9, no. 2, pp. 203–205, 1997.

[66] I. Krutov, M. Y. Saygin, I. Dyakonov, and S. Kulik, "Optimized low-loss integrated photonics silicon-nitride Y-branch splitter," in *AIP Conference Proceedings*, AIP Publishing LLC, vol. 2241, 2020, p. 020 027.

[67] Y. Zhang, S. Yang, A. E.-J. Lim, G.-Q. Lo, C. Galland, T. Baehr-Jones, and M. Hochberg, "A compact and low loss Y-junction for submicron silicon waveguide," *Optics Express*, vol. 21, no. 1, pp. 1310–1316, 2013.

[68] Z. Lin and W. Shi, "Broadband, low-loss silicon photonic Y-junction with an arbitrary power splitting ratio," *Optics Express*, vol. 27, no. 10, pp. 14 338–14 343, 2019.

[69] D. Dai, "Advanced passive silicon photonic devices with asymmetric waveguide structures," *Proceedings of the IEEE*, vol. 106, no. 12, pp. 2117–2143, 2018.

[70] C. Doerr, M Cappuzzo, E Chen, A Wong-Foy, L Gomez, A Griffin, and L Buhl, "Bending of a planar lightwave circuit 2x2 coupler to desensitize it to wavelength, polarization, and fabrication changes," *IEEE Photonics Technology Letters*, vol. 17, no. 6, pp. 1211–1213, 2005.

[71] K. Solehmainen, M. Kapulainen, M. Harjanne, and T. Aalto, "Adiabatic and multimode interference couplers on silicon-on-insulator," *IEEE Photonics Technology Letters*, vol. 18, no. 21, pp. 2287–2289, 2006.

[72] Y. Shani, C. H. Henry, R. C. Kistler, R. F. Kazarinov, and K. J. Orlowsky, "Integrated optic adiabatic devices on silicon," *IEEE Journal of quantum Electronics*, vol. 27, no. 3, pp. 556–566, 1991.

[73] T. A. Ramadan and R. M. Osgood, "Adiabatic couplers: design rules and optimization," *Journal of Lightwave Technology*, vol. 16, no. 2, p. 277, 1998.

[74] C Dragone, "Efficient N*N star couplers using Fourier optics," *Journal of Lightwave Technology*, vol. 7, no. 3, pp. 479–489, 1989.

[75] P. Trinh, S Yegnanarayanan, and B Jalali, "5 x 9 integrated optical star coupler in silicon-on-insulator technology," *IEEE Photonics Technology Letters*, vol. 8, no. 6, pp. 794–796, 1996.

[76] J. Zou, Z. Le, J. Hu, and J.-J. He, "Performance improvement for silicon-based arrayed waveguide grating router," *Optics Express*, vol. 25, no. 9, pp. 9963–9973, 2017.

[77] C. Castellan, S. Tondini, M. Mancinelli, C. Kopp, and L. Pavesi, "Reflectance reduction in a whiskered SOI star coupler," *IEEE Photonics Technology Letters*, vol. 28, no. 17, pp. 1870–1873, 2016.

[78] L. B. Soldano and E. C. Pennings, "Optical multi-mode interference devices based on self-imaging: principles and applications," *Journal of Lightwave Technology*, vol. 13, no. 4, pp. 615–627, 1995.

[79] P. A. Besse, M. Bachmann, H. Melchior, L. B. Soldano, and M. K. Smit, "Optical bandwidth and fabrication tolerances of multimode interference couplers," *Journal of Lightwave Technology*, vol. 12, no. 6, pp. 1004–1009, 1994.

[80] M. Bachmann, P. A. Besse, and H. Melchior, "General self-imaging properties in NxN multimode interference couplers including phase relations," *Applied optics*, vol. 33, no. 18, pp. 3905–3911, 1994.

[81] Y. Li and R. Baets, "Improved multi-mode interferometers (MMIs) on silicon-on-insulator with the optimized return loss and isolation," in *16th Annual Symposium of the IEEE Photononics Benelux Chapter, Belgium*, 2011.

[82] R Hanfoug, L. Augustin, Y Barbarin, J. van der Tol, E. Bente, F Karouta, D Rogers, Y. Oei, X. Leijtens, and M. Smit, "A Multimode Interference coupler with low reflections," in *10th Annual Symposium of the IEEE/LEOS Benelux Chapter, December 1-2, 2005, Mons, Belgium*, IEEE/LEOS, 2005, pp. 97–100.

[83] E. Kleijn, D. Melati, A. Melloni, T. de Vries, M. K. Smit, and X. J. Leijtens, "Multimode interference couplers with reduced parasitic reflections," *IEEE Photonics Technology Letters*, vol. 26, no. 4, pp. 408–410, 2013.

[84] P. A. Besse, E. Gini, M. Bachmann, and H. Melchior, "New 2x2 and 1x3 multimode interference couplers with free selection of power splitting ratios," *Journal of Lightwave Technology*, vol. 14, no. 10, pp. 2286–2293, 1996.

[85] J. D. Doménech, J. S. Fandino, B. Gargallo, and P. Munoz, "Arbitrary coupling ratio multimode interference couplers in silicon-on-insulator," *Journal of Lightwave Technology*, vol. 32, no. 14, pp. 2536–2543, 2014.

[86] A. Y. Piggott, J. Petykiewicz, L. Su, and J. Vučković, "Fabrication-constrained nanophotonic inverse design," *Scientific reports*, vol. 7, no. 1, pp. 1–7, 2017.

[87] A. Y. Piggott, J. Lu, K. G. Lagoudakis, J. Petykiewicz, T. M. Babinec, and J. Vučković, "Inverse design and demonstration of a compact and broadband on-chip wavelength demultiplexer," *Nature Photonics*, vol. 9, no. 6, pp. 374–377, 2015.

[88] S. Molesky, Z. Lin, A. Y. Piggott, W. Jin, J. Vucković, and A. W. Rodriguez, "Inverse design in nanophotonics," *Nature Photonics*, vol. 12, no. 11, pp. 659–670, 2018.

[89] C. M. Lalau-Keraly, S. Bhargava, O. D. Miller, and E. Yablonovitch, "Adjoint shape optimization applied to electromagnetic design," *Optics Express*, vol. 21, no. 18, pp. 21 693–21 701, 2013.

[90] L. F. Frellsen, Y. Ding, O. Sigmund, and L. H. Frandsen, "Topology optimized mode multiplexing in silicon-on-insulator photonic wire waveguides," *Optics Express*, vol. 24, no. 15, pp. 16 866–16 873, 2016.

[91] J. Huang, R Scarmozzino, and R. Osgood, "A new design approach to large input/output number multimode interference couplers and its application to low-crosstalk WDM routers," *IEEE Photonics Technology Letters*, vol. 10, no. 9, pp. 1292–1294, 1998.

[92] A. Hosseini, D. Kwong, C.-Y. Lin, B. S. Lee, and R. T. Chen, "Output Formulation for Symmetrically Excited One-to-N Multimode Interference Coupler," *IEEE Journal of Selected Topics in Quantum Electronics*, vol. 16, no. 1, pp. 61–69, 2009.

[93] A. Hosseini, H. Subbaraman, D. Kwong, Y. Zhang, and R. T. Chen, "Optimum access waveguide width for 1xN multimode interference couplers on silicon nanomembrane," *Optics Letters*, vol. 35, no. 17, pp. 2864–2866, 2010.

[94] P. Munoz, D. Pastor, J. Capmany, and S. Sales, "Analytical and numerical analysis of phase and amplitude errors in the performance of arrayed waveguide gratings," *IEEE Journal of Selected Topics in Quantum Electronics*, vol. 8, no. 6, pp. 1130–1141, 2002.

[95] H. Yamada, K. Okamoto, A. Kaneko, and A. Sugita, "Dispersion resulting from phase and amplitude errors in arrayed-waveguide grating multiplexers–demultiplexers," *Optics Letters*, vol. 25, no. 8, pp. 569–571, 2000.

[96] K Maru, M Okawa, and H Uetsuka, "Influence of statistical amplitude and phase errors on spectral response of arrayed-waveguide grating," *Electronics Letters*, vol. 35, no. 22, pp. 1967–1969, 1999.

[97] R. Halir, I Molina-Fernández, A Ortega-Monux, J. Wanguemert-Perez, D.-X. Xu, P. Cheben, and S. Janz, "A design procedure for high-performance, rib-waveguide-based multimode interference couplers in silicon-on-insulator," *Journal of lightwave technology*, vol. 26, no. 16, pp. 2928–2936, 2008.

[98] L. Vivien and L. Pavesi, *Handbook of silicon photonics*. Taylor & Francis, 2016.

[99] R. Marchetti, C. Lacava, L. Carroll, K. Gradkowski, and P. Minzioni, "Coupling strategies for silicon photonics integrated chips," *Photonics Research*, vol. 7, no. 2, pp. 201–239, 2019.

[100] X. Mu, S. Wu, L. Cheng, and H. Fu, "Edge Couplers in Silicon Photonic Integrated Circuits: A Review," *Applied Sciences*, vol. 10, no. 4, p. 1538, 2020.

[101] C. Kopp, S. Bernabe, B. B. Bakir, J.-M. Fedeli, R. Orobtchouk, F. Schrank, H. Porte, L. Zimmermann, and T. Tekin, "Silicon photonic circuits: on-CMOS integration, fiber optical coupling, and packaging," *IEEE Journal of Selected Topics in Quantum Electronics*, vol. 17, no. 3, pp. 498–509, 2010.

[102] L. Cheng, S. Mao, Z. Li, Y. Han, and H. Fu, "Grating Couplers on Silicon Photonics: Design Principles, Emerging Trends and Practical Issues," *Micromachines*, vol. 11, no. 7, p. 666, 2020.

[103] D. Patterson, I. De Sousa, and L.-M. Achard, "The future of packaging with silicon photonics," *Chip Scale Review*, vol. 21, no. 1, 2017.

[104] T. Tamir and S.-T. Peng, "Analysis and design of grating couplers," *Applied physics*, vol. 14, no. 3, pp. 235–254, 1977.

[105] D. Taillaert, P. Bienstman, and R. Baets, "Compact efficient broadband grating coupler for silicon-on-insulator waveguides," *Optics Letters*, vol. 29, no. 23, pp. 2749–2751, 2004.

[106] Y. Ding, C. Peucheret, H. Ou, and K. Yvind, "Fully etched apodized grating coupler on the SOI platform with- 0.58 dB coupling efficiency," *Optics Letters*, vol. 39, no. 18, pp. 5348–5350, 2014.

[107] W. S. Zaoui, A. Kunze, W. Vogel, M. Berroth, J. Butschke, F. Letzkus, and J. Burghartz, "Bridging the gap between optical fibers and silicon photonic integrated circuits," *Optics Express*, vol. 22, no. 2, pp. 1277–1286, 2014.

[108] Y. Atsumi, T. Yoshida, and Y. Sakakibara, "Design of aspherical-lensed Si surface optical coupler for coupling with standard single-mode optical fibers," *Japanese Journal of Applied Physics*, vol. 59, no. 10, p. 100 905, 2020.

[109] T. Yoshida, S. Tajima, R. Takei, M. Mori, N. Miura, and Y. Sakakibara, "Vertical silicon waveguide coupler bent by ion implantation," *Optics Express*, vol. 23, no. 23, pp. 29 449–29 456, 2015.

[110] T Yoshida, T Nishi, S Tajima, R Takei, M Suzuki, E Omoda, M Nagao, N. Miura, M Mori, and Y Sakakibara, "Vertically-curved silicon waveguide fabricated by ion-induced bending method for vertical light coupling," in *2013 IEEE 10th International Conference on Group IV Photonics, GFP 2013*, 2013, pp. 89–90.

[111] S. Khan, S. M. Buckley, J. Chiles, R. P. Mirin, S. W. Nam, and J. M. Shainline, "Low-loss, high-bandwidth fiber-to-chip coupling using capped adiabatic tapered fibers," *APL Photonics*, vol. 5, no. 5, p. 056 101, 2020.

[112] T. Barwicz, Y. Taira, T. W. Lichoulas, N. Boyer, Y. Martin, H. Numata, J.-W. Nah, S. Takenobu, A. Janta-Polczynski, E. L. Kimbrell, *et al.*, "A novel approach to photonic packaging leveraging existing high-throughput microelectronic facilities," *IEEE Journal of Selected Topics in Quantum Electronics*, vol. 22, no. 6, pp. 455–466, 2016.

[113] T. Tiecke, K. Nayak, J. Thompson, T Peyronel, N. De Leon, V Vuletić, and M. Lukin, "Efficient fiber-optical interface for nanophotonic devices," *Optica*, vol. 2, no. 2, pp. 70–75, 2015.

[114] M. J. Burek, C. Meuwly, R. E. Evans, M. K. Bhaskar, A. Sipahigil, S. Meesala, B. Machielse, D. D. Sukachev, C. T. Nguyen, J. L. Pacheco, *et al.*, "Fiber-coupled diamond quantum nanophotonic interface," *Physical Review Applied*, vol. 8, no. 2, p. 024 026, 2017.

[115] G. Son, S. Han, J. Park, K. Kwon, and K. Yu, "High-efficiency broadband light coupling between optical fibers and photonic integrated circuits," *Nanophotonics*, vol. 7, no. 12, pp. 1845–1864, 2018.

[116] Waft of teem photonics, https://www.teemphotonics.com/integrated-optics/waft-interface-products/.

[117] Y. Zhang, X. Xiao, K. Zhang, S. Li, A. Samanta, Y. Zhang, K. Shang, R. Proietti, K. Okamoto, and S. B. Yoo, "Foundry-enabled scalable all-to-all optical interconnects using silicon nitride arrayed waveguide router interposers and silicon photonic transceivers," *IEEE Journal of Selected Topics in Quantum Electronics*, vol. 25, no. 5, pp. 1–9, 2019.

[118] Y. Arakawa, T. Nakamura, Y. Urino, and T. Fujita, "Silicon photonics for next generation system integration platform," *IEEE Communications Magazine*, vol. 51, no. 3, pp. 72–77, 2013.

[119] Ormocer, https://www.ormocere.de/en.html.

[120] N. Lindenmann, *Photonic Wire Bonding as a Novel Technology for Photonic Chip Interfaces*. KIT Scientific Publishing, 2018, vol. 21.

[121] N Lindenmann, G Balthasar, D Hillerkuss, R Schmogrow, M Jordan, J. Leuthold, W Freude, and C Koos, "Photonic wire bonding: a novel concept for chip-scale interconnects," *Optics Express*, vol. 20, no. 16, pp. 17 667–17 677, 2012.

[122] M. R. Billah, M. Blaicher, T. Hoose, P.-I. Dietrich, P. Marin-Palomo, N. Lindenmann, A. Nesic, A. Hofmann, U. Troppenz, M. Moehrle, *et al.*, "Hybrid integration of silicon photonics circuits and InP lasers by photonic wire bonding," *Optica*, vol. 5, no. 7, pp. 876–883, 2018.

[123] Vanguard automation, https://www.vanguard-automation.com/photonic-wire-bonding-2/.

[124] H. Kobayashi, T. Yamamoto, M. Ekawa, T. Watanabe, T. Ishikawa, T. Fujii, H. Soda, S. Ogita, and M. Kobayashi, "Narrow-beam divergence 1.3-/spl mu/m multiple-quantum-well laser diodes with monolithically integrated tapered thickness waveguide," *IEEE Journal of Selected Topics in Quantum Electronics*, vol. 3, no. 6, pp. 1384–1391, 1998.

[125] Photon design, https://www.photond.com/.

[126] Comparative fdtd, eme, bpm of photon design, `https://www.photond.com/files/docs/leos_newsletter_feb08_article.pdf`.

[127] D. F. Gallagher and T. P. Felici, "Eigenmode expansion methods for simulation of optical propagation in photonics: pros and cons," in *Integrated optics: devices, materials, and technologies VII*, International Society for Optics and Photonics, vol. 4987, 2003, pp. 69–82.

[128] P. J. Cegielski, S. Suckow, A. L. Giesecke, C. Porschatis, H. Lerch, M. Lütticke, B. Chmielak, and M. C. Lemme, "Silicon Nitride Waveguides and Spot Size Converters with¡ 1.76 dB Loss Over Broad Wavelength Range from 1010 nm to 1110 nm for OCT Applications," in *ECIO 2020 22nd Edition Proceedings*, European conference on integrated optics, 2020.

[129] J. Leuerman, A. Fernández-Gavela, L. Lechuga, A. Sánchez-Postigo, Í. Molina-Fernández, and R. Halir, "Towards photonic biosensing using a three-port mach-zehnder interferometer in a silicon nitride platform," in *ECIO 2018 20th Edition Proceedings*, European conference on integrated optics, 2018.

[130] J. A. Summers, V. Lal, M. L. Masanovic, N. Dagli, and D. J. Blumenthal, "Concave low-loss total internal reflection mirrors in indium phosphide for high fabrication tolerance," in *2007 Conference on Lasers and Electro-Optics (CLEO)*, IEEE, 2007, pp. 1–2.

[131] J. Klamkin, H. Zhao, B. Song, Y. Liu, B. Isaac, S. Pinna, F. Sang, and L. Coldren, "Indium phosphide photonic integrated circuits: Technology and applications," in *2018 IEEE BiCMOS and Compound Semiconductor Integrated Circuits and Technology Symposium (BCICTS)*, IEEE, 2018, pp. 8–13.

[132] Y. Fan, A. van Rees, P. J. Van der Slot, J. Mak, R. M. Oldenbeuving, M. Hoekman, D. Geskus, C. G. Roeloffzen, and K.-J. Boller, "Hybrid integrated InP-Si 3 N 4 diode laser with a 40-Hz intrinsic linewidth," *Optics Express*, vol. 28, no. 15, pp. 21 713–21 728, 2020.

[133] J. Mak, A. van Rees, Y. Fan, E. J. Klein, D. Geskus, P. J. van der Slot, and K.-J. Boller, "Linewidth narrowing via low-loss dielectric waveguide feedback circuits in hybrid integrated frequency comb lasers," *Optics Express*, vol. 27, no. 9, pp. 13 307–13 318, 2019.

[134] T. Birks and P Morkel, "Jones calculus analysis of single-mode fiber Sagnac reflector," *Applied optics*, vol. 27, no. 15, pp. 3107–3113, 1988.

[135] M. G. Kane, I. Glesk, J. P. Sokoloff, and P. R. Prucnal, "Asymmetric optical loop mirror: analysis of an all-optical switch," *Applied optics*, vol. 33, no. 29, pp. 6833–6842, 1994.

[136] B. Culshaw, "The optical fibre Sagnac interferometer: an overview of its principles and applications," *Measurement Science and Technology*, vol. 17, no. 1, R1, 2005.

[137] C.-S. Kim, B. Choi, J. S. Nelson, Q. Li, P. Z. Dashti, and H. Lee, "Compensation of polarization-dependent loss in transmission fiber gratings by use of a Sagnac loop interferometer," *Optics Letters*, vol. 30, no. 1, pp. 20–22, 2005.

[138] X. Sun, L. Zhou, J. Xie, Z. Zou, L. Lu, H. Zhu, X. Li, and J. Chen, "Tunable silicon Fabry–Perot comb filters formed by Sagnac loop mirrors," *Optics Letters*, vol. 38, no. 4, pp. 567–569, 2013.

[139] X. Jiang, J. Wu, Y. Yang, T. Pan, J. Mao, B. Liu, R. Liu, Y. Zhang, C. Qiu, C. Tremblay, *et al.*, "Wavelength and bandwidth-tunable silicon comb filter based on Sagnac loop mirrors with Mach-Zehnder interferometer couplers," *Optics Express*, vol. 24, no. 3, pp. 2183–2188, 2016.

[140] C. Vázquez, S. E. Vargas, and J. M. S. Pena, "Sagnac loop in ring resonators for tunable optical filters," *Journal of Lightwave Technology*, vol. 23, no. 8, p. 2555, 2005.

[141] P. R. Patterson, D. Hah, M. Fujino, W. Piyawattanametha, and M. C. Wu, "Scanning micromirrors: An overview," in *Optomechatronic Micro/Nano Components, Devices, and Systems*, International Society for Optics and Photonics, vol. 5604, 2004, pp. 195–207.

[142] A. Liu and X. Zhang, "A review of MEMS external-cavity tunable lasers," *Journal of Micromechanics and Microengineering*, vol. 17, no. 1, R1, 2006.

[143] Hamamatsu, https://www.hamamatsu.com/eu/en/product/type/S13989-01H/index.html.

[144] L. G. de Peralta, A. A. Bernussi, V Gorbounov, J. Berg, and H Temkin, "Control of center wavelength in reflective-arrayed waveguide-grating multiplexers," *IEEE journal of quantum electronics*, vol. 40, no. 12, pp. 1725–1731, 2004.

[145] T. Suhara and H. Nishihara, "Integrated optics components and devices using periodic structures," *IEEE Journal of Quantum Electronics*, vol. 22, no. 6, pp. 845–867, 1986.

[146] W. Streifer, D Scifres, and R. Burnham, "Coupled wave analysis of DFB and DBR lasers," *IEEE Journal of Quantum Electronics*, vol. 13, no. 4, pp. 134–141, 1977.

[147] Z. Zhang, D. Felipe, V. Katopodis, P. Groumas, C. Kouloumentas, H. Avramopoulos, J.-Y. Dupuy, A. Konczykowska, A. Dede, A. Beretta, *et al.*, "Hybrid photonic integration on a polymer platform," in *Photonics*, Multidisciplinary Digital Publishing Institute, vol. 2, 2015, pp. 1005–1026.

[148] S. Reniers, J. van Engelen, K. Williams, J. van der Tol, and Y. Jiao, "Waveguide photonic crystal reflectors on InP-membranes-on-silicon," in *Proc. 21st Eur. Conf. Integr. Opt.*, 2019, pp. 1–3.

[149] J. D. Joannopoulos, P. R. Villeneuve, and S. Fan, "Photonic crystals: putting a new twist on light," *Nature*, vol. 386, no. 6621, pp. 143–149, 1997.

[150] K. Okamoto and K. Ishida, "Fabrication of silicon reflection-type AWGs with distributed Bragg reflectors," in *2013 18th OptoElectronics and Communications Conference held jointly with 2013 International Conference on Photonics in Switching (OECC/PS)*, IEEE, 2013, pp. 1–2.

[151] J. Zou, T. Lang, Z. Le, and J.-J. He, "Ultracompact silicon-on-insulator-based reflective arrayed waveguide gratings for spectroscopic applications," *Applied optics*, vol. 55, no. 13, pp. 3531–3536, 2016.

[152] X. Zhang, J. Van Engelen, S. Reniers, Z. Cao, Y. Jiao, and A. Koonen, "Reflecting AWG by using photonic crystal reflector on Indium-phosphide membrane on silicon platform," *IEEE Photonics Technology Letters*, vol. 31, no. 13, pp. 1041–1044, 2019.

[153] H Okayama, Y Onawa, H Takahashi, D Shimura, H Yaegashi, and H Sasaki, "Reflective arrayed waveguide grating with parallel arms using one-dimensional photonic crystal reflector," *Electronics Letters*, vol. 55, no. 21, pp. 1143–1145, 2019.

[154] M. Cherchi, S. Ylinen, M. Harjanne, M. Kapulainen, and T. Aalto, "MMI resonators based on metal mirrors and MMI mirrors: an experimental comparison," *Optics Express*, vol. 23, no. 5, pp. 5982–5993, 2015.

[155] J. S. Fandiño, J. D. Doménech, and P. Muñoz, "Two-port multimode interference reflectors based on aluminium mirrors in a thick SOI platform," *Optics Express*, vol. 23, no. 16, pp. 20 219–20 233, 2015.

[156] E. Kleijn, M. K. Smit, and X. J. Leijtens, "Multimode interference reflectors: a new class of components for photonic integrated circuits," *Journal of Lightwave Technology*, vol. 31, no. 18, pp. 3055–3063, 2013.

[157] E Kleijn, T De Vries, H. Ambrosius, M. Smit, and X. Leijtens, "MMI reflectors with free selection of reflection to transmission ratio," in *Proceedings of the 15th Annual Symposium of the IEEE Photonics Benelux Chapter*, vol. 18, 2010, p. 19.

[158] J. Brouckaert, W. Bogaerts, P. Dumon, D. Van Thourhout, and R. Baets, "Planar concave grating demultiplexer fabricated on a nanophotonic silicon-on-insulator platform," *Journal of Lightwave Technology*, vol. 25, no. 5, pp. 1269–1275, 2007.

[159] J. Wu and D. Gao, "Silicon Reflective Arrayed Waveguide Grating with Multimode Interference Reflectors," in *2016 Asia Communications and Photonics Conference (ACP)*, IEEE, 2016, pp. 1–3.

[160] H. Okayama, M. Kawahara, and T. Kamijoh, "Reflective waveguide array demultiplexer in LiNbO/sub 3," *Journal of Lightwave Technology*, vol. 14, no. 6, pp. 985–990, 1996.

[161] S. P. Frisbie, "Design of a c-band spectrometer based on an arrayed waveguide grating," Ph.D. dissertation, Texas Tech University, 2004.

[162] Y Inoue, A Himeno, K Moriwaki, and M Kawachi, "Silica-based arrayed-waveguide grating circuit as optical splitter/router," *Electronics Letters*, vol. 31, no. 9, pp. 726–727, 1995.

[163] P Muñoz, R García-Olcina, J. Doménech, M Rius, J Capmany, L. Chen, and C Habib, "Multi-wavelength laser based on an Arrayed Waveguide Grating and Sagnac loop reflectors monolithically integrated on InP," in *Proceedings of the 15th European Conference on Integrated Optics*, 2010.

[164] M. Cherchi, S. Ylinen, M. Harjanne, M. Kapulainen, and T. Aalto, "Dramatic size reduction of waveguide bends on a micron-scale silicon photonic platform," *Optics Express*, vol. 21, no. 15, pp. 17 814–17 823, 2013.

[165] Y. Ikuma, J. Ito, and H. Tsuda, "Integrated loop mirrors for catoptric functional waveguide devices," *IEICE Electronics Express*, vol. 5, no. 5, pp. 176–180, 2008.

[166] B Gargallo, P Muñoz, R Baños, A. Giesecke, J Bolten, T Wahlbrink, and H Kleinjans, "Silicon-on-insulator reflective arrayed waveguide grating with sagnac loop reflectors," in *2014 The European Conference on Optical Communication (ECOC)*, IEEE, 2014, pp. 1–3.

[167] T. Inaba and H. Tsuda, "Compact Si reflection type arrayed-waveguide grating with loopback mirrors," in *2016 IEEE Photonics Conference (IPC)*, IEEE, 2016, pp. 769–770.

[168] Q. Fang, X. Chen, Y. Zhao, J. Hu, H. Chen, C. Qiu, and M. Yu, "Folded Silicon-Photonics Arrayed Waveguide Grating Integrated With Loop-Mirror Reflectors," *IEEE Photonics Journal*, vol. 10, no. 4, pp. 1–8, 2018.

[169] B. Gargallo, P. Muñoz, R. Baños, A. L. Giesecke, J. Bolten, T. Wahlbrink, and H. Kleinjans, "Reflective arrayed waveguide gratings based on Sagnac loop reflectors with custom spectral response," *Optics Express*, vol. 22, no. 12, pp. 14 348–14 362, 2014.

[170] J. Capmany and M. A. Muriel, "A new transfer matrix formalism for the analysis of fiber ring resonators: compound coupled structures for FDMA demultiplexing," *Journal of Lightwave Technology*, vol. 8, no. 12, pp. 1904–1919, 1990.

[171] X. J. Leijtens and M. K. Smit, "S-matrix-oriented CAD tool for photonic integrated circuits," in *Integrated Optic Devices II*, International Society for Optics and Photonics, vol. 3278, 1998, pp. 6–12.

[172] C. Bachiller, H. E. Gonzalez, V. E. B. Esbert, Á. B. Martínez, and J. V. Morro, "Efficient technique for the cascade connection of multiple two-port scattering matrices," *IEEE transactions on microwave theory and techniques*, vol. 55, no. 9, pp. 1880–1886, 2007.

[173] D. Pérez, J. Fernández, R. Baños, J. D. Doménech, A. M. Sánchez, J. M. Cirera, R. Mas, J. Sánchez, S. Durán, E. Pardo, *et al.*, "Thermal tuners on a Silicon Nitride platform," *arXiv preprint arXiv:1604.02958*, 2016.

[174] J. E. Toney, *Lithium Niobate Photonics*. Artech House, 2015.

[175] R. Soref and B. Bennett, "Electrooptical effects in silicon," *IEEE journal of quantum electronics*, vol. 23, no. 1, pp. 123–129, 1987.

[176] M. de Lima Jr, M Beck, R Hey, and P. Santos, "Compact Mach-Zehnder acousto-optic modulator," *Applied physics letters*, vol. 89, no. 12, p. 121 104, 2006.

[177] Matlab, https://es.mathworks.com/products/matlab.html.

[178] Photonics research labs (prl) – iteam, http://www.iteam.upv.es/group/photonics-research-labs-prl/?lang=es.

[179] J. P. Epping, D. Marchenko, A. Leinse, R. Mateman, M. Hoekman, L. Wevers, E. J. Klein, C. G. H. Roeloffzen, M. Dekkers, and R. G. Heideman, "Ultra-low-power stress-based phase actuator for microwave photonics," in *2017 European Conference on Lasers and Electro-Optics and European Quantum Electronics Conference*, Optical Society of America, 2017, pp. 0–3. [Online]. Available: `\url{http://www.osapublishing.org/abstract.cfm?URI=CLEO_Europe-2017-CK_7_6}`.

[180] P. Morin, G. Raymond, D. Benoit, P. Maury, and R. Beneyton, "A comparison of the mechanical stability of silicon nitride films deposited with various techniques," *Applied surface science*, vol. 260, pp. 69–72, 2012.

[181] A Stoffel, A Kovacs, W Kronast, and B Müller, "LPCVD against PECVD for micromechanical applications," *Journal of Micromechanics and Microengineering*, vol. 6, no. 1, p. 1, 1996.

[182] M. H. P. Pfeiffer, C. Herkommer, J. Liu, T. Morais, M. Zervas, M. Geiselmann, and T. J. Kippenberg, "Photonic Damascene process for low-loss, high-confinement silicon nitride waveguides," *IEEE Journal of Selected Topics in Quantum Electronics*, vol. 24, no. 4, pp. 1–11, 2018.

[183] J. M. Olson, "Analysis of LPCVD process conditions for the deposition of low stress silicon nitride. Part I: preliminary LPCVD experiments," *Materials Science in Semiconductor Processing*, vol. 5, no. 1, pp. 51–60, 2002.

[184] M Ghaderi, G De Graaf, and R. Wolffenbuttel, "Thermal annealing of thin PECVD silicon-oxide films for airgap-based optical filters," *Journal of Micromechanics and Microengineering*, vol. 26, no. 8, p. 084 009, 2016.

[185] W. Shi, H. Zhang, G. Zhang, and Z. Li, "Modifying residual stress and stress gradient in LPCVD Si3N4 film with ion implantation," *Sensors and Actuators A: Physical*, vol. 130, pp. 352–357, 2006.

[186] M. Bahadori, A. Gazman, N. Janosik, S. Rumley, Z. Zhu, R. Polster, Q. Cheng, and K. Bergman, "Thermal rectification of integrated microheaters for microring resonators in silicon photonics platform," *Journal of Lightwave Technology*, vol. 36, no. 3, pp. 773–788, 2017.

[187] L. A. Bru, D. Pastor, and P. Muñoz, "Integrated optical frequency domain reflectometry device for characterization of complex integrated devices," *Optics Express*, vol. 26, no. 23, pp. 30 000–30 008, 2018.

[188] L. A. Bru, D. Pastor, and P. Munoz, "On the characterization of integrated power splitters and waveguide losses using optical frequency domain interferometry," in *ECIO 2019 21st Edition Proceedings*, European conference on integrated optics, 2019.

[189] J. Fernández, J. Felip, B. Gargallo, J. D. Doménech, D. Pastor, C. Domínguez-Horna, and P. Muñoz, "Reconfigurable reflective arrayed waveguide grating using optimization algorithms," *Optics Express*, vol. 28, no. 21, pp. 31 446–31 456, 2020.

[190] C. J. Sun, K. M. Schmidt, and W. Lin, "Silica waveguide devices and their applications," in *Optoelectronic Integrated Circuits VII*, International Society for Optics and Photonics, vol. 5729, 2005, pp. 9–17.

[191] Y. Hibino, "Recent advances in high-density and large-scale AWG multi/demultiplexers with higher index-contrast silica-based PLCs," *IEEE Journal of Selected Topics in Quantum Electronics*, vol. 8, no. 6, pp. 1090–1101, 2002.

[192] H Yamada, K Takada, Y Inoue, Y Ohmori, and S Mitachi, "Statically-phase-compensated 10 GHz-spaced arrayed-waveguide grating," *Electronics Letters*, vol. 32, no. 17, pp. 1580–1582, 1996.

[193] M Gehl, D Trotter, A Starbuck, A Pomerene, A. Lentine, and C DeRose, "Active phase correction of high resolution silicon photonic arrayed waveguide gratings," *Optics Express*, vol. 25, no. 6, pp. 6320–6334, 2017.

[194] R. Gatdula and C. DeRose, Negative Feedback Tuning of Arrayed Waveguide Gratings. https://www.osti.gov/servlets/purl/1279656, 2015.

[195] S. Tondini, C. Castellan, M. Mancinelli, C. Kopp, and L. Pavesi, "Methods for low crosstalk and wavelength tunability in arrayed-waveguide grating for on-silicon optical network," *Journal of Lightwave Technology*, vol. 35, no. 23, pp. 5134–5141, 2017.

[196] D. J. Geisler, N. K. Fontaine, T. He, R. P. Scott, L. Paraschis, J. P. Heritage, and S. Yoo, "Modulation-format agile, reconfigurable Tb/s transmitter based on optical arbitrary waveform generation," *Optics Express*, vol. 17, no. 18, pp. 15 911–15 925, 2009.

[197] N. Fontaine, R. Scott, J Cao, A Karalar, W Jiang, K Okamoto, J. Heritage, B. Kolner, and S. Yoo, "32 phasex32 amplitude optical arbitrary waveform generation," *Optics Letters*, vol. 32, no. 7, pp. 865–867, 2007.

[198] N. Fontaine, J. Yang, W. Jiang, D. Geisler, K Okamoto, R. Huang, and S. Yoo, "Active arrayed-waveguide grating with amplitude and phase control for arbitrary filter generation and high-order dispersion compensation," in *2008 34th European Conference on Optical Communication*, IEEE, 2008, pp. 1–2.

[199] R. P. Scott, N. K. Fontaine, J. P. Heritage, and S. Yoo, "Dynamic optical arbitrary waveform generation and measurement," *Optics Express*, vol. 18, no. 18, pp. 18 655–18 670, 2010.

[200] L. G. De Peralta, A. Bernussi, S Frisbie, R Gale, and H Temkin, "Reflective arrayed waveguide grating multiplexer," *IEEE Photonics Technology Letters*, vol. 15, no. 10, pp. 1398–1400, 2003.

[201] A. Bernussi, L. G. de Peralta, V Gorbounov, J. Linn, S Frisbie, R Gale, and H Temkin, "Mirror quality and the performance of reflective arrayed-waveguide grating multiplexers," *Journal of Lightwave Technology*, vol. 22, no. 7, pp. 1828–1832, 2004.

[202] A Krishnan, M Knapczyk, L. G. de Peralta, A. Bernussi, and H Temkin, "Reconfigurable direct space-to-time pulse-shaper based on arrayed waveguide grating multiplexers and digital micromirrors," *IEEE Photonics Technology Letters*, vol. 17, no. 9, pp. 1959–1961, 2005.

[203] P. Cheben, I. Powell, S. Janz, and D.-X. Xu, "Wavelength-dispersive device based on a Fourier-transform Michelson-type arrayed waveguide grating," *Optics Letters*, vol. 30, no. 14, pp. 1824–1826, 2005.

[204] D. Dai, X. Fu, Y. Shi, and S. He, "Experimental demonstration of an ultracompact Si-nanowire-based reflective arrayed-waveguide grating (de) multiplexer with photonic crystal reflectors," *Optics Letters*, vol. 35, no. 15, pp. 2594–2596, 2010.

[205] S. Pathak, "Silicon nano-photonics based arrayed waveguide gratings," Ph.D. dissertation, Ghent University, 2014.

[206] D. A. Miller, "Self-configuring universal linear optical component," *Photonics Research*, vol. 1, no. 1, pp. 1–15, 2013.

[207] G Lenz, B. Eggleton, C. Giles, C. Madsen, and R. Slusher, "Dispersive properties of optical filters for WDM systems," *IEEE journal of quantum electronics*, vol. 34, no. 8, pp. 1390–1402, 1998.

[208] H. Venghaus, *Wavelength filters in fibre optics*. springer, 2006, vol. 123.

[209] J. Fang and D. Savransky, "Amplitude and phase retrieval with simultaneous diversity estimation using expectation maximization," *JOSA A*, vol. 35, no. 2, pp. 293–300, 2018.

[210] S. Tondini, C. Castellan, M. A. Medina, and L. Pavesi, "Automatic Initialization Methods for Photonic Components on a Silicon-Based Optical Switch," *Applied Sciences*, vol. 9, no. 9, p. 1843, 2019.

[211] D. Melati, Y. Grinberg, M. K. Dezfouli, S. Janz, P. Cheben, J. H. Schmid, A. Sánchez-Postigo, and D.-X. Xu, "Mapping the global design space of nanophotonic components using machine learning pattern recognition," *Nature communications*, vol. 10, no. 1, pp. 1–9, 2019.

[212] Machine learning mastery, https://machinelearningmastery.com/4-steps-to-get-started-in-machine-learning/.

[213] D. M. Kita, B. Miranda, D. Favela, D. Bono, J. Michon, H. Lin, T. Gu, and J. Hu, "High-performance and scalable on-chip digital Fourier transform spectroscopy," *Nature communications*, vol. 9, no. 1, pp. 1–7, 2018.

[214] P. Munoz, D. Pastor, and J. Capmany, "Modeling and design of arrayed waveguide gratings," *Journal of Lightwave Technology*, vol. 20, no. 4, p. 661, 2002.

[215] M. Abramson, "Pattern search algorithms for mixed variable general constrained optimization problems," Ph.D. dissertation, PhD thesis, 2003.

[216] P. Muñoz, D. Pastor, J. Capmany, D. Ortega, A. Pujol, and J. R. Bonar, "AWG model validation through measurement of fabricated devices," *Journal of Lightwave Technology*, vol. 22, no. 12, p. 2763, 2004.

[217] P. Pramanick and P. Bhartia, *Modern RF and microwave filter design*. Artech House, 2016.

[218] H. Zhang, T.-W. Weng, P.-Y. Chen, C.-J. Hsieh, and L. Daniel, "Efficient neural network robustness certification with general activation functions," in *Advances in neural information processing systems*, 2018, pp. 4939–4948.

[219] M. R. Zadeh, S. Amin, D. Khalili, and V. P. Singh, "Daily outflow prediction by multi layer perceptron with logistic sigmoid and tangent sigmoid activation functions," *Water resources management*, vol. 24, no. 11, pp. 2673–2688, 2010.

[220] A. Masood, M. Pantouvaki, G. Lepage, P. Verheyen, J. Van Campenhout, P. Absil, D. Van Thourhout, and W. Bogaerts, "Comparison of heater architectures for thermal control of silicon photonic circuits," in *10th International Conference on Group IV Photonics*, IEEE, 2013, pp. 83–84.

[221] 10 multicurrent luzwavelabs, https://luzwavelabs.com/ldc-e-multicurrent10/.

[222] Ultra-high na single-mode fibers, `https://www.nufern.com/pam/optical_fibers/spec/id/988/`.

[223] B. Gargallo and P. Munoz, "Full field model for interleave-chirped arrayed waveguide gratings," *Optics Express*, vol. 21, no. 6, pp. 6928–6942, 2013.

[224] J. Wang, Z. Sheng, L. Li, A. Pang, A. Wu, W. Li, X. Wang, S. Zou, M. Qi, and F. Gan, "Low-loss and low-crosstalk 8× 8 silicon nanowire AWG routers fabricated with CMOS technology," *Optics Express*, vol. 22, no. 8, pp. 9395–9403, 2014.

[225] J. Park, J. Joo, G. Kim, S.-W. Yoo, and S. Kim, "Low-crosstalk silicon nitride arrayed waveguide grating for the 800-nm band," *IEEE Photonics Technology Letters*, vol. 31, no. 14, pp. 1183–1186, 2019.

[226] U. Khan, M. Fiers, and W. Bogaerts, "Experimental phase-error extraction and modelling in silicon photonic arrayed waveguide gratings," in *Silicon Photonics XV*, International Society for Optics and Photonics, vol. 11285, 2020, p. 1 128 510.